Gas-Liquid Segmented Flow Microfluidic Reactors

by

Seyed Ali Kazemi Oskooei
B.Sc., Sharif University of Technology, 2006

A Thesis Submitted in Partial Fulfillment
of the Requirements for the Degree of

MASTER OF APPLIED SCIENCE

in the Department of Mechanical Engineering

SUPERVISORY COMMITTEE

Gas-Liquid Segmented Flow Microfluidic Reactors

by

Seyed Ali Kazemi Oskooei
B.Sc., Sharif University of Technology, 2006

Supervisory Committee

Dr. David Sinton, (Department of Mechanical Engineering)
Supervisor

Dr. Peter Oshkai, (Department of Mechanical Engineering)
Departmental Member

ABSTRACT

Supervisory Committee
Dr. David Sinton, (Department of Mechanical Engineering)
Supervisor
Dr. Peter Oshkai, (Department of Mechanical Engineering)
Departmental Member

This thesis is devoted to the study and application of gas-liquid segmented flow microfluidic reactors. In the most common configuration, these devices facilitate mixing and reaction of liquid-phase constituents by the introduction of non-participating gas bubbles in a microchannel flow. In this work, segmented flow microreactors are modelled, designed, fabricated, tested and applied.

Residence time distribution (RTD) within the reactors is employed as a measure to quantify reactor performance. In order to narrow the residence time distribution, a novel microreactor with hybrid surface properties is developed. The injector channel is made wetting to the liquid phase to assure stable segmentation while the reaction channel is rendered less wetting to eliminate the lubricating film surrounding the gas bubbles. It is demonstrated through RTD testing that the hybrid microreactor shows up to 63% gain in performance over the fully-wetting reactor.

A numerical model is developed to study the feasibility of shear-induced breakup of nanoparticles within gas-liquid segmented flow reactors. The critical shear rate required for breakup is calculated from literature and is compared to the maximum shear rate value found through modeling to give a prediction for the possibility of particle breakup. Previous experimental data support the existence of shear-induced particle breakup. Here, the transition region where the liquid film meets the liquid plug is found to exhibit relatively high shear stresses. With these results, the potential role of shear-induced processing of nanoparticle systems is discussed.

Lastly, fabricating devices with long microchannel lengths, as required in this work, necessitates the ability to densely pattern microfluidic channels on a substrate with minimal defects. The fabrication methods developed and employed here for densely patterned, high surface area microchips are presented in detail. These microchips were employed in this thesis work and also in other collaborative works.

TABLE OF CONTENTS

LIST OF FIGURES

ACKNOWLEDGEMENT

I would like to express my sincerest gratitude to my supervisor, Dr. David Sinton, for his excellent guidance, support patience, and providing me the opportunity to work with him. Also, I would like to acknowledge and thank the members of the UVic Microfluidics Lab, past and present, for or the support, feedback and assistance they have provided during this endeavour. Special thanks to Joe Wang for his assistance in the Chemistry Lab, and also to Paul Wood and Mohsen Akbari for their friendly assistance and support. I would also like to acknowledge Dr. Matt Moffitt for his input and guidance related to the nanoparticle application, Dr. Tom Fyles and Sensific Technologies Inc. for their support, and Dr. Ned Djilali for use of his computer cluster.

I would like to also acknowledge the Natural Sciences and Engineering Research Council of Canada (NSERC) as well as the BC Innovation Council, that has given me the financial support to pursue my graduate education.

Finally, it is to my family that I dedicate this work for their love, encouragement and support. Thank you.

1. Chapter 1: INTRODUCTION

1.1 Aims and Motivations of This Thesis

Microfluidics is defined as the study and application of fluid flow on the micro scale [Stone et al. (2004); Shui et al. (2007)]. Microscale refers to structures with characteristic dimensions ranging from 1μm to 1mm [Whitesides (2006)]. Structures with characteristic dimension of smaller than 1μm are called nanostructures and involve nanofluidics [De Leebeeck (2006); De Leebeeck et al. (2006)]. Fluidic systems with characteristic dimension of greater than 1 mm are usually considered as macro-scale. Microscale flows have long been part of the fluid mechanics aspects of colloid science [Russel et al. (1989)], clinical chemistry, soil science, plant biology, and biomedical science [Shui et al. (2007)]. In the past decade and a half, the new research area of engineering microfluidics emerged following the development of microtechnology and microfabrication techniques [Duffy et al. (1998); Jensen (2001); Reyes et al. (2002); Shui et al. (2007)], and the growing need for micro-devices in analytical chemistry, chemical synthesis, biology, and biotechnology [Beebe et al. (2002); Stone et al. (2004); West et al. (2008)].

Microscale fluid flow is characterized by very low Reynolds numbers (< 1). Thus, in micro-structured flows viscous forces dominate inertia. In such a flow regime diffusion is the dominant means of transport and the fluid flow is instantaneous due to the negligible effects of inertia forces [Purcell (1977); Squires et al. (2005)]. This instantaneous behaviour makes microfluidic systems more controllable than their macro scale counterparts [Squires et al. (2005)]. These physical characteristics of micro systems along with their capability to analyze very small volumes of reagents and samples in a cheap, simple and rapid manner has made them a versatile tool in many different application [Whitesides and Stroock (2001); Beebe et al. (2002); Kamholz et al. (2004); Stone et al. (2004); Eijkel and van den Berg (2005); Whitesides (2006)].

Motivated by the unique characteristics of microfluidic systems, some recent healthcare research has been directed towards the development of point-of-care medical diagnosis systems. In addition to promises of improved accuracy, increased speed and reduced cost of diagnosis in developed economies, there is potential for developing economies to gain quality diagnostics without the costs associated with centralized lab facilities [Curtis et al. (2007); Yager et al. (2006); Tüdos et al. (2001); Sia et al. (2003); Meldrum et al. (2002); Liu et al. (2005)].

Another growing application area for microfluidics is energy applications. There is growing demand for reliable and efficient power sources for portable applications such as cell phones, laptop computers, personal organizers, and also more specialized devices such as clinical diagnostic tools, and medical and military field devices. This demand has motivated much recent research on developing microfluidic power generation systems such as membraneless microfluidic fuel cells. These fuel cells employ a colaminar flow of fuel and oxidant within a microchannel for generating power [Choban et al. (2004); Kjeang (2007,2008); Wainright et al. (2003); Dyer (2002)].

The application of microfluidics to control and facilitate chemical reactions is a growing area. Microreactors benefit from the small size and integrated multiple functions which can provide advantages as compared to the macro scale counterparts. Microreactors can also be inexpensive, mass-produced, and scaled-up to achieve throughput rates comparable with macroscale systems. Microreactors have been shown to have a number of advantages for chemical production. The high heat and mass transfer rates possible in microfluidic systems allow microreactors to operate in more aggressive conditions with higher process yields compared to the macroscale counter parts [Jensen (2001); Hardt et al. (2003)]. Microreactors also have safety benefits as a result of their small size and small volume of reactant they process. Due to their unique safety characteristics microreactors can be employed as point-of-use production units for materials with storage and shipment restrictions such as highly reactive and toxic reaction intermediates [Jensen (2001)].

Enhancing heat and mass transfer within microreactors has been one of the most central driving forces for research in this area. Structuring the reactor surface to increase the surface area has been shown to promote an order of magnitude enhancement in heat transport within reactors [Lebens et al. (1999); Hardt et al. (2003)]. Developing specific flow patterns within microreactors has also been shown to be a powerful tool in enhancing transport, especially mass transfer and mixing within reactors [Stroock et al. (2002)]. On that basis, multiphase flow patterns have been developed where a continuous flow of reactants is segmented by an immiscible disperse phase [Horvath et al. (1973); Song et al. (2003); Günther et al. (2004); Song et al. (2006); Ahmed et al. (2006)]. The most desirable outcomes of such segmentation are the generation of advective patterns within both phases and also the reduced mass transfer in the axial direction [Thiers et al. (1971); Kreutzer et al. (2005); Günther et al. (2006); Shui et al.

(2007)]. The degree of axial dispersion is an indicator of the reactor performance in allowing uniform reaction time for all fluid elements and delivering uniform reaction products as a consequence. In some applications the dispersed segmenting phase may also be involved in the reaction [Kreutzer et al. (2005); Günther et al. (2006)]. However, in passive segmentation, one phase is only present to enhance mixing properties in the reacting phase (i.e. the continuous phase) and to inhibit axial dispersion by partitioning the reactants [Song et al. (2003); Günther et al. (2004); Günther et al. (2006); Song et al. (2006)].

Both gas-liquid and liquid-liquid segmented flows have been developed and applied to a number of different applications in chemistry, biology, chemical synthesis and catalytic chemical reactions where enhanced mixing and low axial dispersion was required [Günther al. (2006); Kreutzer et al. (2005)]. Gas liquid segmented flow reactors however have been shown to be capable to operate stably in a wider range of flow velocities and temperatures compared to the liquid-liquid counterparts [Günther et al. (2004); Yen et al. (2005)]. Gas-liquid reactors have been widely applied to particle synthesis and catalytic monolith reactors [Günther et al. (2004); Khan et al. (2004); Trachsel et al. (2005); Yen et al. (2005); Kreutzer et al (2005);].

The reduced axial dispersion in gas-liquid segmented flow reactors has been quantified using the residence time distribution (RTD) concept. RTD is a distribution of the time fluid elements spend within the reactor. It has been observed that the segmented flow reactor possesses a significantly narrower residence time distribution (RTD) compared to the single phase counter parts [Thulasidas et al. (1999); Günther et al. (2004); Khan et al. (2004); Trachsel et al. (2005)]. Although Gas-liquid segmented flow reactors provide significant decrease in axial dispersion and slug-to-slug contamination, there is still a considerable communication among the liquid slugs through the lubricating film which surrounds the bubbles [Pedersen et al. (1981); Thulasidas et al. (1999); Kreutzer et al. (2008)]. This liquid film is an intrinsic feature of the segmented flow pattern in microreactors with wetting surfaces [Taylor (1961)].

The central motivation in this thesis is to enhance the performance of a gas-liquid segmented flow microreactor by modifying the reactor surface in a way that the lubricating thin film is eliminated while maintaining the stable segmented flow pattern. The surface modification of the reactor is expected to reduce the only means of axial dispersion present in regular gas-liquid segmented flow reactors while allowing the reactor to benefit from the chaotic mixing present in the segmented flow pattern.

A secondary motivation of this thesis is the study of hydrodynamics of gas-liquid segmented flow. To the author's knowledge, shear forces in gas-liquid segmented microfluidic reactors have not been studied or intentionally exploited prior to this work. The aim here is to study shear forces and strain rates in these reactors and compare these with classical droplet break-up theory in order to determine if shear forces could be playing a significant role in these systems. The nanoparticle system of interest here is that of the collaborating Moffitt Group (UVic Chemistry), quantum dot compound micelles. These particles are promising as bio-labels, and for such applications it is desirable to have a high degree of control over particle size and constituents [Yusuf et al. (2007a), Yusuf et al. (2007b)]. This work follows from earlier demonstrations of microfluidic reactor based assembly of these particles [Schabas (2007); Schabas al. (2008a), Schabas al. (2008b)]. Researching the role of shear in on-chip processing and size control of these particles has motivated the third chapter of this thesis.

The complex microreactors employed in this thesis required a robust fabrication method which allowed development of a wide range of microchannel sizes and geometries. The need for such fabrication capabilities and methods motivated the fourth chapter of the current thesis work.

1.2 Microfluidic Transport Phenomena

Microfluidics is the study and application of fluid flow in microstructures with characteristic dimensions between 1 and 100 μm. Flow in micro-structures is significantly different than in macroscale counter parts. At the microscale, surface forces become the dominant forces while body forces and inertia forces become negligible. The dominance of surface forces over body forces can be explained by the high surface to volume ratio in microstructured fluid flow.

Viscous and surface tension forces are both inversely proportional to the channel diameter, d, (or hydraulic diameter, d_H, for non-circular channels), and for small diameters these forces will dominate inertia and gravity forces. The microscale flow regime can be characterized using dimensionless groups such as Re which relates inertia forces to viscous forces [Reynolds (1883)]. The Re number is defined as

$$Re = \frac{\rho U d_H}{\mu} \tag{1.1}$$

Where ρ represents the mass density of the fluid, U is the characteristic velocity of the flow, d_H is characteristic dimension of the flow channel, and μ is dynamic viscosity coefficient of the fluid. The Reynolds number is used to classify fluid flow in macro scale structures as laminar or turbulent [Reynolds (1883)]. Due to their small characteristic dimension and velocity microscale flows have Reynolds numbers on the order of unity or lower and are hence characterized as laminar. In laminar flow, fluid elements move along parallel ordered streamlines and all perturbations in the flow diminish by dominating viscous forces [White (2003)].

Due to the negligible inertia forces (as compared to viscous forces), microfluidic flows are effectively instantaneous. That is, the flow cannot effectively store inertia, instead fluid elements react to instantaneous forces and are relatively uninfluenced by flow history [Purcell (1977)]. In other words, fluid velocities at time *t*, are a result of forces acting at time *t*. This aspect of microscale flows is a direct consequence of diffusion dominated momentum transport (low Re).

Several publications and texts in the field of microfluidics describe the physics of transport phenomena in microscale including topics such as fluid flow [Sharp et al. (2002); Kirby and Hasslebrink (2004); Stone et al. (2004)], diffusion [Hatch et al.(2004); Squires and Quake (2005)] and multiphase kinetics [Bringer et al. (2004); deMello (2006)]. The following section provides an overview of the fundamental phenomena relevant in the context of this thesis.

1.2.1 Equations of Transport and Microscale Fluid Flow

A fluid flow is completely determined if the velocity vector **V** and the thermodynamic properties, the pressure P, the density ρ, and the temperature T are known everywhere in the flow field. These six quantities, the three velocity components in three spatial directions and the thermodynamic variables have to be provided for the description of the flow. This can be done by solving the conservation equations for mass, momentum, and energy and the thermal equation of state, which connects the thermodynamic variables [Acheson (1990); Probstein (1994); White (2003); Krause (2005)]. If the material properties such as the dynamic viscosity, density, thermal conductivity, and specific heat change significantly, then they must be prescribed as a function of pressure and temperature. Liquids are normally considered as incompressible and their density ρ is thus assumed to be constant. This assumption also holds for gases flowing at low speeds. Here we focus on conservation laws for incompressible flows and study their application to microscale flows.

In a moving fluid the three fundamental laws, conservation of mass, momentum, and energy, must be satisfied at every point in the domain. Thus the first step is to formulate the three laws in a form that satisfies this condition. This is accomplished by applying each law to a differential (infinitesimal) element as shown in a schematic in Figure (1.1). Following this approach, each law is described by a partial differential equation. Differential formulation of the three laws will be presented using rectangular coordinates [Acheson (1990); Probstein (1994); White (2003); Krause (2005)].

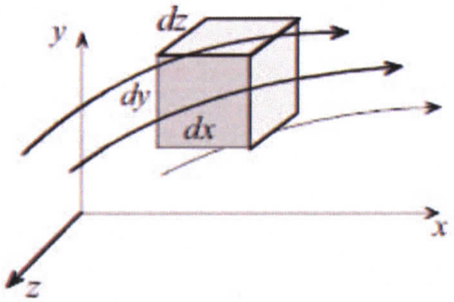

Figure 1.1 Differential (infinitesimal) fluid element

The conservation of mass within a fluid element suggests that the rate of mass change within the element must be equal to the rate of mass added to the element minus rate of mass removed from element, This balance of mass results in the well-known continuity equation given in Eq. (1.2),

$$\frac{\partial \rho}{\partial t}+\frac{\partial}{\partial x}(\rho u)+\frac{\partial}{\partial y}(\rho v)+\frac{\partial}{\partial z}(\rho w)=0 \tag{1.2}$$

where ρ is the fluid density and u, v, and w are velocity components in x, y, and z directions, respectively. For incompressible flow, ρ is constant and Eq. (1.2) is reduced to

$$\frac{\partial u}{\partial x}+\frac{\partial v}{\partial y}+\frac{\partial w}{\partial z}=0 \tag{1.3}$$

Momentum is a vector quantity. Thus conservation of momentum (Newton's law of motion) provides three equations, one in each of the three coordinates. Application of Newton's law of motion to the fluid element shown in Figure 1.1 gives

$$\underbrace{\rho\left(\frac{\partial \vec{V}}{\partial t}+(\vec{V}\cdot\vec{\nabla})\vec{V}\right)}_{\text{acceleration term}}=\underbrace{\rho\vec{g}}_{\text{body forces}}-\overbrace{\vec{\nabla}p+\mu\vec{\nabla}^{2}\vec{V}}^{\text{surface forces}} \tag{1.4}$$

where $\vec{g}$ denotes the gravitational acceleration, p is the pressure, $\vec{V}$ is the velocity vector, and a Newtonian fluid is assumed. The left hand side of Eq. (1.4) represents the flow acceleration and the right hand side terms each represent a force (per unit volume) acting on the fluid element. The $\rho\vec{g}$ term is the gravity force, the $\vec{\nabla}p$ term is the pressure gradient, the $\mu\nabla^2\vec{V}$ term represents the viscous forces acting on the surface of the element and the term on the left-hand side collectively represents the acceleration of the fluid [Acheson (1990); Probstein (1994); White (2003); Krause (2005)].

A dimensionless form of Navier-Stokes equations can be obtained from substitution of following terms in Eq. (1.4)

$$\vec{V}=\overrightarrow{V^{*}}U\ ,\ \vec{\nabla}=\overrightarrow{\nabla^{*}}\left(\frac{1}{D}\right),\ t=t^{*}\left(\frac{D}{U}\right),\ p=p^{*}\left(\frac{\mu U}{D}\right),\ \vec{g}=\overrightarrow{g^{*}}\left(\frac{U^{2}}{D}\right) \tag{1.5}$$

The starred quantities are then dimensionless quantities whose size varies from zero to order one. The dimensionless Navier-Stokes equation is shown in Eq. (1.6),

$$Re\left(\frac{\partial\overrightarrow{V^{*}}}{\partial t^{*}}+(\overrightarrow{V^{*}}\cdot\overrightarrow{\nabla^{*}})\overrightarrow{V^{*}}-\rho\overrightarrow{g^{*}}\right)=-\overrightarrow{\nabla^{*}}p^{*}+\overrightarrow{\nabla^{*}}^{2}\overrightarrow{V^{*}} \tag{1.6}$$

in which all the variables appear in dimensionless form and Re number appears as a key parameter. If Re number is very small, which is the case for many microscale flows, the entire left hand side of Eq. (1.6) which includes inertia and gravity terms becomes negligible [Probstein (1994); Nguyen and Wereley, (2002)]. Hence, in microscale flow regime Navier-stokes equation is simplified to a linear partial differential equation also known as Stokes equation

$$-\vec{\nabla}p+\mu\vec{\nabla}^{2}\vec{V}=0 \tag{1.7}$$

Many microscale devices have straight channels of constant cross section. For laminar flow in such parallel microchannels the flow field is one dimensional (for instance in x direction). Under this condition Stokes flow can be written as

$$\frac{\partial p}{\partial x}=\mu\left(\frac{\partial^{2}u}{\partial y^{2}}+\frac{\partial^{2}u}{\partial z^{2}}\right) \tag{1.8}$$

Analytical solutions to Eq. (1.8) are available [Nguyen and Wereley, (2002)] for channels of rectangular cross section which are the most common in microfluidic devices including those developed and studied in this thesis. The velocity profile in a microchannel with rectangular cross section is

$$u(y,z)=\frac{16a^3}{\mu\pi^3}\left(-\frac{dp}{dx}\right)\sum_{i=1,2,\ldots}^{\infty}(-1)^{(i-1)/2}\left[1-\frac{\cosh(i\pi z/2a)}{\cosh(i\pi b/2a)}\right]\frac{\cos(i\pi y/2a)}{i^3} \tag{1.9}$$

Where a and b are the cross sectional dimensions. It is notable that for microchannel geometries with high aspect ratio (width/height) the flow field can be approximated with that of flow between two infinite parallel plates. In that case velocity profile only varies in one direction (y direction here) and can be approximated as

$$u(y)=\frac{1}{2\mu}\frac{dp}{dx}\left(y^2-(b/2)^2\right) \tag{1.10}$$

where, b is the channel height or the distance between infinite parallel plates. This type of flow is also known as Poiseuille flow [Acheson (1990); Probstein (1994); White (2003); Krause (2005)].

The schematics in Figure 1.2 demonstrate roughly the velocity profiles across the channel width and height within rectangular microchannels with finite aspect ratio similar to those employed in this thesis work. The aspect ratio for microchannels studied in this thesis is fairly small (width/height ~ 2.67). Hence, the latter simplified solution does not apply here and velocity is a function of both y and z as given in Eq. (1.9). However, velocity gradients along the larger dimension (width) are, in general, smaller than those along the channel height.

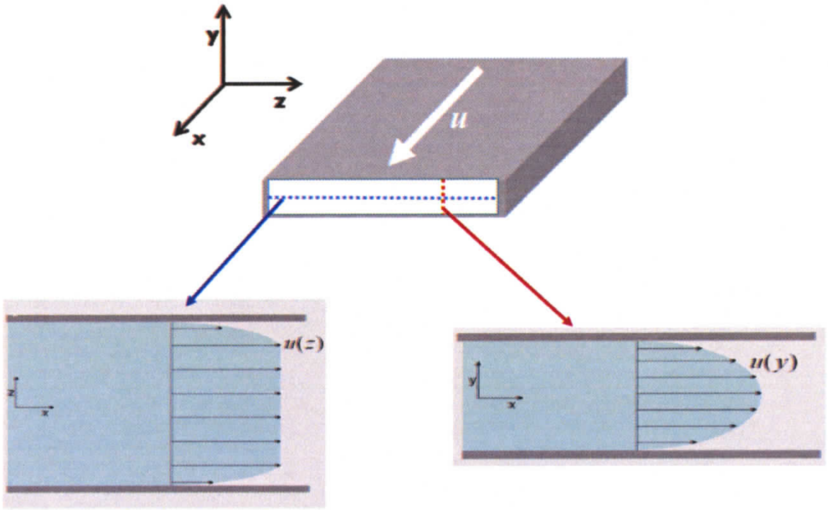

a) b)

Figure 1.2 a) velocity profile across the channel width b) velocity profile across the channel height.

The above analysis covers hydrodynamics of homogeneous flow. In many microfluidic applications, the fluid contains dissolved substances (contaminants or reactants) and is a solution or a mixture. The composition of solutions is usually characterized by the mass density of each constituent substance (the mass of dissolved substance per unit volume) or the dimensionless mass concentration C (the ratio of the mass density of a substance to the total density of the mixture) [Bird et al. (1960); Probstein (1994); Polyanin et al. (2002)]. The concentration of individual components at each point of the flow field depends on convective mass transfer, molecular diffusion, and the intensity of physical and chemical transformations [Bird et al. (1960); Probstein (1994); Polyanin et al. (2002)].

Assuming that the fluid density and viscosity are independent of concentration, the concentration distribution does not influence the flow field. This assumption allows hydrodynamic problem to be decoupled from the mass transfer problem [Bird et al.

(1960); Probstein (1994); Polyanin et al. (2002)]. With this assumption, the equation governing conservation of individual species is given as

$$\frac{\partial C}{\partial t} + V.\nabla C = D\nabla^2 C \tag{1.11}$$

where the second term on the left hand side in Eq. (1.11) is the convective mass transfer term and the right hand side is the diffusive mass transfer term. Equation (1.11) includes only ordinary diffusion and advection according to Fick's Law. It also assumes a constant diffusion coefficient, and neglects any other forms of species transport such as electromigration or thermodiffusion.

A dimensionless form of the mass transfer equation can be obtained by substituting the following variables in Eq. (1.11)

$$\vec{V} = \overrightarrow{V^*}U\,,\ \vec{\nabla} = \overrightarrow{\nabla^*}\left(\frac{1}{a}\right),\ \tau = \frac{Dt}{a^2},\ c = \frac{C_i - C}{C_i - C_s} \tag{1.12}$$

Where U is the characteristic flow velocity, a is the characteristic dimension (channel diameter), D is the molecular diffusion coefficient, and in the case of simple dissolution of a solute in the flow, C_i is the flow's unperturbed concentration and C_s is the solute concentration. The mass transfer equation is then simplified as below

$$\frac{\partial c}{\partial \tau} + Pe(V^*.\nabla^* c) = \nabla^{*2} c \tag{1.13}$$

where, Peclet number ($Pe = \frac{Ua}{D}$) is an important dimensionless group which characterizes the ratio of convective to diffusive mass transfer.

From Eq. (1.13) it can be deduced that at very low Pe the convective term becomes negligible and diffusion is the dominating means of mass transport while at very large Pe the right hand side becomes negligible compared to the left hand side and convection becomes important. With moderate *Pe* values, common in microreactors studied in this thesis work, both convective and diffusive mechanisms exist. It is noteworthy that the Peclet number is similar to the Reynolds number except that the diffusion coefficient is used in place of the kinematic viscosity. For typical aqueous solutions, the diffusion coefficient is approximately three orders of magnitude lower than the kinematic viscosity. The result is that microfluidic flows characterized by low Reynolds number, may have much higher Peclet numbers. Thus the momentum equation is diffusion dominated, whereas the species transport equation contains both advective and diffusive components [Probstein (1994)].

1.2.2 Multiphase Microfluidics

Multiphase flows are created when two or more immiscible fluids come into contact. The immiscible phases can take different forms such as suspending droplets in a continuous phase or cross-channel spanning slugs or liquid films deposited on channel walls. These different forms can be achieved depending on interactions among acting forces such as surface tension, viscosity, inertia and gravity forces. In static conditions with negligible gravity forces two phases are in equilibrium if the pressure in both phases is uniform and only differs at the interface due to capillary pressure given by Young-Laplace equation [Probstein (1994)].

$$\Delta p = \gamma\left(\frac{1}{R_1}+\frac{1}{R_2}\right) \tag{1.14}$$

where γ is the surface tension coefficient and R_1, R_2 are the radii of curvature of the surface along any two orthogonal tangents. Interfacial tension either increases or decreases the liquid pressure in comparison to the ambient (i.e. second phase) pressure. The schematics in Figure 1.3 show two fluids in equilibrium with a solid wall. When a static fluid interface comes into contact with a wall (a solid, third phase) two equilibrium configurations are possible depending on the surface and fluid properties; 1) the fluid interface does touch the wall and forms a contact line between the three phases and 2) One fluid wets the solid surface in form of an adsorbed film separating the other fluid from the wall [Günther et al. (2006)]. In the first case, a contact angle (θ) exists which is the angle at which the three phases coincide. The contact angle, θ, is related to interfacial energies of the solid phase, *'s'* and two fluid phases *'1'* and *'2'* by Young's equation given below [Günther et al. (2006); Probstein (1994)]

$$\gamma_{12} \cos(\theta) = \gamma_{1s} - \gamma_{2s} \qquad (1.15)$$

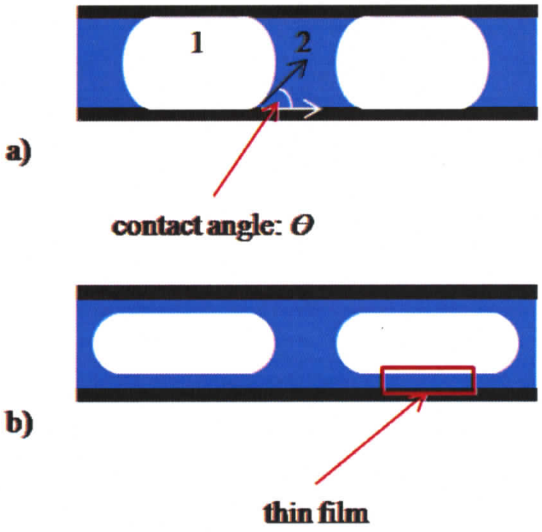

Figure 1.3 Schematic illustrating multiphase flow in microchannels. a) Immiscible fluids and the microchannel wall form a three phase contact line. The contact angle Θ is the angle at which the three phases coincide. b) One fluid phase is wholly contained within the other fluid that wets the solid surface completely.

In dynamic conditions (i.e. where a multiphase flow occurs) however, the dispersed phase velocity adds a third inertia force to the system. [Günther et al (2006)]. The addition of inertia in multiphase microfluidic flows brings complexity to the possible interactions among the governing forces. These complex interactions are responsible for formation of several possible flow patterns inside microchannels.

Many flow patterns have been described for multiphase flow in capillaries [Suo and Griffiths (1964); Taitel et al. (1980); Triplett et al. (1999); Kreutzer (2005); Günther et al. (2006)]. Most flow regimes are based on the microscopy observation, imaging, and using image analysis to distinguish different flow patterns [Triplett et al. (1999); Günther et al (2006)]. Possible flow patterns for a gas-liquid flow in a capillary where the liquid forms the continuous phase, that is the liquid wets the solid surface in its entirety [Günther et al. (2006)] have been studied [Barajas et al. (1993); Zhao et al. (1993); Triplett et al. (1999); Coleman et al. (1999); Zhao et al. (2001); Kawahara et al. (2002), Serizawa et al. (2002); Kreutzer et al. (2005); Cubaud et al. (2004); Günther et al (2006); Zhen hua et al. (2007)]. The flow patterns are described as follows

A "*bubbly flow*" pattern can be seen when non-wetting small bubbles of a gas are dispersed in a continuous wetting liquid. This pattern is observed for low gas fractions and in moderate liquid velocities, in such conditions bubble coalescence is minimal and bubbly flow pattern is observed.

A "*segmented flow*" pattern, (sometimes called Taylor flow, plug flow, slug flow, bubble train flow or intermittent flow) is the flow regime of succession of large long bubbles which take up most cross-section area of the channel. The bubble (or liquid slug) lengths may be determined by manipulating the inlet conditions (i.e. gas and liquid flow rates) [Kreutzer el al. (2003); Garstecki et. al. (2006)].

A "*churn flow*" occurs in segmented flows at much higher velocities. In that case a chaotic flow pattern results. The onset of churn flow is signalled by small bubbles appearing at the rear end of the bubbles.

An "*annular flow*" pattern occurs with small liquid fractions at very high velocities. This flow pattern consists of a wetting liquid film flowing on the wall while a high-velocity flow of gas (and potentially very small droplets of liquid) flow in a continuous fashion through the center.

It is notable that in some publications different names have been adopted to describe the flow patterns and/or higher numbers of flow patterns are proposed. However, the most commonly discussed flow patterns, and associated terminology, are those described above.

Most of the observed flow patterns presented above are transient [Günther et al (2006)]. To predict the multiphase flow pattern under different flow conditions, phase maps have been developed which are independent of channel geometry and classify multiphase flows according to only the superficial velocity of each immiscible phase [Barajas et al. (1993); Zhao et al. (1993); Triplett et al. (1999); Coleman et al. (1999); Zhao et al. (2001); Kawahara et al. (2002); Serizawa et al. (2002); Kreutzer et al. (2005), Cubaud et al. (2004); Günther et al (2006); Zhen hua et al. (2007)]. Superficial velocity is defined as time averaged flow rate of each phase divided by the cross-section area.

The segmented flow pattern which consists of bubbles or droplets of a liquid dispersed in an immiscible continuous phase is the most common pattern in multiphase microfluidic devices, including segmented flow microreactors. Formation of droplets or bubbles in a segmented flow depends on the value of capillary number [Garstecki et al. (2006)]. Capillary number is a dimensionless group relating viscous and surface tension forces given by

$$Ca = \frac{\mu U}{\gamma} \tag{1.16}$$

where μ is the dynamic viscosity, U is the characteristic velocity and γ is the interfacial tension. In low Ca number flows typical of microfluidics, the breakup of the dispersed phase occurs due to the pressure rise in continuous flow and not due to shear forces [Garstecki et al. (2006)]. The commonly employed method of initiating segmented flow in a microfluidic channel is shown schematically in Figure 1.4. When two immiscible liquids come to contact in a microfluidic T-channel the dispersed phase emerges as a small droplet in the main channel where the continuous phase flows. The droplet then starts growing inside the main channel while moving downstream and forms a small neck. In the meantime, the pressure in the inhibited flow upstream of the emerging droplet rises. Finally, at a critical pressure the neck formed in the dispersed phase breaks and the droplet moves downstream [Garstecki et al. (2006)]. The injection of a gas as the dispersed phase (i.e. bubble) is similar to that of an immiscible liquid (i.e. droplet) [Garstecki et al. (2006)]. The key difference between gas-liquid systems and liquid-liquid systems is the characteristic surface tensions (for typical gas-liquid systems, as compared to typical liquid-liquid systems). The relative size of the dispersed droplet/bubble with respect to the separating continuous phase is primarily a function of flow rates [Garstecki et al. (2005); Garstecki et al. (2006)].

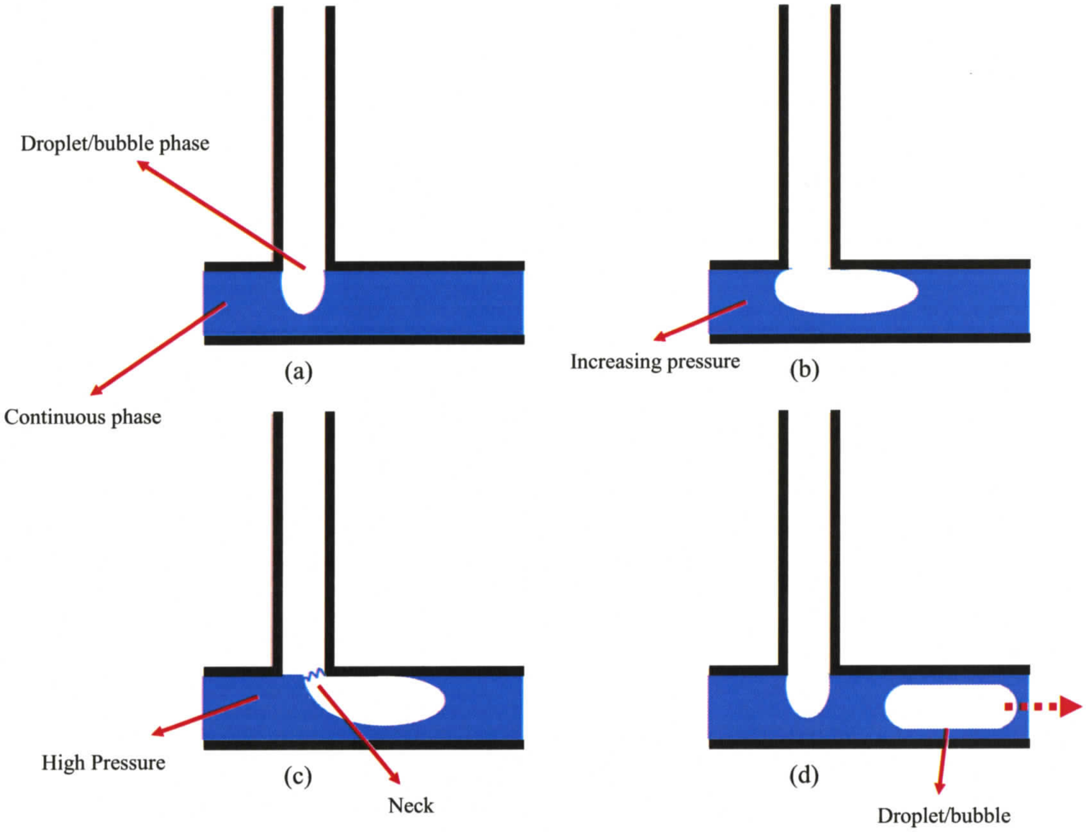

Figure 1.4 Schematic illustration of droplet/bubble formation in microchannels. (a) The droplet/bubble phase enters the main channel. (b) The droplet begins to form and grows downstream. (c) The droplet grows to block the entire cross-section of the main channel, increasing the pressure in the continuous phase until the neck of the droplet breaks. (d) The droplet moves downstream and the cycle is repeated

The flow of a long bubble inside a capillary is a classical problem in fluid mechanics. Figure 1.4 shows a typical gas-liquid segmented flow where the liquid phase wets the capillary wall. Bretherton (1961) first analyzed the hydrodynamics of bubble flow inside capillaries and thus it is referred to as the Bretherton problem. Prior to such hydrodynamics analysis and considerations, bubbles in capillaries were used as markers for measuring liquid velocity inside the capillaries. Fairbrother and Stubbs (1935) first noticed the deposition of a liquid film around a moving bubble in a capillary. From a continuity point of view this means that the bubbles travel at a higher velocity than the surrounding liquid [Thulasidas et al (1995); Thulasidas et al (1997); Kreutzer et al (2003)]. The relative velocity between the bubble and the liquid phase was shown to be a function of capillary number [Fairbrother and Stubbs (1935); Thulasidas et al. (1997)]. Later, Bretherton employed a lubrication analysis for the transition region between the spherical bubble cap and the flat liquid film and drew a relationship for the film thickness and pressure drop across a bubble as a function of capillary number. He also validated his analytical solution experimentally by measuring the film thickness via measurement of reducing volume of a moving liquid slug as it left a thin film behind.

Another unique characteristic of segmented flow is the circulating advection within the liquid slugs which is induced by the shear forces from the channel walls. Taking the moving liquid plug as the point of reference/observation, the flow is circulating as shown schematically in Figure 1.5. Taylor (1961) for the first time proposed three different streamline patterns for liquid phase in front of a moving bubble. He proposed three different streamline patterns for three different ranges of relative velocity of the bubbles and the surrounding liquid. Later his suggested circulating streamlines were verified experimentally, numerically and analytically [Cox (1964); Kolb and Cerro (1991); Thulasidas et al. (1995a); Thulasidas et al. (1997)].

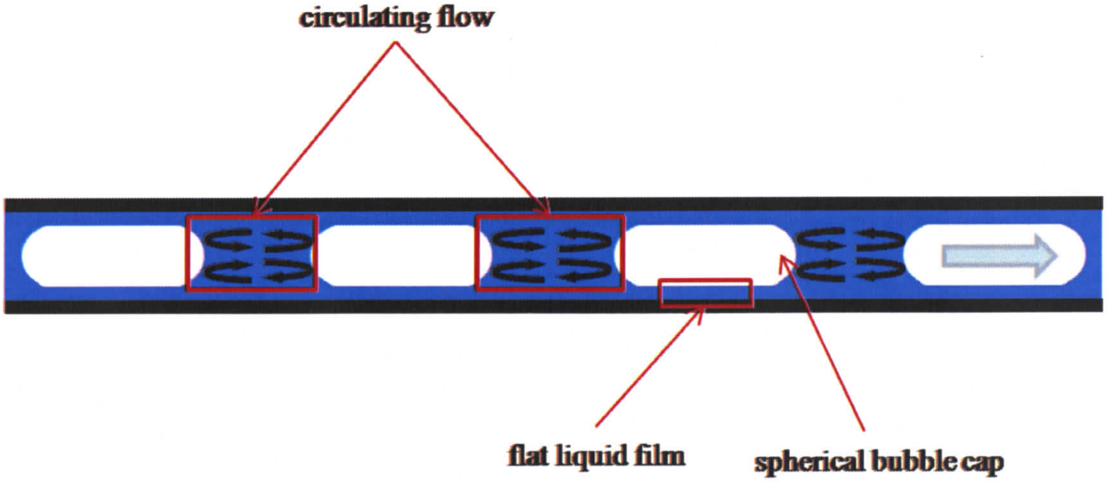

Figure 1.5 Schematic illustration of segmented flow inside a microchannel. The liquid film surrounding the bubbles, bubble cap and the recirculating flow pattern within the liquid plug are as indicated.

1.2.3 Residence Time Distribution in Reactors

Residence time distribution (RTD) is an important parameter in the characterization of mixing and flow behaviour in chemical reactors [Fogler (2006)]. The main benefit associated with RTD is that it enables real chemical reactors to be compared to the ideal situation in which each fluid element (or reactant) experiences the identical conditions and duration in the reactor. The two major uses of the residence time distribution to characterize reactors are: (1) to diagnose problems of reactors in operation; and (2) to predict conversion or outlet concentrations in existing available reactors when a new reaction is used in the reactor [Fogler (2006)]. The time it takes for a liquid element to flow through a reactor system is called the *residence time*. The function that describes in a quantitative manner how much time different fluid elements have spent in the reactor is called the residence-time distribution function [Fogler (2006)].

The RTD is generally determined by tracer tests. Specifically, a tracer material is injected at the reactor's inlet and then the tracer concentration is measured over time at a fixed location downstream [Folger (2006); Günther et al. (2006); Kreutzer et al. (2005); Günther et al. (2004)]. The observed experience of the tracer is used to characterize and analyze mixing and flow behaviour within the reactor. Dirac pulse injection of tracer and step injection of tracer are the most commonly employed methods. Figure 1.6 shows the pulse and step tracer injection methods for RTD measurement and their respective responses. Given a perfect pulse injection (or 'disturbance') the RTD can be expressed by means of the distribution function,

$$E_t = \frac{C_e(t)}{\int_0^\infty C_e(t)dt},\ E_\theta = E_t\tau,\ \theta = t/\tau \quad \tau = \int_0^\infty tE_t dt \tag{1.17}$$

where $C_e(t)$ is the concentration distribution over time at the reactor exit, E_t, is the distribution function evaluated from the tracer response at the exit of the reactor, E_θ is the reduced form of the distribution function once normalized by the mean residence time, τ.

The RTD function, E_t (t), is a probability distribution of residence time of fluid elements (reactants) inside a reactor. In other words, the fraction of fluid elements which have spent a time t inside the reactor is given by E_t (t).

In the case of step injection of tracer at the inlet, the cumulative residence time distribution curves result from the outlet concentration divided by the tracer inlet concentration C_0 which is assumed to be constant with time. The cumulative RTD definition and its relationship with RTD are given in Eq. (1.18).

$$F_t = \frac{C(t)}{C_0},\ F_t = \int_0^t E_t dt,\ F_\theta = \int_0^\theta E_\theta d\theta \tag{1.18}$$

The physical significance of the cumulative distribution function is the fraction of molecules exiting the reactor that have spent a time t or less in the reactor.

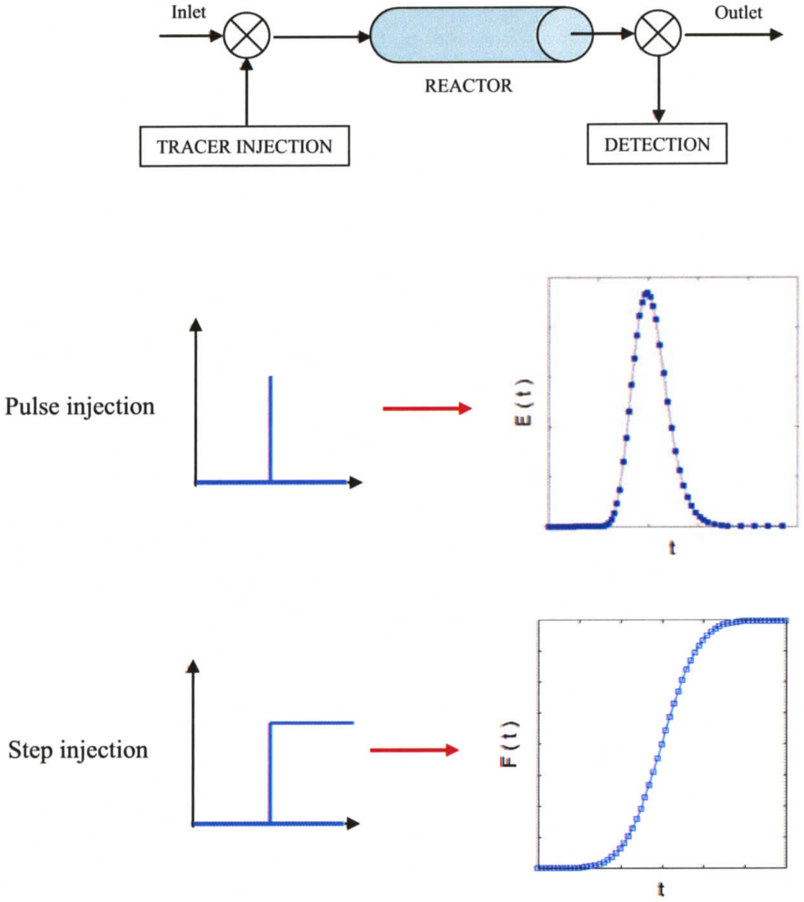

Figure 1.6 Schematics showing pulse and step tracer injection methods for RTD measurement and their respective responses. E(t) is the RTD function and F(t) is the cumulative RTD function.

1.3 Microreactors and Residence Time Distribution Overview

Microfluidic reactors are central to a number of biological and chemical applications [Günther et al (2006); Stone at al. (2004); Beebe et al. (2002); Squires et al. (2005); Tüdos et al. (2001); Kreutzer et al. (2005); Diao et al. (2006); Haeberle et al. (2007); Köhler et al. (2004)]. As compared to their macroscale counterparts, microfluidic reactors can provide several advantages including multiplexing, rapid mixing, environmental control, high pressures, and, they may be applied to small volumes of reactant or scaled-up to produce large volumes [Jensen (2001); Johnson et al. (2002); Stroock et al. (2002); Hertzog et al. (2006); Munson et al. (2005); Gobby et al. (2001); Schabas et al. (2008)]. Typical single-phase pressure-driven microreactors rely on cross-stream diffusion and suffer from high axial dispersion; specifically the cross-stream velocity gradients result in a non-uniform residence time within the reactor, and can lead to heterogeneities in reaction product.

Multiphase flow-reactors, also called segmented flow reactors, have been shown to greatly enhance mixing efficiency and reduce axial dispersion [Song et al. (2003); Günther et al. (2006); Günther et al. (2004); Kreutzer et al. (2005)]. Both these benefits stem from the partitioning of reactants into discrete plugs or droplets. Early multiphase microreactors employed immiscible liquids such as oil and water [Song et al. (2003); Tice et al. (2003); Zheng et al. (2004); Song et al. (2006)]. In these cases, the oil fully wet the microchannel surface and surrounded the aqueous phase as droplets. The oil phase was distributed liquid plugs joined by a thin film, and thus continuous. The aqueous phase was discretized as unconnected droplets, and thus dispersed. These reactors have found many applications, particularly in aqueous chemistry and biological microenvironments [Gadd et al (2008); Zheng et al. (2004)]

As an alternative to immiscible liquids, gas-liquid segmented flow reactors have been developed [Günther et al (2004); Yen et al (2005)]. The gas-liquid segmented flow is more versatile in terms of the range of chemistries that can be used in a microreactor. Gas-liquid segmented reactors are more desirable for reactions that take place in high temperatures since high temperatures tend to increase the miscibility of immiscible liquids [Yen et al (2005)]. Moreover, uniform gas-liquid segmented flows occur in a wide range of flow conditions and channel dimensions without the addition of surfactants [Günther et al. (2004)] while liquid-liquid segmented flows may be operated only over a narrow range of velocities [Song et al. (2003); Shestopalov et al (2004)]. Furthermore, in gas-liquid segmented flow the liquid phase is the continuous phase and it is possible to add additional reactants to the reacting liquid or remove a fraction of it in a controllable way [Yen et al. (2005)]. In these reactors the gas makes up the dispersed phase and the liquid makes up the continuous phase. This is commonly referred to as Taylor flow [Taylor (1961)], and is not to be confused with Taylor dispersion which is a product of single phase flow [Taylor (1953); Taylor (1954)]. Gas-liquid segmented flow reactors have been employed in a number of applications such as micro total analysis systems [Garstecki et al. (2006); Chen et al. (2007)], colloidal particle synthesis and assembly [Yen et al. (2005); Günther et al. (2004); Khan et al. (2004); Schabas et al. (2008b)] and monolithic catalytic chemical reactors [Kreutzer et al. (2005); Roy et al. (2004); Dudukovic et al. (2002)]. In the most common configuration, the reactions of interest take place in the liquid, continuous phase. The gas serves to divide the liquid plugs, however, a thin film of liquid remains. The only mechanism for transfer of mass from one slug to the next is by diffusion from the slug to the lubricating liquid film surrounding the gas bubbles, and subsequent diffusion from the film to the next liquid slug. [Kreutzer et al. (2005)].

The adverse effect of axial dispersion in microreactors has motivated extensive numerical and experimental research in quantifying the degree of axial mass transfer in both single phase and multiphase reactors [Kreutzer et al. (2005); Günther et al. (2004)]. Residence time distribution (RTD) has been widely employed as a measure of axial dispersion in microreactors. Levenspiel and smith (1957) developed an analytical solution for the RTD in single phase flow. Several analytical models have also been developed for axial dispersion in multiphase flow, based on mass transfer between bulk and film regions in liquid slugs [Pedersen (1981); Thulasidas et al. (1999)]. A variety of experimental methods for RTD measurement have been developed and applied to single phase flow reactors [Lohse et al.(2008); M. Günther et al. (2004); Bošković (2008)]. Many parameters influence RTD including the effects of film thickness, bubble and slug lengths and gas and liquid velocities on axial dispersion [Berčič et al. (1997); Salman et al. (2004); Muradoglu et al. (2007); Salman et al. (2005)]. As compared to single-phase reactors, reduced axial dispersion of the continuous phase in a Taylor flow regime has been demonstrated [Günther et al. (2004); Khan et al. (2004); Trachsel et al. (2005)].

1.4 Size Control of Quantum Dot Nanoparticles in Segmented Flow Reactors

One Section of this thesis focuses on size control and breakup of nanoparticles within a gas-liquid segmented flow microreactor. This microreactor was developed and tested in UVic microfluidics lab for the self-assembly of Quantum Dot (QD) nanoparticles, in collaboration with the Moffitt Group (UVic Chemistry), and Joe Wang in particular. Here, a brief description of these particles and the self assembly method is provided with detailed information available elsewhere [Schabas (2007); Schabas et al. (2008a); Schabas et al. (2008b)].

The size-dependent optical and electronic properties of semiconductor and metal nanoparticles make them unique elements for a wide range of new materials and devices [Schabas et al. (2008b)]. Quantum Dots are semiconductor nanoparticles (usually 1-10 nm in diameter [Pinaud et al. (2005)]) with distinct optical properties when compared to bulk semiconductor materials [Krishnadasan et al. (2004)]. Quantum dot nanoparticles have previously been applied as fluorescent bio-labels [Wang and Moffitt (2004)], lasers [Marsh et al. (2000)], solar cells [Nozik (2002)], and light emitting diodes [Park et al. (2001)].

However, widespread application of these particles in photonics, sensing, and biological labelling will require the controlled self-assembly of Quantum Dots into complex colloidal structures with hierarchical organization [Schabas et al (2008b)]. Particle size control strategies for this particular nanoparticles system have involved manipulation of reagent concentrations and addition rate of reagents within the microreactor [Schabas et al. (2008a); Schabas et al. (2008b);Yusuf et al. (2007a)].

However, improved methods offering finer control over the sizes and polydispersities of colloidal QD assemblies are required for various future applications [Schabas et al. (2008b)]. The excellent mixing properties and narrowed RTDs offered by gas-liquid segmented microfluidic reactors are attractive in the context of this particle self-assembly application.

1.5 Microfabrication

When the field of microfluidics was first developing, microfabrication techniques from the microelectronics industry where employed to develop the microfluidic structures [Madou (1997); McKechnie (2006)]. The materials used in the early fabrication processes were silicon and glass. Photolithography, micromachining and etching are common methods to create microscale patterns or grooves on a glass or silicon substrate [de Mello (2002); Quake et al, (2000); Duffy et al. (1998)]. The substrates containing microsize grooves were then enclosed via anodic or fusion bonding of a flat substrate to form enclosed microchannels [Duffy et al. (1998)]. These early methods were expensive and time consuming and the mechanical properties of the materials imposed problems in the fabrication process and limited the range of geometries that could be developed [Quake et al. (2000); Duffy et al. (1998)]. As a result of these limitations, a great deal of effort was focused on using alternative materials and fabrication techniques, particularly those that could be translated to mass-manufacturing.

Replication-based techniques (casting, embossing, and injection molding) for fabrication of microstructures in polymer materials were developed as cheap, quick and efficient alternatives to former methods [Duffy et al. (1998)]. Polymer materials proved to be a unique alternative due to their very low cost, tunable physical and chemical properties [deMello (2002); McKechnie (2006)], and their potential for mass-manufacture. Replication methods are based on transfer of patterns from a negative master to a polymeric substrate [Becker and Locascio (2002)]. The major drawback to replication methods is that any defect on the negative master will be passed on to the polymeric substrate and hence it is very important to fabricate an effectively flawless master. This process can be costly and time consuming. However, mass manufacturing using such techniques is quite straight forward and this benefit generally justifies the cost of initial master fabrication. Soft lithography which is the microfabrication method used in this thesis is a two step process: 1) Rapid prototyping and 2) Replica molding.

1.5.1 Rapid Prototyping

Rapid prototyping is the soft-lithography step through which desired patterns are fabricated on a substrate through photolithography, and is shown in the first three steps of Figure 1.7. A layer of photosensitive material, photoresist, is spun and baked on a substrate which is usually made of glass or silicon. A photomask with the desired channel pattern is designed using a computer aided design (CAD) software package. Care must be taken to assure that the desired pattern remains transparent on the photomask while the rest of the design is hatched in black to block the UV exposure. The designed photomask is then printed on transparency. The substrate already coated with photoresist is exposed to collimated UV light with the photomask on top. Areas of the substrate which are exposed to UV light will polymerize after a post-exposure baking step. The unexposed photoresist is then washed away and the template is ready. The entire process of rapid prototyping can be finished in a few hours depending on the photoresist thickness and complexity of the microstructure to be fabricated. A photoresist template fabricated for the microreactor studied in this thesis work is shown in Figure 1.8a.

1.5.2 Replica Molding

Following the fabrication of the template, a prepolymer is added on top of the template inside a container, as shown in the fourth step in Figure 1.7. The prepolymer is then cured and removed from the substrate. Of the polymers available, polydimethylsiloxane (PDMS) has become popular due to its many attributes. PDMS provides high-accuracy replication of the template patterns, [Quake et al. (1998)], is cheap, is molded easily, can endure high temperatures [de Mello, (2002)], and may be removed from the template surface easily without damaging either surface. PDMS is also transparent to visible light and much UV, making it compatible with flow visualization and fluorescence techniques [Becker and Gartner (2000)].

Once molded and removed, as shown in the fifth and final step in Figure 1.7, the channels can be enclosed either reversibly or irreversibly depending on the application and surface properties needed. Reversible sealing methods take advantage of elasticity of PDMS and channels are enclosed by a conformal contact between the microchip containing channels and a flat substrate such as PDMS, glass, cellophane or silicone tape [McDonald et al. (2002)]. Reversible sealing is suitable for low pressure applications (<5psi). For higher pressure applications, a strong irreversible sealing is required. It has been shown that plasma oxidization of PDMS surface brought into contact with a similarly plasma oxidized flat substrate made of PDMS, glass and some other materials can seal the chip permanently [Duffy et al (1998); McDonald et al. (2000); McDonald et al. (2002)]. A irreversibly sealed PDMS chip employed in this work is shown in Figure

1.8b. In that case, the top PDMS slab is bonded to a PDMS layer previously spun onto a glass microscope slide.

It has been suggested that plasma oxidization of PDMS breaks down the Si – CH_3 methyl groups on the surface of PDMS and replaces them by Si – OH silanol groups. The silanol groups form strong permanent Si – O – Si siloxane groups when brought to contact with a surface containing Si – OH silanol groups and hence seal the channels irreversibly [Duffy et al. (1998)]. Moreover, the plasma oxidization of PDMS renders the surface hydrophilic while PDMS is natively hydrophobic. This phenomenon is useful for filling microfluidic chips with aqueous solutions, and in applications where hydrophilic surfaces are required [Duffy et al. (1998)]. However, the surface does returns to its native hydrophobic state with time [Lee et al. (2003)]. To extend the life time of an oxidized PDMS surface it may be submerged in water or another polar organic solution which prevents the diffusion of polar groups from the surface to the bulk and the condensation of silanol groups [Duffy et al. (1998)].

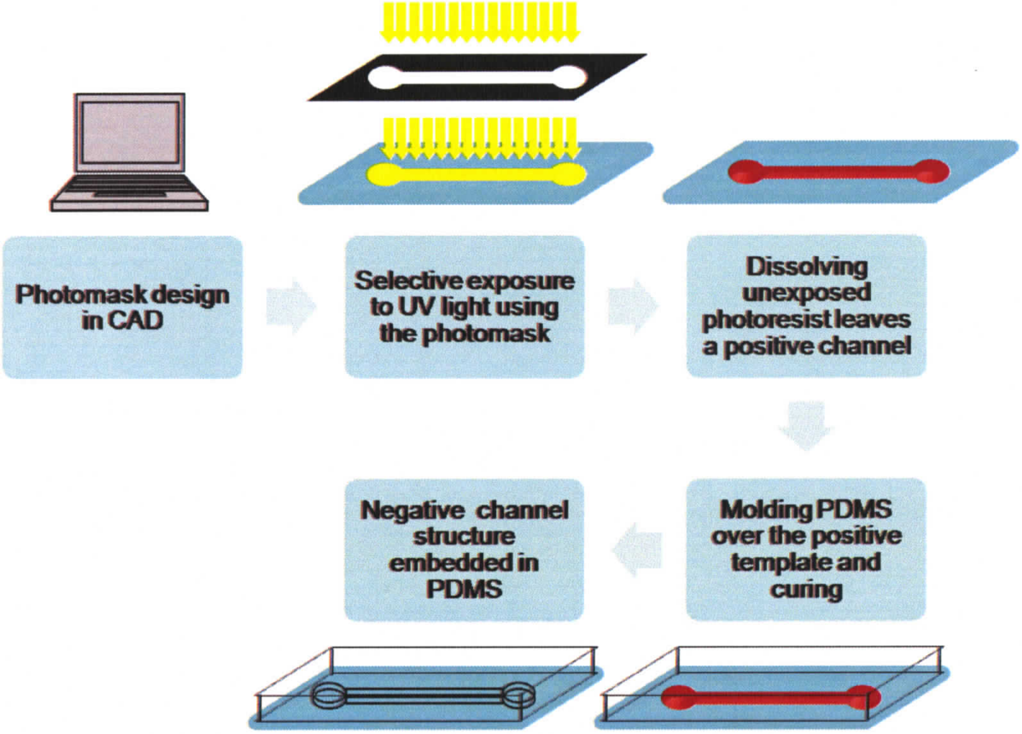

Figure 1.7 Schematic illustrating the soft-lithographic microfabrication process employed in this work. Following the arrows: design of a photomask in a CAD software and subsequent print on transparency; spin-coating of a photosensitive (photoresist) material on a substrate; exposure to UV light through the photomask; dissolving unexposed photoresist and finishing the template; casting PDMS over the finished template and curing, The negative channel structure after the template is removed from cured PDMS.

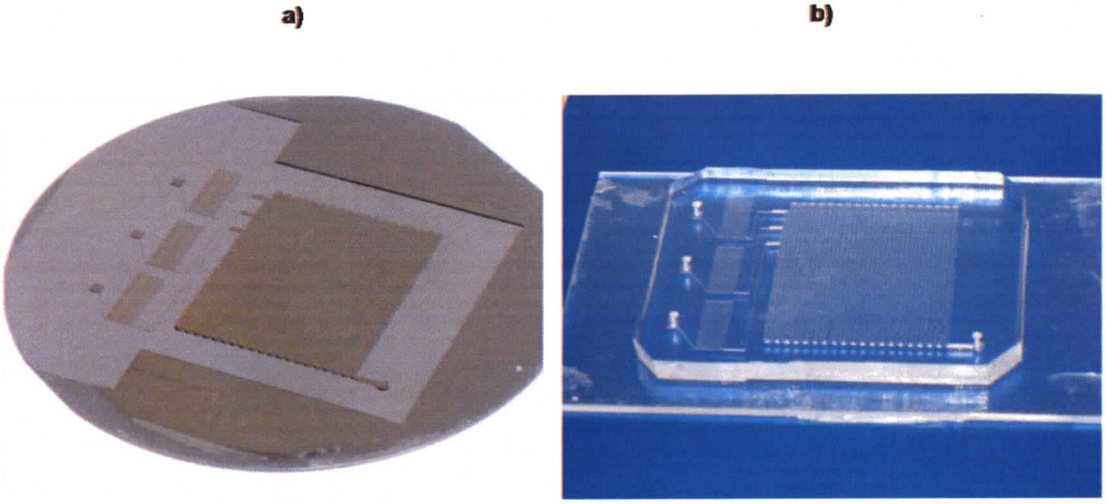

Figure 1.8 Images from the fabrication of: a) a photoresist master (template) fabricated on a silicon substrate via rapid prototyping; and b) A PDMS chip made from replica molding of PDMS onto the template, and subsequent sealing to a PDMS-coated glass microscope slide. The wafer is 3" in diameter.

1.6 Experimental Methods

1.6.1 Fluorescence Microscopy

Flow visualization is an essential tool in studying fluid dynamics and behaviour. Several different visualization techniques have been developed for studying different aspects of fluid dynamics and transport phenomena within fluids. Flow visualization techniques for liquid phase flows can be classified in two major groups; 1) particle based flow visualization methods and 2) scalar based flow visualization methods [Sinton (2004)]. In particle based methods the motion of bulk fluid is concluded from the motion of marker particles. On the other hand, in scalar based visualization techniques, a small amount of a conserved scalar, such as a tracer dye, is injected in the flow and the bulk flow is estimated by observation and imaging of the tracer motion.

Fluorescent microscopy which was first used in biology to visualize components of cells is an important tool for flow visualization in microfluidics. It has been recently used in microfluidic applications where multiple streams exist such as mixing [Oddy et al. (2001); Biddiss et al. (2004); Coleman et al. (2006)] and dispensing [Jacobson et al. (1998); Alarie et al. 2001]. Fluorescence microscopy has been also employed for measuring residence time distribution [Günther et al. (2004); Trachsel et al. (2005); Lohse et al. (2008)] and was used in this thesis work for the same purpose.

Fluorescence microscopy facilitates selective visualization of fluorescent molecules. Fluorescent molecules emit a photon almost immediately when exposed to electromagnetic radiation. When a fluorescent molecule absorbs a photon it enters an excited state. The molecule remains excited for a brief period of time (1 to 10ns) which is called the fluorescent lifetime. The molecule then releases a photon and returns to its ground state. During the interim period the fluorescent molecule loses some of the absorbed energy. Hence the emitted photon is of lower energy and longer wavelength. This wavelength shift, termed the Stokes shift, enables selective visualization of just the fluorescent species. In this way fluorescence microscopy enables microscale flow visualization using scalar (fluorescent dye) and particle (fluorescently-labelled particles) methods [Sinton (2004)]. In this thesis work we employ a solution of a fluorescence material as the tracer in RTD measurement experiments. The fluorescence effect of the tracer enables us to visualize the dispersion and mixing properties of our microfluidic reactors conveniently and with high accuracy.

1.6.2 Working Solution and materials

Tris-Borate buffer (50mM, PH = 8.5) was prepared and used as the continuous phase in the segmented flow experiments. A 4mM solution of fluorescein (Invitrogen Inc., ON) in the same buffer was used as the tracer in all RTD measurement experiments. Argon was used as the gas phase in all segmented flow experiments. To adjust the surface properties of the PDMS chips, a 25mM solution of Octadecyltrichlorosilane (OTS)(Sigma Aldrich, Oakville, ON) in Hexadecane (Sigma Aldrich, Oakville, ON) was prepared and used. In addition, the microfabrication involved poly (dimethylsiloxane) PDMS (SYLGARD, Dow Corning Corporation, Midland, MI), SU-8-50 and SU-8-100 photoresists and SU-8 developer solution (4-hydroxyl-4-methyl-2-pentanone) (Microchem, Newton, MA).

1.6.3 Experimental Apparatus

Liquids were pumped into the microchannels using syringe pumps (Harvard Apparatus, QU). Glass syringes (Hamilton gastight series, NV) were used to deliver the working liquids to the microchannels (in two different sizes: 250 µL and 1000 µL). Argon gas was introduced to the microchannels from a pressure regulator (Johnston Controls Inc) connected to a Q-sized argon tank (Praxair Inc, ON). Teflon Tubing and fittings of 1/16 inch outer diameter (Upchurch Scientific, WA) were used to connect the syringes to the microchannels and the microchips to each other. The tubing was inserted in the microchannels punched inlets and outlets. The tubing connections were friction-fit and sealed reversibly due to the elasticity of PDMS. The microchips were observed using an inverted microscope (DMI 6000B, Leica). Images were captured using a charge-coupled device (CCD) camera (Orca AG) installed on the microscope. The experimental apparatus and setup are shown in Figure 1.9. The inverted microscope platform is convenient for these types of experiments as it leaves the top surface open and available for access with tubing, pipetting and/or electrodes etc.

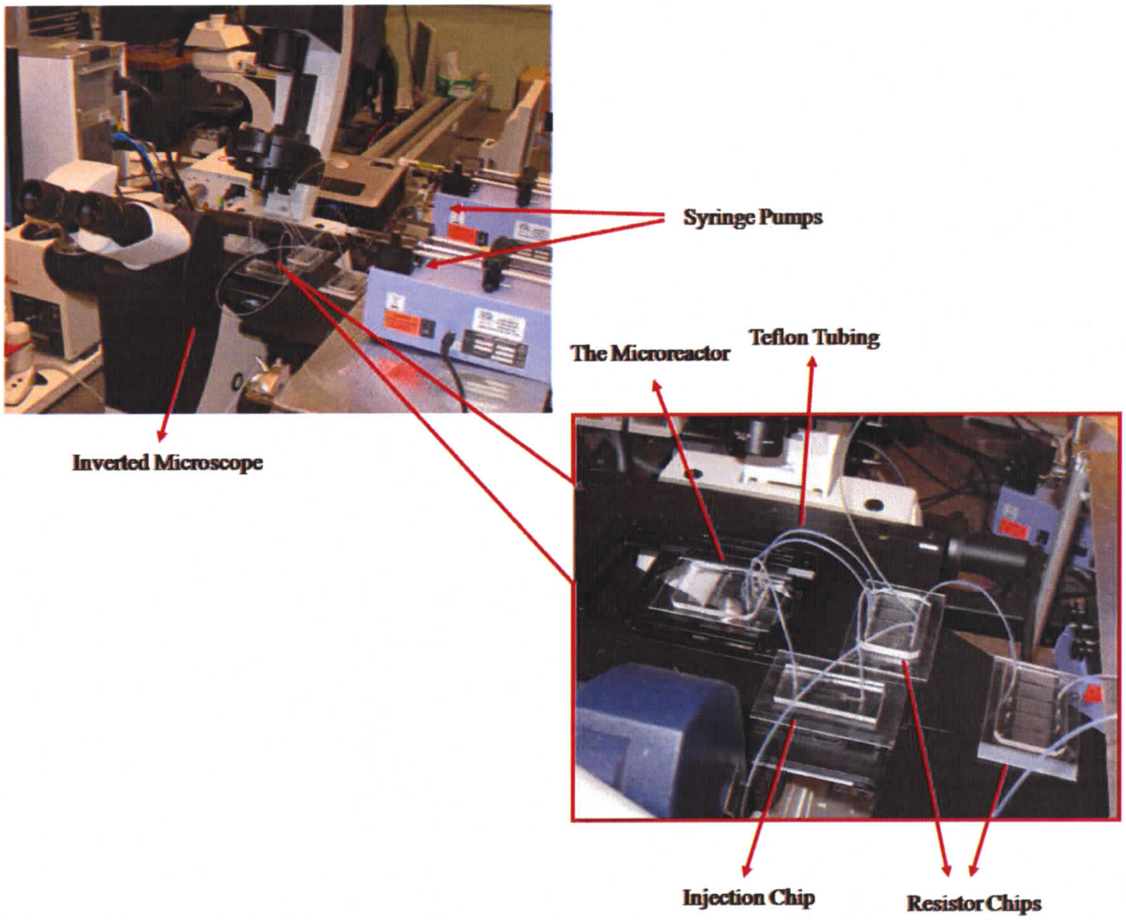

Figure 1.9 Labelled images of the experimental apparatus. The inverted microscope and syringes mounted on syringe pumps (top) and the microscope platform; fabricated chips set up and connected using Teflon tubing (bottom).

A fluorescent filter cube (Semrock, NY) installed on the microscope transmits the excitation light to the microscope stage and to excite the fluorescein inside the microchannels. The Stokes-shifted emission from the excited fluorescein is then imaged through the microscope, onto the CCD camera. The excitation and emission filters along with a dichroic mirror inside the filter cube cause the selective transmission of specific wavelengths which is basic to fluorescent microscopy. Figure 1.10 illustrates the optical function of a fluorescence filter cube. The excitation wavelength (in blue) passes through the excitation filter and is reflected by the dichroic mirror to excite the fluorescein inside the microchannels. The excited fluorescein emits a longer wavelength (in green) which is transmitted by the dichroic mirror and also the emission filter and is captured by the CCD camera.

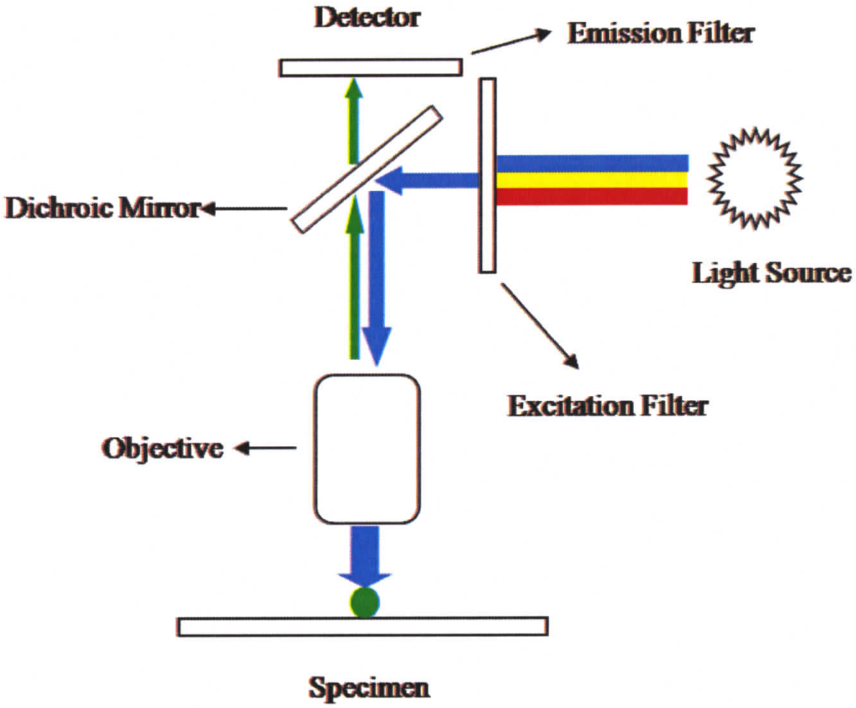

Figure 1.10 The schematic illustrates the optical infrastructure that enables fluorescence microscopy. The excitation and emission filters transmit only the wavelength required for fluorescein excitation and emission. The dichroic mirror in the middle is transparent to the longer wavelength while it reflects the shorter wavelength from the light source.

1.6.4 Image processing

The fluorescence images taken from the CCD camera are raw images. To extract fluorescein concentration data from the images, they must be normalized with respect to a bright- and dark–field image. Normalizing images also eliminates unwanted imaging artefacts from the raw images. Such artefacts include noise, non-uniformity in excitation light, nonuniformity in background light, shadows, curved interfaces which appear in multiphase flows inside microchannels or marks made on the microchip's surface during the fabrication process. To normalize a raw image, a bright-field image is an image captured when only fluorescein solution (at the maximum concentration employed) flows through the entire microfluidic chip. A dark-field image is obtained when the microfluidic chip contains no fluorescent dye. Accordingly, a fluorescence concentration of unity is assigned to the bright-field image and zero to the dark-field image. Thus, a normalized concentration field, by pixel, may be obtained from each image pixel as follows,

$$C = I_{normalized} = \frac{I_{raw} - I_{dark}}{I_{bright} - I_{dark}} \tag{1.19}$$

where I represents the grayscale intensity of the images, and subscripts *raw*, *bright*, and *dark* correspond to the raw image, the bright-field image, and dark-field image, respectively.

1.7 Numerical methods

Computational fluid dynamics (CFD) is another important tool in studying fluid flows at small scales. The role of CFD becomes more pronounced in complex flow structures where experimental measurements would be too difficult or costly to perform or where supporting data is required to validate experimental data. In CFD, Navier-Stokes equations along with the other transport equations presented in section 1.2.1 (if present in the problem) are solved numerically over a discretized solution domain.

There has been tremendous amount of numerical work on multiphase microreactors despite the fact that these reactors emerged relatively recently as an alternative to macro scale reactors [Kreutzer et al. (2003); Salman et al. (2004); Kreutzer et al. (2005b); Jensen et al. (2006); Ajaev et al. (2006); Özkan et al. (2007); Kashid et al. (2007); Muradoglu et al. (2007)]. The numerical solutions have focused on different aspects of multiphase flow in microchannels such as hydrodynamics, bubble formation and interface shapes [Kreutzer et al. (2005b); Ajaev et al (2006); Jensen et al. (2006); Özkan et al. (2007); Kashid et al. (2007)] and heat and mass transfer [Kreutzer et al. (2003); Salman et al. (2004); Kreutzer et al. (2005b); Muradoglu et al. (2007)].

Different sets of assumptions and simplifications have been reported in modeling segmented flow numerically. A common assumption is to neglect the gas phase due to its small viscosity and density with respect to the liquid phase. This assumption is suitable in problems where only a solution in the liquid phase is required [Kreutzer et al. (2003); Kreutzer et al. (2005b); Kashid et al. (2007)]. The gas-liquid interface in this case is modeled as a moving boundary on the liquid domain. The geometry of this boundary is in general a function of the velocity fields, however, an assumption of a fixed interface shape is reasonable for very low capillary number flows.

Capillary numbers typical of microfluidic reactors considered in this work are on the order of 10^{-04}, and thus considered low. Low capillary numbers, according to Bretherton (1961), also result in extremely small film thicknesses. In other words, the gas bubble covers almost the entire channel cross-section, if circular. Another artefact of low capillary number flow is that the bubbles and liquid slugs move at essentially the same velocity [Homsy (1987); Thulasidas (1995)]. However, in typical microfluidic reactors fabricated using the processes described earlier in this chapter, the microchannels are rectangular in cross-section. Thus the liquid film in these channels varies in thickness with the thickest portion at the corner of the channel [Kreutzer et al. (2008)], and even at low capillary number film flow effects can be significant.

1.8 Overview of This Thesis

The contributions of this thesis are outlined below.

In Chapter 1 the background was provided for the entire thesis. The aims and motivations of this thesis were presented. Basic theory behind microfluidics in general and multiphase flows in specific was covered. That analysis included the conservation laws in microscale and also hydrodynamics of microscale multiphase flow. An introduction to microreactors and common methods for measuring residence time distribution within reactors were discussed. Microfabrication methods and soft lithography were introduced next. An overview of the experimental and numerical methodologies employed in this work was provided.

In Chapter 2 a microreactor strategy is developed and fabricated. The single phase and segmented flow RTDs within the reactor are compared and discussed. The microreactor surface is then modified and the effect of surface modification on the RTD of segmented flow within the reactor is investigated.

In Chapter 3, a simplified numerical simulation is developed for gas-liquid segmented flow inside a microreactor. The hydrodynamics of the flow in the liquid phase is discussed. The shear stress distribution in liquid slugs and its potential effect on nanoparticle break up within segmented flow microreactors are discussed.

In chapter 4, methods for fabrication of templates (substrate or master) with very large surface area of the patterns are discussed.

In chapter 5 an overview of major contributions of this thesis and a summary of future work based on findings of the current thesis is presented.

2. Chapter 2: HYBRID PARTIAL-WETTING GAS-LIQUID SEGMENTED FLOW MICROREACTORS

2.1 Introduction

In this chapter a novel multiphase microreactor strategy is developed and tested, and its performance is compared to that of a single phase microreactor and previous multiphase reactor strategies. The approach here is to reduce the wettability of the continuous phase within gas-liquid segmented reactors to achieve partial wetting, and reduced transport between liquid plugs. The schematic in Figure 2.1 illustrates the flow pattern and axial dispersion of a tracer in segmented flows with wetting and partial-wetting microreactors. As shown, partial wetting would result in reduced axial dispersion through the reduction or elimination of the lubricating, connecting film. Pulsed injection and step injection RTD measurement methods are employed here to quantify the degree of axial mass transfer in single phase, and wetting and partial-wetting microreactors. While partial wetting results in increased flow instabilities, in general, parameters for steady well-ordered segmented flow regimes are reported here.

The first strategy employed in this work was to treat the entire microreactor surface such that it was less wetting to the continuous phase. It was found, however, that the resulting microreactors did not provide sufficient stability and repeatability. Specifically, the injection process was the main source of the instability due to the high surface tension between the liquid phase and the channel walls. Since the injection process was very effective with reactors of similar geometry with a more wetting surface, a two-part, or hybrid, microreactor was proposed. The hybrid microreactor presented in this chapter generates segmented flow within a wetting injector channel that transitions, downstream to a less wetting condition.

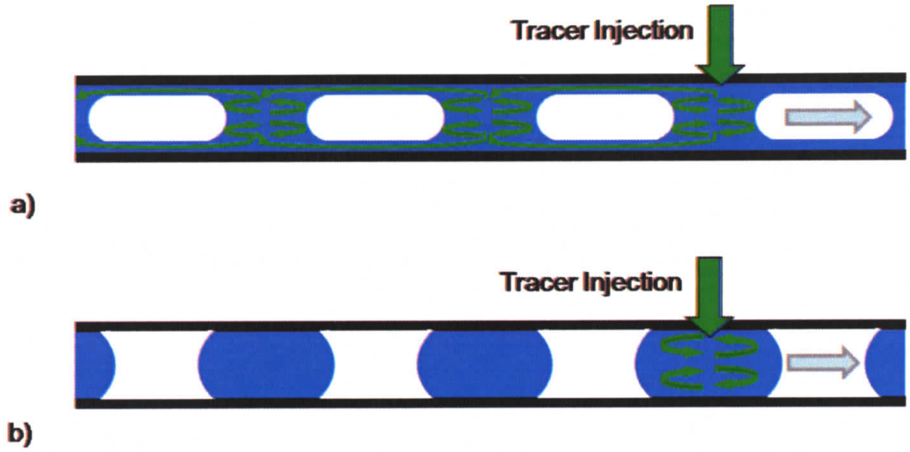

Figure 2.1 Schematic illustrating the role of the film surrounding the gas phase in plug-to-plug transport. a) The through-the-film tracer dispersion mechanism in a wetting microreactor with liquid film. b) Elimination of the lubricating film inhibit tracer dispersion in a reactor with channel surfaces modified to be less wetting.

2.2 Experimental Section

2.2.1. Microfluidic Chips

A schematic of the microfluidic chips employed and the experimental procedure is given in Figure 2.2. The reaction channel used in the current work consisted of a serpentine microchannel 400 μm wide and 150 μm deep. The length of the reaction channel, as fabricated, was very long (1200 mm). In practice the length was set by the position of the punched outlet; the reaction channel was 150 mm long in one case and 300 mm long in the other case. The channel length of 150mm was adopted for initial studies on the effect of surface properties (i.e. hydrophilic, hydrophobic surfaces) on the

RTD in the reactor. The longer, 300 mm length was used for RTD trials. The chip has three inlets, two of them deliver the liquid reactants and the other inlet delivers the gas phase. All three inlets lead to a 200 mm serpentine channel resistor blocks prior to entering the injector. These resistors serve to stabilize the generation of the two-phase flow [Günther et al. (2004), Günther et al. (2006), Fuerstman et al. (2007)]. External resistor chips were also employed to add resistance to the inlet flows for further stabilization. These resistors were 1000 mm long and had the same cross section dimensions as the on-chip resistors. In effect, these high pressure drop resistors serve to efficiently dampen the pressure fluctuations produced by the bubble generation process itself and also from the syringe pumps and the gas tank. Basically, the resistors are designed in a way that the pressure drop in each lane is at least one order of magnitude higher than the pressure drop in the reaction channel [Günther et al. (2006)]. For instance, given a total flow rate of 27μLiter/min, the total flow resistances for the liquid inlet and the gas inlet (including tubing, on-chip resistors and external resistor blocks) were 385 *KPa* and 43.5 *KPa* respectively and as compared to the total flow resistance of the 300 mm reaction channel which was 2.5 *KPa.* Basically, the resistors are desined in a way that the pressure drop in each lane is at least one order of magnitude higher than the pressure drop in the reaction channel [Günther et al. (2006)].

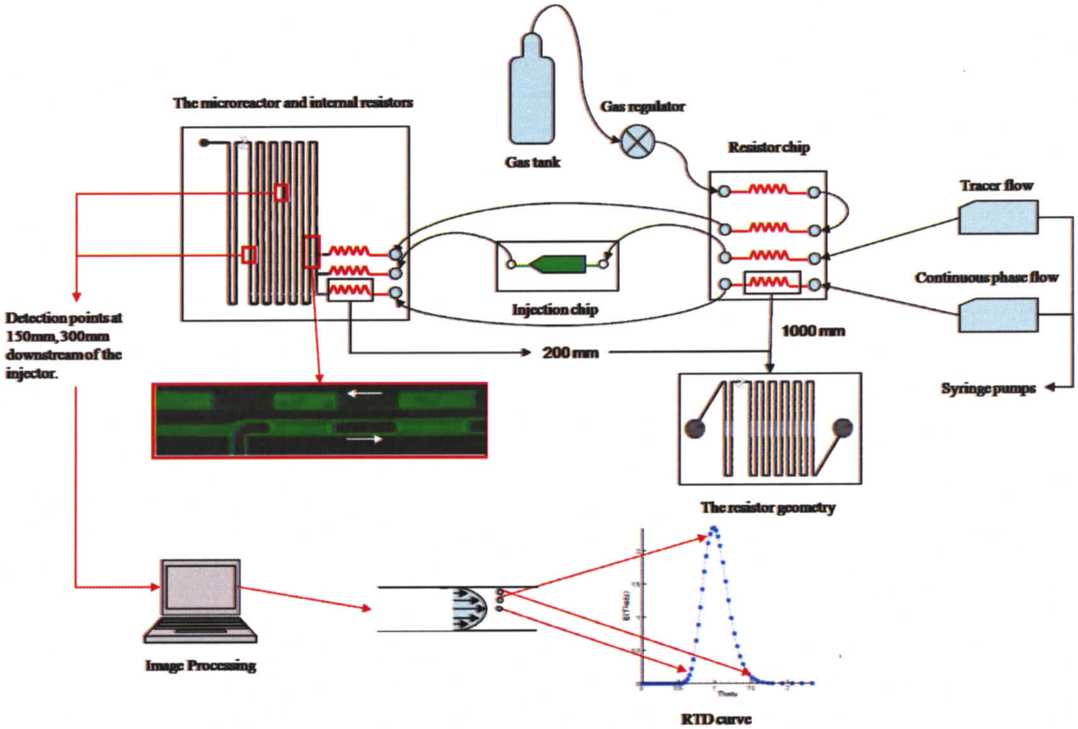

Figure 2.2 Schematic summarizing the experimental setup and procedure. The microreactor chip, the on-chip resistor channels, the external resistor blocks, the injection chip, syringe pumps, gas tank are connected via tubing as shown. The syringe pumps deliver the liquids and the argon tank provides the gas flow via a regulator. The tracer is injected at the inlet by manually depressing the injector chip reservoir, and the transport of the tracer is imaged and the images are processed to determine reactor performance.

2.2.2. Fabrication

The general fabrication method is described in Chapter 1 and the details of large area patterning are described in Chapter 4. Here, only a brief description specific to the microfluidic chips used in this chapter is provided.

The microfluidic chips, and the associated photoresist-based masters, employed in this chapter are shown in Figure 2.3. These chips were fabricated in poly (dimethylsiloxane) PDMS (SYLGARD, Dow Corning Corporation, Midland, MI) using the established soft-lithography technique [Duffy et al (1998), McDonald et al. (2000)].

Briefly, to produce the master (template), photoresist was spin-coated on a silicon wafer (Silicon Quest International, CA) and baked. The baked photoresist was then exposed to UV light through a photo-mask of the microreactor. The exposed substrate was baked on the hotplate unexposed photoresist removed. PDMS and curing agent were degassed in a vacuum chamber (Model 280A , Fisher Scientific, ON) and applied to the pre-patterned silicon substrate.

In order to accommodate on-chip resistor channels with a smaller hydraulic diameter than the microreactor channel, a two-step, two-layer photolithography process was required. The substrate was patterned in SU8-50 (MicroChem Corp. Newton, MA) photoresist for the thinner features (the resistors) and SU8-100 photoresist (MicroChem Corp. Newton, MA) for the thicker features (the reaction channel and the injection chip). The only double-thickness chip fabricated was the microreactor with 50μm thickness for the on-chip resistors and 150μm thickness for the reaction channel. The two-step fabrication process included an initial fabrication of only resistors with thickness 50 μm followed by fabrication of the thicker reaction channels on top of the resistors. The most challenging step of such multi-thickness fabrication process was the alignment of the micro-sized resistor outlets with the reaction channel inlets on the photomask prior to exposure under the UV source. The alignment was critical to ensure that the resistor and reaction channels on the final template were connected.

PDMS was molded on the master and was then cured on hotplate at 85C for 30 minutes. The microreactor was then removed from the mold and the inlets and outlet holes were punched. The holes were 1/16 inch in outer diameter. The microreactor was then cleaned and placed in a plasma cleaner (Harrick PDC 32-G). A microscope glass slide with PDMS-coated surface (a layer of about 100 μm thick) served as a substrate to enclose the negative microchannels within the PDMS chip. Both the microreactor and the coated glass slide were exposed to oxygen plasma for 30 seconds and the treated surfaces were then put together to form chemical bonds and seal the reactor permanently. In cases where a wetting chip surface was desired, the channels were filled with distilled water immediately after plasma sealing.

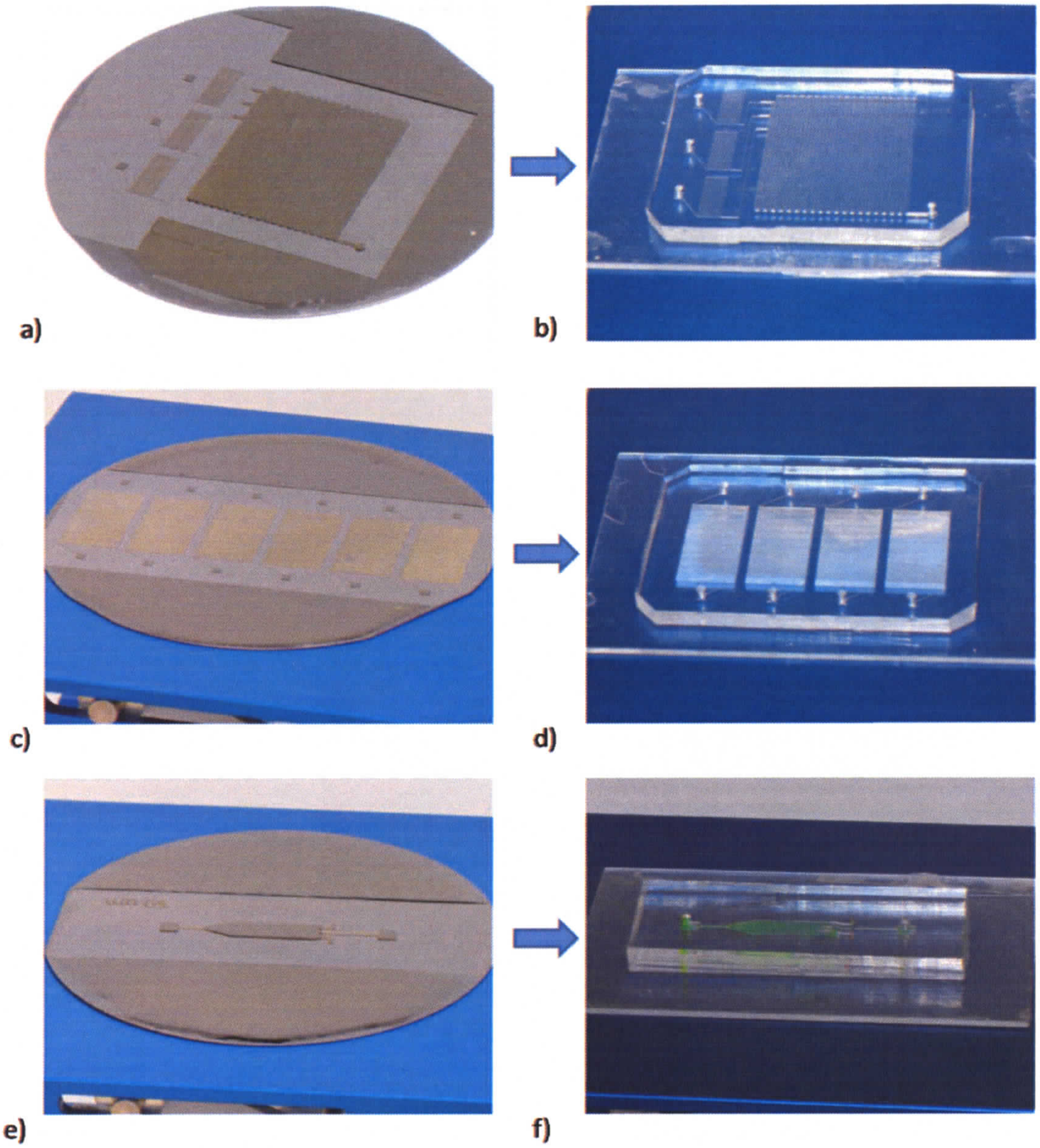

Figure 2.3 Images of the photoresist based masters (on silicon) and associated microfluidic chips. a) The microreactor template fabricated in photoresist on a silicon substrate b) The microreactor fabricated in PDMS c) The resistor chip template fabricated on a silicon substrate d) The resistor chip fabricated in PDMS e) The injection chip template fabricated on a silicon substrate f) The injection chip fabricated in PDMS.

2.2.3. Surface Modification

To render the reaction channel surface hydrophobic, a technique based on self assembled monolayer (SAM) deposition [Doms et al. (2008), Schumacher et al. (2008), Adzima et al. (2006)] was employed. The surface was first oxidized in oxygen plasma for 30 seconds and then a 25mM solution of Octadecyltrichlorosilane (OTS) (Sigma Aldrich, Oakville, ON) in Hexadecane (Sigma Aldrich, Oakville, ON) was introduced via the outlet using a syringe. Prior to reaching the injection channels, the solution was withdrawn via the outlet. The coating procedure took approximately 60 seconds. This procedure enabled modification of the reaction channel while maintaining the original surface characteristics of the injector. Past studies suggest that OTS can silanize the PDMS surface through reaction of tri-chlorosilane groups with Hydroxyl (-OH) groups on the oxidized PDMS surface resulting in grafting of the octadecyl chains onto the surface [Doms et al. (2008), Schumacher et al. (2008), Adzima et al. (2006)]. Here, a lower concentration of OTS solution (25mM) in addition to a brief injection period of 20 s was adopted. This resulted in advancing and receding contact angles of water of 120-130 degrees and 60-90 degrees respectively, which was not as high (i.e. not as hydrophobic) as that used in previous studies. Using higher concentrations and/or injection periods was found to result in overly hydrophobic response, which has been shown previously to result in unstable flow and poor segmentation [Cubaud et al. (2006)]. In addition, over exposure of OTS causes discoloration of the channel, and swelling of the PDMS.

2.2.4. Chemicals

Tris-Borate buffer which contains a mixture of Tris base and Boric acid (c = 50 mM, PH = 8.5) was prepared and used for the flow to ensure unchanging properties for the liquid phase during the experiment. A 4mM solution of fluorescein (Invitrogen Inc., ON) in the same buffer was used as a tracer in the pulse injection RTD measurement experiments. Argon from a Q-sized argon tank (Praxair Inc, ON) was employed as a gas source in gas-liquid segmented flow experiments.

2.2.5 Flow Delivery and Control

Pressure regulation of the gas inlet was enabled by the tank regulator as well as a downstream regulator for fine adjustments (Johnson Controls Inc.). Liquids were delivered to the microreactor using 250 μL and 1000 μL glass syringes (Hamilton gastight series, NV). Syringe pumps (Harvard Apparatus, QU) were used to deliver the liquids. Teflon tubing lengths of 20 cm and 10 cm with 1/16 inch outer diameter and 100 μm inner diameter (Upchurch Scientific, WA) connected the syringes to the resistor chip inlets and resistor chips to the on-chip resistors. The tubing connecting the pressure regulator to the gas inlet was 120 cm long. The liquid flow rates were adjusted via the syringe pumps. The gas flow rate was controlled by tuning the pressure regulator. It is noteworthy that due to the compressible nature of the gas, and lack of flowmeters with accuracy in order of μLiter, the gas flow rates were calculated from the frequency of the bubble formation and the gas bubbles average volume. This method of flow rate calculation has been widely employed in the context of gas-liquid multiphase flow in microscale [Yen et al. (2005); Kreutzer et al. (2008)].

2.2.6 Imaging and RTD Measurement

Fluorescence microscopy was used to visualize the flow through the microreactor. An inverted microscope (DMI 6000B, Leica , NJ) was used to image tracer transport inside the reactor. Image sequences were captured using a CCD camera (Orca AG, Hamamatsu, NJ) installed on the microscope, and the images were imported into MATLAB (Mathworks Inc. Natick MA) for image processing. To normalize the fluorescence images, bright field and dark field images were required as described in Chapter 1. A brightfield image was obtained with the reactor channel filled with fluorescein solution. The darkfield image was obtained by flushing buffer solution throughout.

Initially, the system was filled with buffer and the flow rate was maintained constant. To achieve segmented gas-liquid flow, argon gas was introduced and the gas pressure was tuned to achieve stable segmented flow, and then fixed. The tracer injection channels were was also filled at a low flow rate until fluorescein solution reached the injection point on the microreactor chip. Once any residual tracer in the reaction channel was removed, and the image recording system started, a pulse of tracer is injected manually be a quick depression of the injection chip which is a wide channel (5mm) with a diaphragm-like upper wall. Images of the tracer transport were obtained at steady time intervals of 170-200 ms.

Following image acquisition, the images were organized in a temporal sequence with appropriate time intervals and with t = 0 corresponding to the initial tracer injection. The images were converted from false-color to greyscale mode for image processing in

MATLAB software. A MATLAB code was written to import images one by one and normalize them with respect to the dark and bright field images [Inoue and Spring (1997)]. To obtain the RTD data, fluorescence intensity over a small window at the detection point was recorded in each normalized image. In the single-phase RTD tests, the detection window was 2 mm long, and the width of the channel minus the near edge region where fluorescence signal naturally decreases due to edge effects. The schematic in Figure 2.4 shows the detection window employed in the gas-liquid segmented flow reactor runs. In the gas-liquid RTD tests, the detection window was selected in each image based on the closest liquid plug to the detection point. The length of the detection window in these tests was generally 1-4 mm depending on the liquid plug size. In selecting the detection window, care was taken to avoid the bright spots at the bubble caps that result from total internal reflection at the liquid-gas interface [Sinton et al. (2003)]. The intensity values for all pixels within the detection window were averaged to obtain a single concentration value per image (or time step). The normalized intensity-versus-time data were then analyzed. The RTD curve was found from the following relationship in Eq. (2.1) [Fogler (2006)] :

$$E(t) = \frac{C(t)}{\int_0^\infty C(t)dt} \tag{2.1}$$

Where C(t) is the tracer concentration distribution at the detection point. The RTD expression was non-dimensionalized in time by using the parameter θ, where $\theta = t/\tau$ and τ is the mean residence time within the reactor and is defined as,

$$\tau = \int_0^\infty tE(t)dt \tag{2.2}$$

The dimensionless function $E(\theta)$ was then defined as $E(\theta) \equiv \tau E(t)$ and was plotted as a function of θ where the dimensionless comparison between the RTD curves was required.

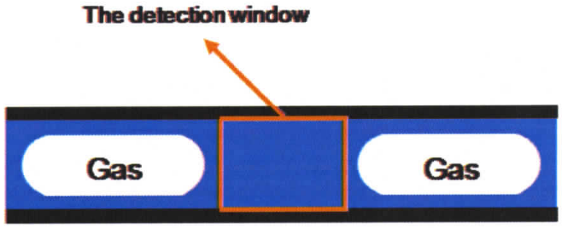

Figure 2.4 Schematic illustrating the selection of the image detection window in the case of gas-liquid segmented flow. Fluorescence intensity was averaged for pixels inside the detection region; $I = \left(\sum_{1}^{n} I_i\right)/n$. Imaging artefacts at the channel walls and the gas-liquid interfaces were avoided.

2.3 Results and Discussion

A single phase microreactor is considered first. Levenspiel and Smith (1965) provided an analytical solution for the non-dimensionalized RTD, $E(\theta)$, in single phase flow. Their solution assumes a straight channel of uniform cross-section and the length of the channel is very long relative to the width of the injected tracer band. The model also assumes that dispersion of the tracer occurs in Taylor dispersion regime [Taylor (1953)]. This assumption suggests that the model is most accurate in Taylor dispersion envelope as presented below

$$7 << Pe = \frac{UR}{D_\infty} << 4\frac{L}{R} \tag{2.3}$$

where Pe is the Peclet number, a dimensionless group, relating the rate of convection of a flow to its rate of diffusion. Other parameters in Eq. (2.3) are U, the characteristic velocity, D_∞, the molecular diffusion coefficient, L and R which are characteristic channel length and radius respectively. The dimensionless parameter emerging out of the analysis by Levenspiel and Smith is the vessel dispersion number ($D^*/J_L L$). The family of normalized RTD curves is given by the following expression,

$$E(\theta)=\frac{1}{2\sqrt{\pi\theta\left(\frac{D^*}{J_L L}\right)}}\exp\left(\frac{-(1-\theta)^2}{4\theta\left(\frac{D^*}{J_L L}\right)}\right) \tag{2.4}$$

where θ is, dimensionless time as is defined earlier, J_L is superficial liquid velocity defined as liquid flow rate divided by the cross-sectional area of the micro-channel, L is the channel length up to the point where the concentration distribution is measured, and D^* is the axial dispersion coefficient. For Taylor dispersion the expression for D^* is given by,

$$D^*=\frac{J_L^2 d_h^2}{192 D_\infty} \tag{2.5}$$

where d_h is the channel's hydraulic diameter and D_∞ is the molecular diffusion coefficient. Figure 2.5 shows the family of normalized RTD curves given in Eq. (2.4). The shapes and trends of the predicted single-phase RTD curves are best explained with a schematic diagram.

The schematic in Figure 2.6a illustrates the role of cross-stream velocity gradients (in the absence of multiphase flow) on dispersion, and the form of the resulting residence time distribution. Here, velocity gradients distort the tracer, and induce concentration gradients in the transverse, or cross-channel, direction. Cross-stream diffusion driven by the cross-stream gradients effectively slows down the tracer particles at the front and speeds up those at the back. At short times, or short channel lengths, where the flow Peclet number does not fall in the envelope given in Eq. (2.3), the convective dispersion regime is dominant rather than the Taylor dispersion. Hence, as the relatively concentrated sample front passes the detector it registers a sharp rise, followed by a slow decline corresponding to the trailing edge. This effect results in the asymmetric form of the RTD at short times (or short channel lengths). On the other hand, at very long times, or long channel lengths, the Taylor dispersion regime prevails where radial cross-stream gradients are relatively small and the cross-stream averaged concentration profile, as observed by the detector, becomes symmetric in the axially direction. As this concentration profile passes a stationary point detector a more symmetric residence time profile is recorded as shown in Figure 2.6a at right.

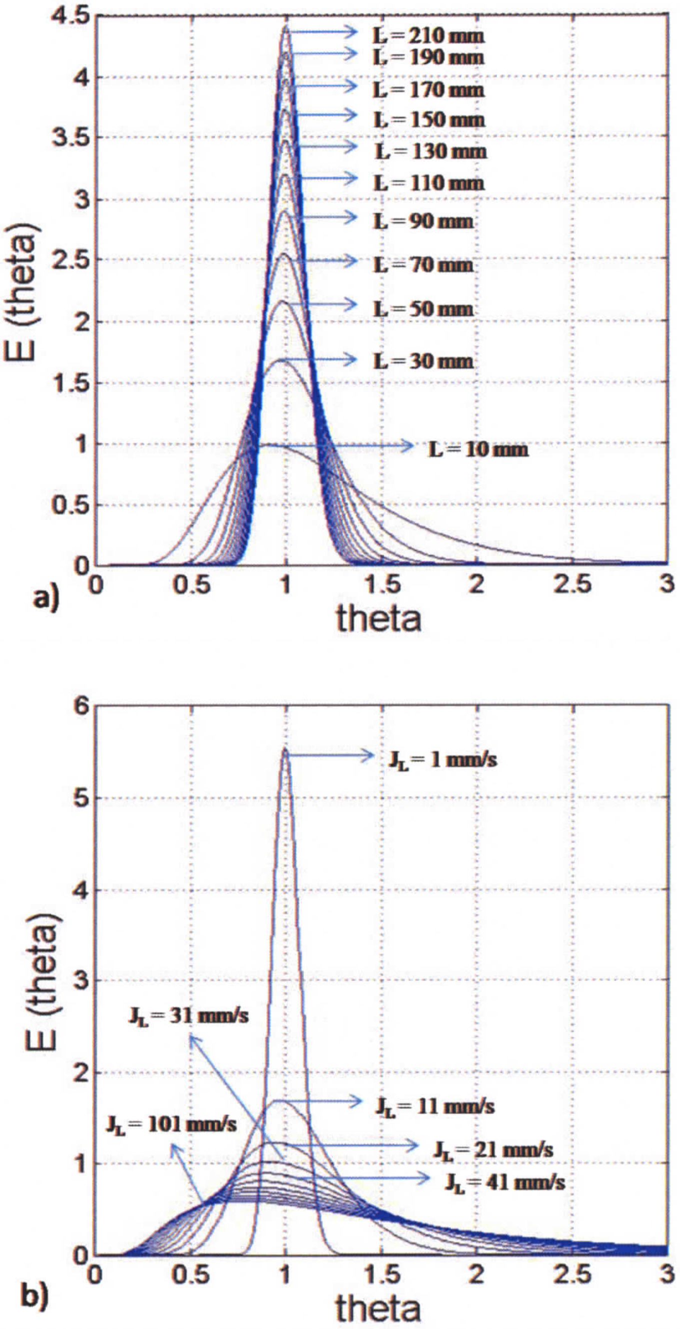

Figure 2.5 Family of normalized RTD curves given in Eq. (2.4) for a) different channel lengths at J_L=2.2 mm/s and b) different superficial velocities (J_L) at L=150mm which is the length of the single phase reactor studied herein.

The measured RTD, $E(t)$, for single phase flow inside the reactor is plotted versus real time in Figure 2.6b. The average liquid velocity, in this single phase case is equivalent to the superficial velocity (i.e. average velocity), J_L = 4.2 mm/s, and the detection region was 150 mm downstream of the injector. The normalized RTD, $E(\theta)$, is plotted in Figure 2.6c with the corresponding analytical solution of Levenspiel and Smith (1965). Although it is difficult to compare the results directly due to ideal assumptions made in the analytical model, it is encouraging to note that there is a reasonable agreement between the analytical solution and the experimental data as shown in fig. 2.6c. The full width at half maximum (FWHM) is used here to compare the RTD curves. FWHM is a measure of the extent of a function given by the difference between the values of the independent variable at which the dependent variable equals to half of its maximum value. The analytical solution predicts a full width at half maximum (FWHM) value of 0.40, as compared to 0.57 determined from the experimental data. The experimental RTD, however, exhibits more asymmetry than the analytical curve. This asymmetry observed in the experimental data is attributed to finite sample size and non-ideal injection effects, not included in the analytical model, and associated finite length effects as shown schematically in Figure 2.6a. Asymmetry in single-phase microreactor RTD is common in single phase reactors with shorter channel lengths than required for Taylor dispersion regime. [Lohse et al. (2008), Bošković (2008), M. Gunther et al. (2004), Khan et al. (2004), Günther et al. (2004)].

It is noteworthy that other measures such as shape parameter for fitting functions like Weibull function can also be employed to capture and compare shape information for different RTD curves.

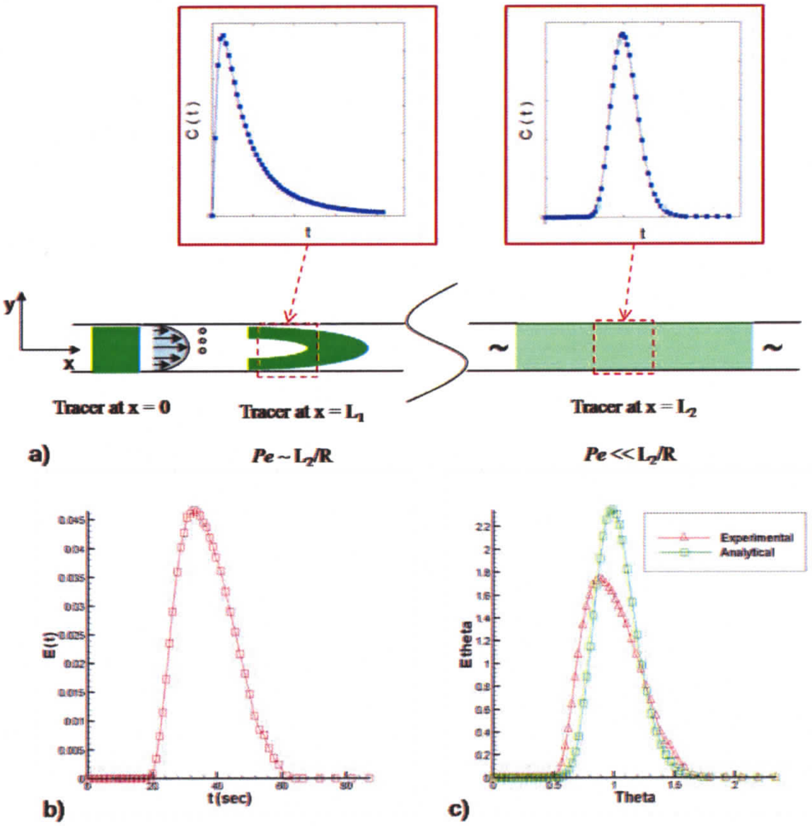

Figure 2.6 Single phase microreactors schematic of transport and RTD and experimental data. a) Schematic showing tracer dispersion in single phase flow at short times (short channel length) and long times (long channel length). As shown the RTDs are asymmetric at short channel lengths and become symmetric at very long channel lengths due to the action of Taylor dispersion. b) Experimentally determined RTD curve for single phase reactor at L = 150mm downstream of injection point; J_L=4.2 mm/s. c) Normalized residence time distribution curves at L=150mm, J_L=4.2 mm/s, for both the experimental results and the analytical solution; Analytical □ Experimental Δ.

The result of adding a dispersed gas bubble phase to the single phase reactors of Figure 2.6, is given in Figure 2.7. The reactor in both cases was hydrophilic, and the buffer solution forms the continuous phase with bubbles forming the dispersed phase. A fluorescence image of the multiphase flow is given in Figure 2.7a. The measured RTD,

$E(t)$, for the gas-liquid segmented flow reactor with hydrophilic walls is given in Figure 2.7b. The superficial liquid velocities for the two-phase and single phase flows were J_L = 2.2 mm/s, J_L = 4.2 mm/s respectively. The normalized RTDs for the single and multi-phase reactors are compared in Figure 2.7c. As shown, the RTD for the multiphase reactor is much narrower than the single phase reactor, with FWHM values of 0.10 and 0.57 respectively. This improvement in reactor performance is in agreement with previous works [Günther et al. (2004), Khan et al. (2004), Trachsel et al. (2005)].

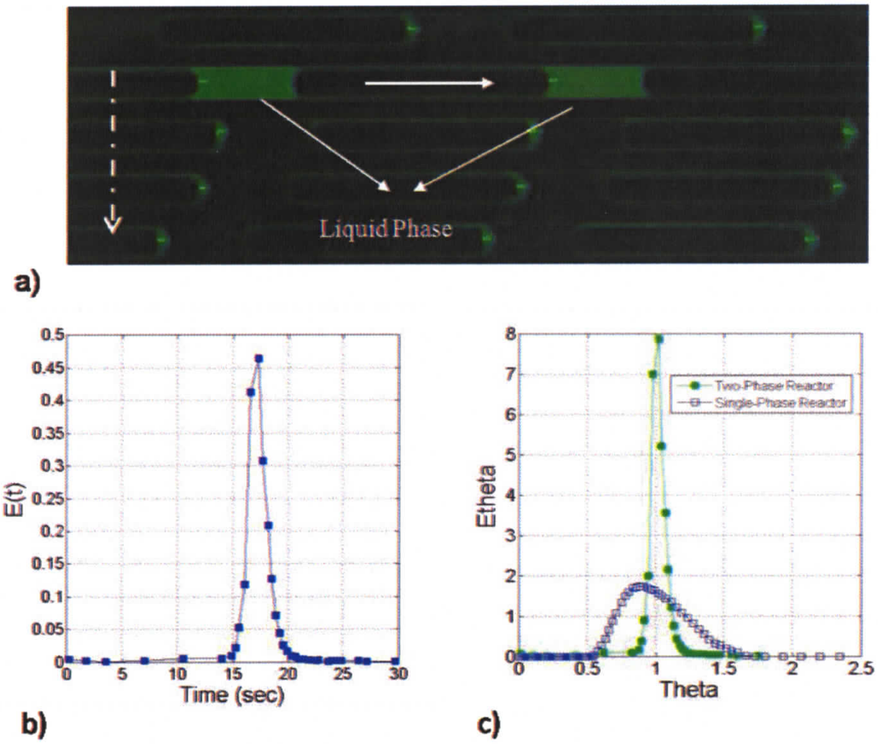

Figure 2.7 Experimental data obtained from the microfluidic reactor (of Figure 2.6) with the addition of a gas phase. The surface properties in this case were the same as those of the single-phase reactor that is, wetting. a) Segmented flow inside the wetting reaction channel following the pulse injection of tracer. b) RTD curve for the segmented flow at L = 150mm, J_L = 2.2 mm/sec, J_G = 5.5 mm/sec. c) Normalized RTD curves for the single phase and segmented flow reactors with mean residence times τ_m=37.3 s, and τ_m=16.9 s, respectively.

While the addition of a gas phase results in significant narrowing of the residence time distribution, the liquid film connecting the plugs does enable mass transport between plugs and thus decreases microreactor performance. The connecting film thickness depends on the liquid and surface properties, and is commonly very thin (sub micron) in circular cross-section channels. Monolithic microreactor microchannels are more commonly rectangular in cross-section, resulting in relatively thick film in the corners [Thulasidas et al. (1999); Kreutzer et al. (2008)]. The approach here is to minimize the film thickness, or disconnect the liquid plugs, by altering the surface properties of the reactor. PDMS provides readily tunable surface properties. Initial work focused on uniformly hydrophobic treatment of the microreactor chip. It was found, however, that a hydrophobic channel surface at the injector resulted in unstable flow and poor gas-liquid segmentation. Instead, a hybrid approach was adopted where introducing and subsequently removing the OTS solution via the reactor outlet enabled selective coating of the microreactor channel surface while keeping the injector channel hydrophilic.

Figure 2.8a, b depict the segmentation in the wetting injector channel followed by, transition to discrete liquid slugs downstream where the channel surface switches to a less wetting condition. It is observed that the interface shape for discrete slugs shows a finite contact angle, and the presence of a circumferential contact line.

The nature of the segmented flow pattern inside a hydrophobic reactor can be explained through the analysis of interfacial tensions acting within the reactor [Chen et al. (2007)]. In the context of capillarity and wetting phenomena the wettability of a surface is characterized by a 'spreading parameter', *S*, which is given in Eq. (2.5). A positive value of S $(S > 0)$ corresponds to a total wetting surface while a negative value $(S < 0)$ corresponds to a partial wetting surface [de Gennes et al. (2004)].

$$S = \gamma_{SG} - (\gamma_{GL} + \gamma_{SL}) \tag{2.5}$$

The parameters γ_{SG}, γ_{GL}, γ_{SL} are the surface tensions at the solid/gas, gas/liquid and solid/liquid interfaces respectively. In the fully-wetting case γ_{SG} is much larger than the other two and consequently S has a positive value. As a result, there is no solid-gas surface in the system, and the liquid wets the solid surface throughout. In contrast, in the hydrophobic reaction channel, the increase in solid-liquid surface tension, γ_{SL}, makes S negative and results in a partially-wetting system where all three interfaces exist.

Additional dynamic effects are observed with flow. Specifically, the bullet shape of the liquid plugs is owed to two effects, firstly the Bretherton effect [Bretherton (1961)] where front and back interfaces have different curvatures due to axial pressure drop, and contact angle hysteresis (i.e. a difference between the advancing and retreating contact angle). Referring to Bretherton [Bretherton (1961)], and considering the very low capillary number of the flow (order of 10^{-04}) the Bretherton problem is negligible here and, the contact angle hysteresis effect is the dominant effect in this flow regime.

The hybrid configuration was found to produce a stable segmented flow at a range of flow rates. Figure 2.8c,d show a set of a section of the reaction channel with a sequence of similar plugs for different gas flow rates. Stable plug flow was achieved in the hybrid reactor for all cases for which stable flow was achieved in the fully wetting, hydrophilic, chip. Thus the addition of the hydrophobic surface treatment in the reaction channel, and the elimination of the liquid film, did not result in a considerable loss in stability. The partial-wetting reactor did, however required higher pressure gradients for the similar flow rates. Higher pressures are not an issue for the liquid syringe pumps that provide fixed flow rate, however, the gas pressure needed was significantly higher in the non-wetting case. Specifically, inlet gas pressures of 30kPa and 70kPa were needed to drive an otherwise similar flow/chip in the hydrophilic and hydrophobic reactors, respectively.

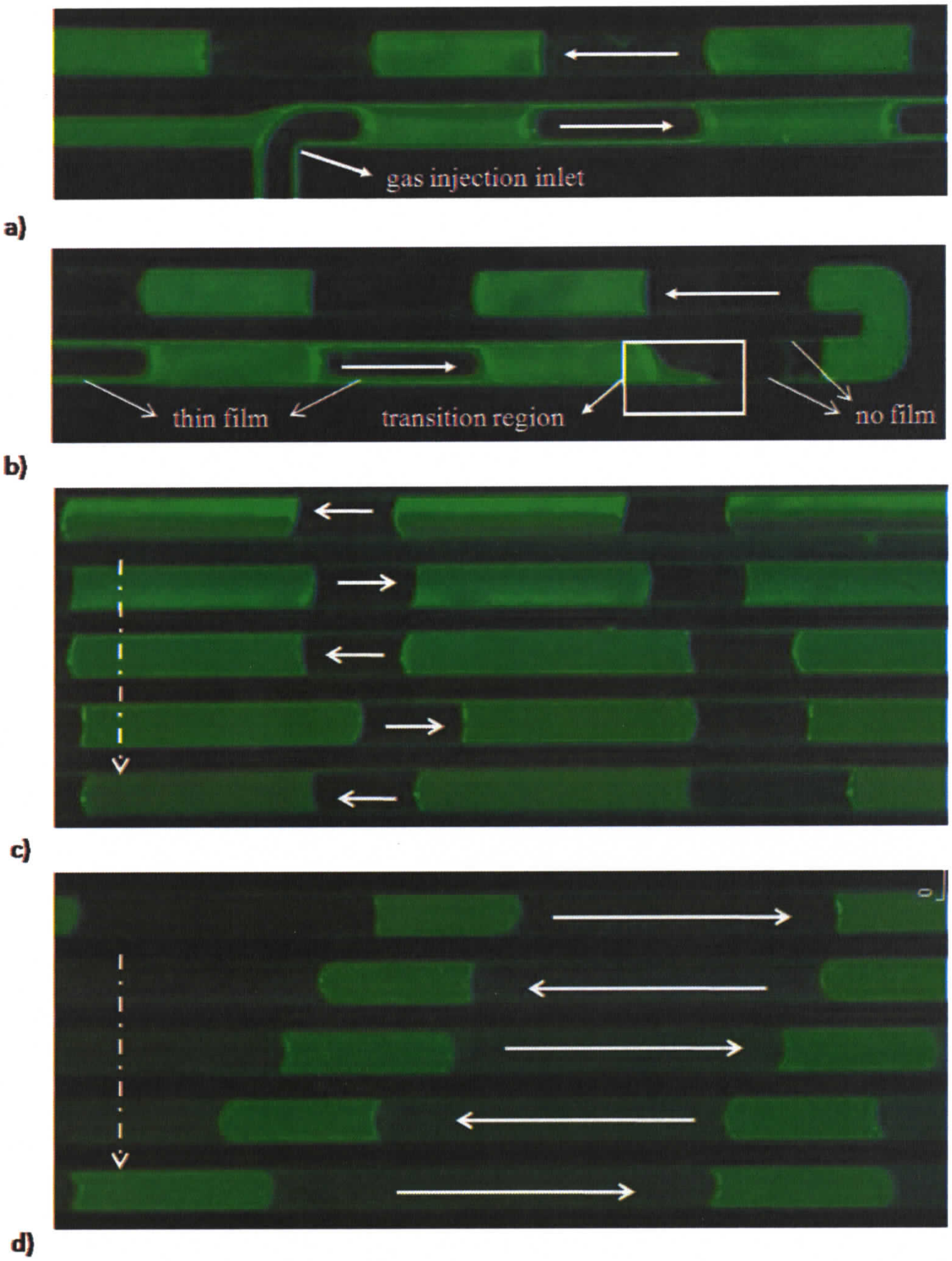

Figure 2.8 Fluorescence microscopy images of the hybrid gas-liquid segmented flow reactor in operation. a) Formation of liquid slugs at the wetting (hydrophilic) injector channel; J_L = 5.3 mm/s, J_G = 6.1 mm/s b) The transition region where the liquid wets the channel surface partially and the thin lubricating film disappears; J_L = 5.3 mm/s, J_G = 6.1 mm/s c) Segmented flow in partial-wetting reaction channel downstream of the injector at J_L = 5.3 mm/s, J_G = 1.7 mm/s d) Segmented flow in partial-wetting reaction channel downstream of the injector at J_L = 2.2 mm/s, J_G = 6.1 mm/s.

Figure 2.9a and b depict liquid slugs flowing downstream of the 300 mm long reaction channel after the pulse-injection of the tracer in wetting and non-wetting reaction channels, respectively. These images are much darker than those in Figure 2.8 as only a small volume of tracer is injected in the RTD tests. The liquid slugs carrying the tracer are brighter in the hydrophobic reactor suggesting that these liquid slugs contain higher tracer concentrations due to the reduced axial dispersion to the other slugs. Ideally, the injection process would result in only one liquid slug containing a fixed concentration of tracer. This was not possible, in practice, and instead a number of liquid plugs (generally 4-5) contained tracer at the injection point.

Figure 2.10 shows the RTD measurement results for the partial-wetting reactor and also for a wetting reactor with the same flow conditions. The RTD function for injection pulse and the response curves are plotted for both reactors. The injection pulse curve is superimposed on the response curve to facilitate comparison between the input and response curves. The discrepancy between the input and response curves provides a measure of axial dispersion in the reactors, and thus a measure of reactor performance. Figure 2.10a shows a much wider response curve than the input curve which implies significant axial dispersion. On the other hand, Figure 2.10b shows an almost negligible difference between the response and input curves which suggests that the axial dispersion is greatly reduced in the modified reactor.

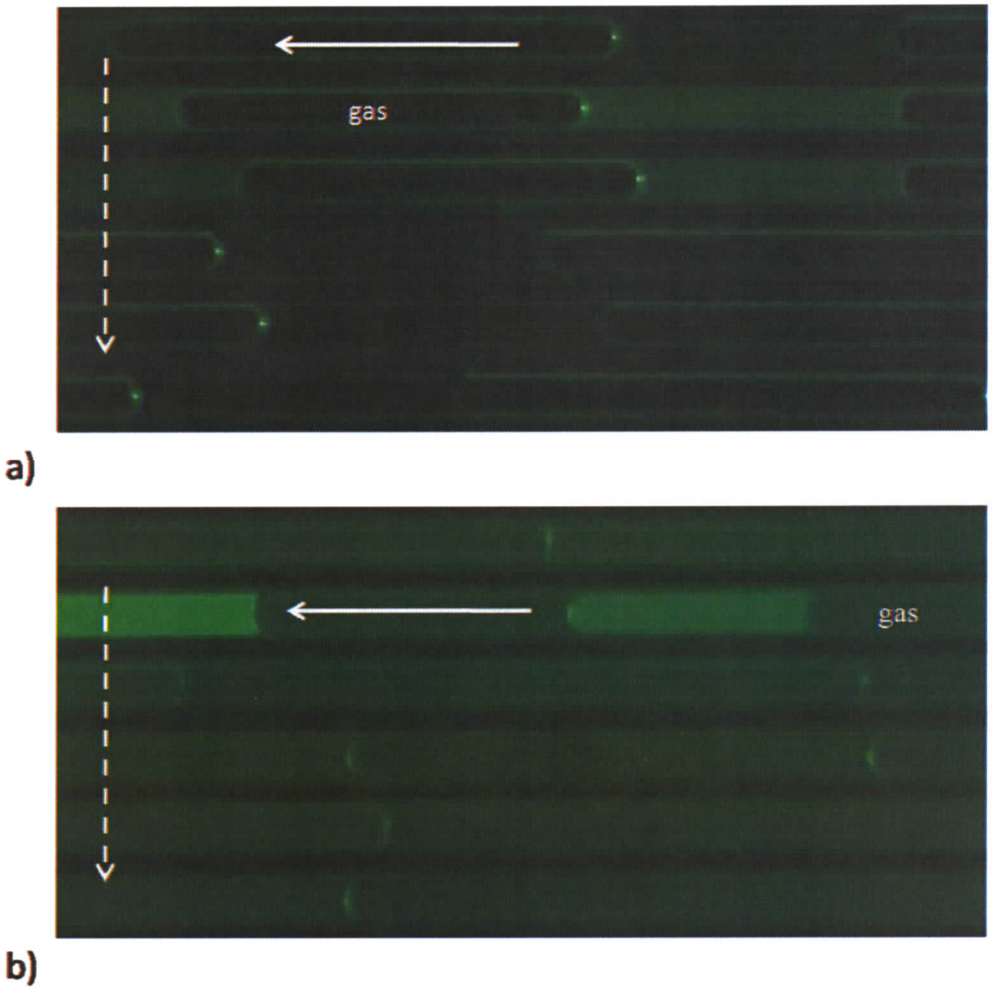

Figure 2.9 Fluorescence microscopy images of different L = 300 mm segmented flow reaction channels with injected tracer. a) Liquid slugs flowing downstream of the reaction channel after the pulse injection of tracer in a) the hydrophilic (wetting) reactor; J_L=2.2 mm/s, J_G=6.3 and b) the hydrophobic (partially-wetting) reactor; J_L=2.2 mm/s, J_G=6.1. It is notable that the liquid slugs carrying the tracer are brighter in the hydrophobic reactor which suggests that the liquid slugs maintain the initial tracer concentration due to the absence of axial dispersion to the other slugs.

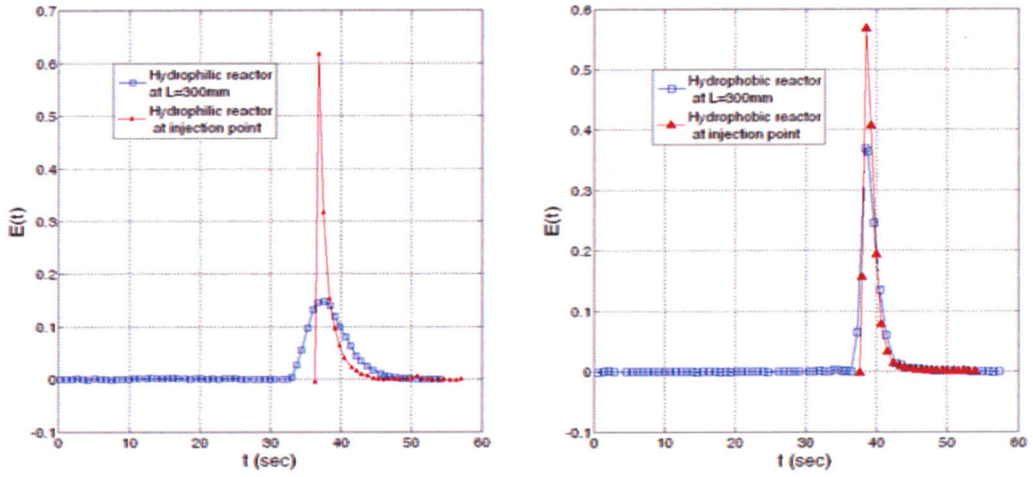

(a) (b)

Figure 2.10 RTD curves for hydrophobic reactor at L = 300 mm downstream from the injection point (blue) and right after the injection point (red) for a) the hydrophilic (wetting) microreactor with the mean residence time, τ_m=37.9 s and b) the hydrophobic (partial-wetting) microreactor with the mean residence time, τ_m=39.42 s. Although the liquid flowrates were identical in both cases, the mean residence time in the microreactors were not exactly the same due to a slight difference in the gas velocity. It is difficult to match gas velocities between runs as only the input pressure may be controlled, and the pressure required is a function of surface properties.

Figure 2.11 compares the non-dimensionalized RTD curves for both reactors. The partial-wetting reactor shows a 63% narrower RTD than the wetting reactor with FWHM values of 0.06 and 0.164 respectively. This suggests that in the modified reactor the separation of the liquid plugs through the reduction/removal of the connecting film results in significantly improved reactor performance. While it is not, with this setup, possible to rule out any plug-to-plug transport, it is apparent that at detection point very little of the tracer has left the initially injected liquid plugs. In the Taylor flow reactor however, the initial liquid segment containing the tracer passes the tracer on to downstream liquid segments through diffusion to the liquid film on the channel walls (see

Figure 2.1). This distributes the tracer and results in a much wider exiting RTD profile than the input pulse.

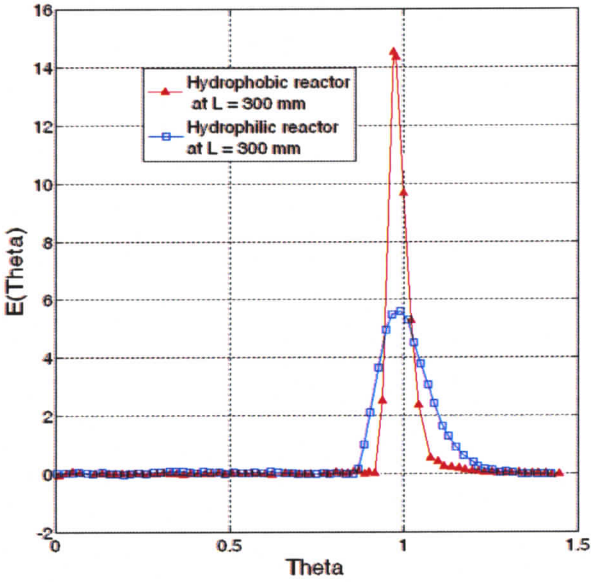

Figure 2.11 Normalized RTD curves for hydrophobic (partial-wetting) and hydrophilic (wetting) microreactors. The FWHM values for hydrophilic and hydrophobic reactors are 0.06 and 0.164 respectively. The difference between FWHM values marks a 63% decrease in RTD width for the hydrophobic microreactor.

In order to study the influence of channel length, RTD measurement tests are performed in hydrophobic and hydrophilic microreactors with a shorter channel length of 150mm. Figure 2.12a,b show liquid slugs flowing downstream of the 150 mm long reaction channel after the pulse-injection of the tracer in hydrophilic and hydrophobic reactors respectively. Figure 2.13 presents RTD measurement results for both hydrophilic and hydrophobic reactors. The hydrophobic reactor shows a 40% narrower RTD than the regular reactor with FWHM values of 0.06 and 0.10 respectively. It is deduced from FWHM values, that for the shorter reactor, narrowing of RTD due to surface modification is not as pronounced as it is for the longer reactor. This modest narrowing is due to the shorter mean residence time which allows shorter time for the tracer to disperse to upstream liquid slugs through the thin film. In the limit of a very short reaction channel, one would expect very little dispersion regardless of the dispersion phenomena present in the flow. Thus, the surface modification method developed here is more effective in longer channel lengths where axial dispersion effects are significant in broadening RTD within hydrophilic microreactors. It is noteworthy, however, that the FWHM values for both 150 mm and 300mm hydrophobic reactors are the same and equal to 0.06 which emphasizes the repeatable dispersion-minimizing behaviour of such reactors.

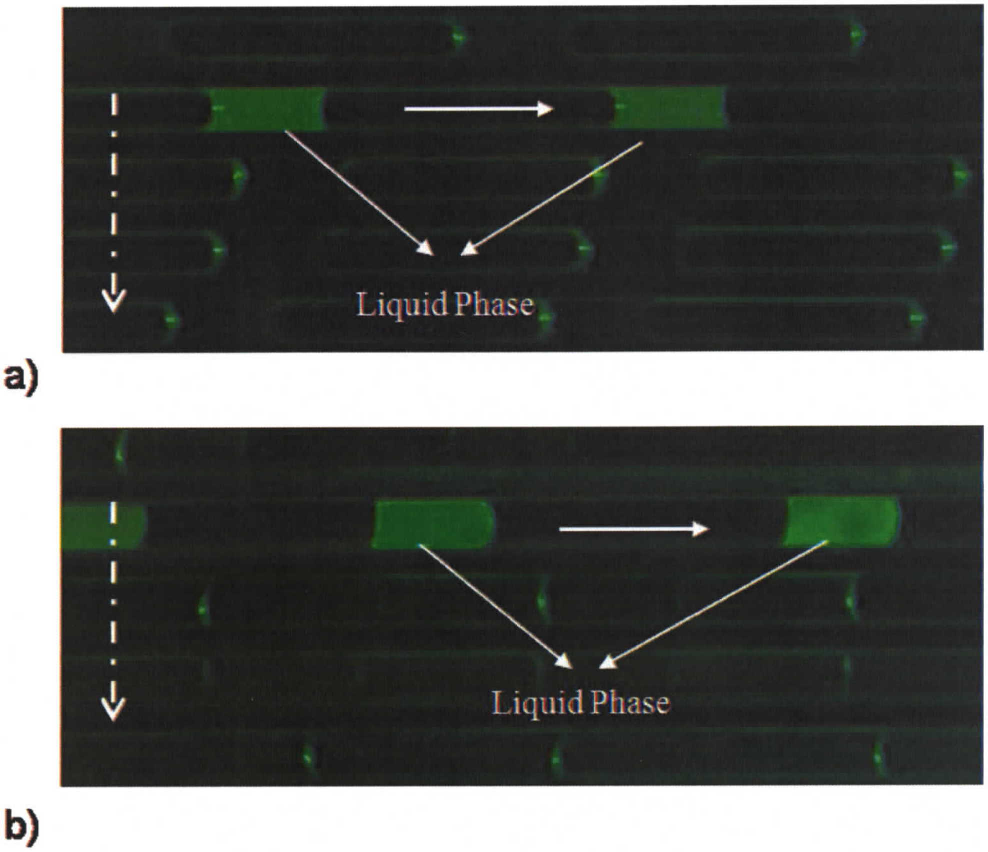

Figure 2.12 Fluorescence microscopy images of different L =150 mm segmented flow reaction channels with injected tracer. a) Liquid slugs flowing downstream of the reaction channel after the pulse injection of tracer in a) the hydrophilic (wetting) reactor at J_L = 2.2 mm/s, J_G = 5.5 mm/s and b) the hydrophobic (partially-wetting) reactor at J_L = 2.2 mm/s, J_G = 4.2 mm/s. It is notable that the liquid slugs carrying the tracer are brighter in the hydrophobic reactor which suggests that the liquid slugs maintain the initial tracer concentration due to the absence of axial dispersion to the other slugs

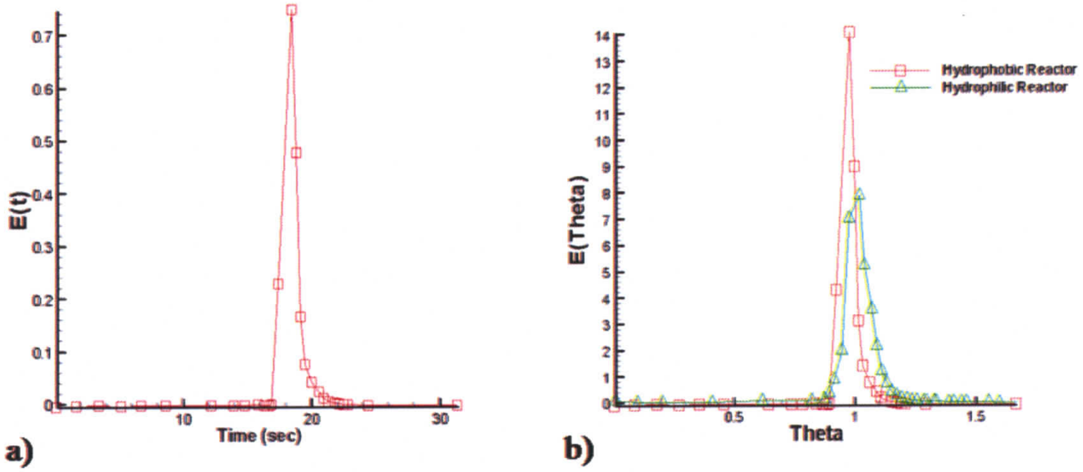

Figure 2.13 RTD profiles for the L = 150 mm microreactor. a) RTD function for the hybrid reactor at L = 150 mm downstream of the injection point with mean residence time; τ_m=18.4 s b) Normalized RTD for hydrophilic and hydrophobic microreactors at L=150 mm downstream of the injection point. The hydrophilic microreactor has a mean residence time; τ_m=16.9 s.

2.4. Summary

In this chapter, a hybrid microfluidic microreactor was developed, fabricated and tested using residence time distribution as the performance measure. RTD was measured for single-phase and segmented flow microreactors. In the segmented flow microreactors, surface modification was shown to reduce the common lubricating film in the classic Taylor flow (microchannel with wetting surface) and hence to inhibit the axial dispersion within the reactor. RTD measurement experiments were performed for microreactors with reaction channel lengths of 150mm, 300mm. Surface modification of the 300mm reactor caused a 63% narrowing in RTD within the modified reactor compared to the hydrophilic counterpart. For the 150 mm reactor, surface modification narrowed the RTD

40% compared to the hydrophilic reactor. These results confirmed that the film elimination narrows the RTD and improves the reactor performance. It was shown that surface modification is more efficient in longer channel lengths where axial dispersion and RTD broadening more significant. Such longer channel lengths are common in microfluidic reactor applications such as particle synthesis, self-assembly and other processes that require both rapid mixing and longer residence times (order of minutes).

3. Chapter 3: MODELING SHEAR FORCES IN SEGMENTED FLOW MICROREACTORS

3.1 Introduction

In this chapter a simplified numerical model is developed to study the hydrodynamics of the liquid flow within a gas- liquid segmented flow reactor. This chapter focuses on traditional segmented flow microreactors with a continuous wetting phase (i.e. not the hybrid microfluidic reactor developed in Chapter 2). The motivation of this numerical work is to find an order of magnitude estimate of the maximum shear stress within the gas-liquid segmented flow microreactor. The motivation of this study was an experimental observation that the growth of particles within the liquid slugs was being limited by flow-related forces. Specifically, given a chemical and thermodynamic environment in which particle growth is promoted, particles were found to decrease in size as opposed to increase in size when given a long channel (longer time) in which to grow (with all other factors remaining similar). This result suggested that in addition to reducing RTD, and improving mixing properties, segmented flow microreactors could enable tuning of size distributions of nanoparticles through flow forces. The experimental work was performed by Greg Schabas (alumnus of the UVic Microfluidics lab) and Joe Wang (current Ph.D. student co-supervised with Dr. Sinton and Dr. Moffitt, UVic Chemistry). Much previous work on this and related polymer particle systems has been reported elsewhere [Schabas (2007), Schabas et al. (2008a), Schabas et al. (2008b)]. The focus in this work is the study of the fluid mechanics inside the plug, particularly with an aim to quantify shear forces in these reactors.

A number of simplifications were made to allow solution of the complicated gas-liquid segmented flow in a simple but effective manner. Only the liquid phase flow was solved and flow within the gas phase was neglected due to its negligible viscosity and density compared to the liquid phase [Kreutzer (2003); Kreutzer et al. (2003)]. Gas-liquid interfaces were assumed to be fixed boundaries that provided zero shear, or in other words, negligible resistance to liquid flow at the gas-liquid interface was assumed. The assumption of the bubble surface as a fixed boundary is well supported by the fact that the reactor operates in very low capillary number regime (Ca~6.6e-05). For low Re number flows with low capillary numbers Bretherton relationship for the viscous pressure drop over a bubble can be employed [Bretherton (1961)] to justify "the fixed bubble shape" assumption quantitatively. In the flow regime studied in this numerical work Bretherton relationship suggests that $\Delta P_{Vis} = 0.006 \Delta P_{Cap} = 5.2 Pa$. Here ΔP_{Vis} is the viscous pressure drop over a bubble and ΔP_{Cap} is the surface tension cap pressure. This stark difference between viscous and surface tension effects explains why the viscous pressure drop in this flow regime is incapable of deforming the gas-liquid interface and leaves the bubble surface as a fixed boundary. Thus, the original two phase flow problem was approximated with single phase flow of the liquid in a domain bounded by a solid wall and fixed gas-liquid interfaces.

It is also noteworthy that in the wetting reactor experiments in Chapter 2, the bubble caps did not deviate from their apparent spherical shape under any flow conditions. The wetting microreactors used in chapter 2 also operate at a low capillary number regime (~1e-04) where the gas bubbles are symmetric and deformation in the bubble shape is negligible.

In the following sections, first, the geometry of the solution domain and the computational grid are presented and appropriate boundary conditions are attributed to the boundaries. The Navier-Stokes equations are then solved over the domain using a commercial CFD package. The numerical results are then employed to determine the maximum shear rate experience in the segmented flow. Next, the feasibility of the particle breakup is investigated and some explanations are proposed for the shear-induced processing of the quantum dot nanoparticles observed experimentally.

3.2 Numerical Modeling

3.2.1 Computation Domain and Boundary Conditions

The solution domain was a segmented flow unit cell which consisted of two half-bubbles and a liquid slug in the middle as is shown in Figure 3.1. Bubble and slug lengths were measured from the available experimental images. Figure 3.2 depicts the segmented flow pattern within the reactor employed in the quantum dot compound micelle self assembly experiment. The bubble and slug lengths were measured to be approximately equal at 1mm on average. The original reaction channel where the QD assembly was performed was 200μm wide and 150μm high. In the simulations, the original rectangular cross-section microchannel was approximated by a round microchannel with 86μm radius, equal to the hydraulic radius of the reaction channel. This simplification enabled the otherwise three-dimensional flow problem to be studied using a two-dimensional axisymmetric domain which is much more computationally economic. As mentioned earlier, change in the gas-liquid interface shape at the front and rear of the bubble was neglected due to very low capillary number of the flow regime studied [Bretherton (1961)], as also supported by experimental observations.

The bubble was assumed to be a wall boundary condition with assigned zero shear stress, which is a common boundary condition in modeling two phase flows of this type [Kreutzer et al. (2003); Kreutzer et al. (2003)]. It is noteworthy that from the perspective of shear stresses, this is also the conservative approach. An important simplification in these flows is to move the frame of reference at the bubble velocity. This change of reference frame enables the problem to be treated as steady-state with fixed boundaries, however it does require the wall velocity be set to reflect this change in reference frame, as shown in Figure 3.1. The periodic boundary condition was adopted at the two ends of the unit cell to account for a train of bubbles and slugs and to ensure fully developed flow within the microchannel. The center line of the capillary was set as an axis boundary condition (zero flux). A no-slip boundary condition was applied at the microchannel wall. The Geometry and boundary conditions as well as the grid were created in the software GAMBIT. A fine triangular grid was generated to allow discretization of the domain with a uniform high quality grid. Although quad, rectangular grids have better convergence properties, the rather extreme geometry to be modelled here required the flexibility afforded by the triangular elements. Specifically, the dimensions of the liquid domain vary from 86μm across the liquid slug to 0.1μm across the thin film. For this geometry a high quality quad mesh could not be generated. The quad mesh generated had high aspect ratio and skewness which are not desirable for a successful solution.

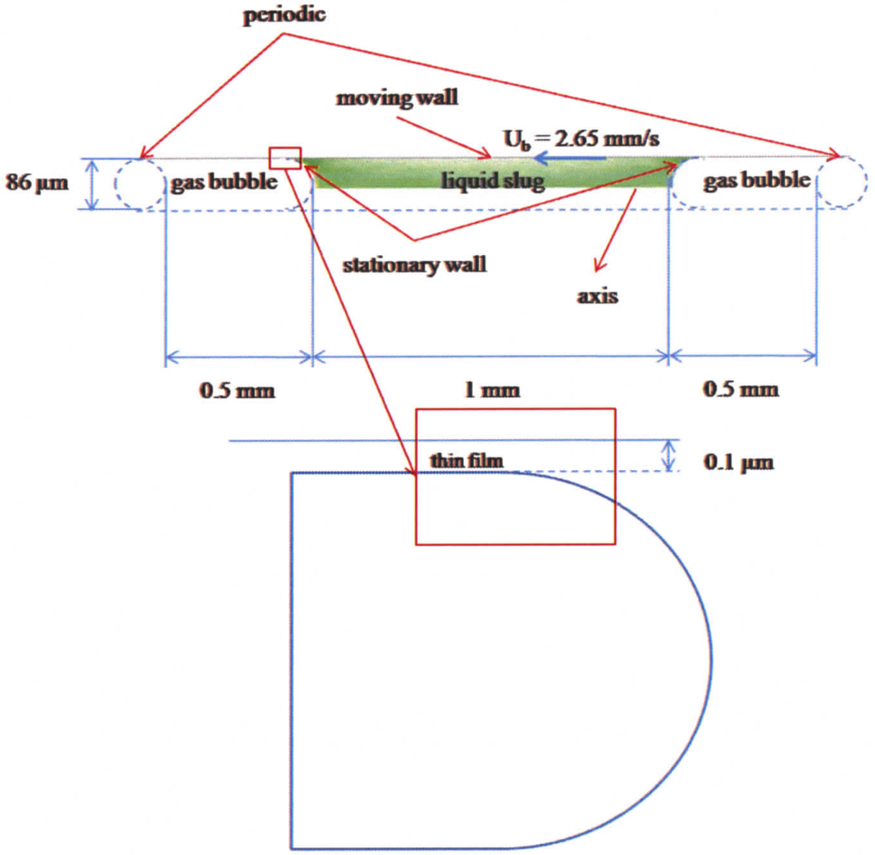

Figure 3.1 Schematic illustrating the computational solution domain and boundary conditions. The dashed lines are not included in the domain. The gas-liquid interfaces were assumed to be stationary walls and the computational reference frame moved at the bubble velocity. Thus, relative to the domain the bubbles are fixed and the wall moves in the upstream direction.

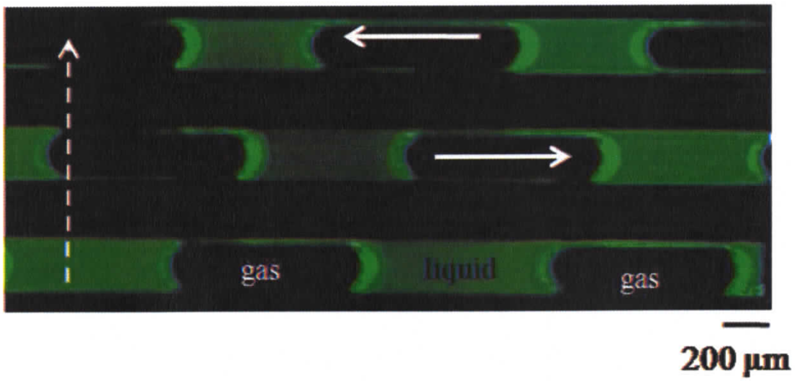

Figure 3.2 Fluorescence microscopy image of the flow pattern in the segmented flow microreactor used for nanoparticles assembly [Schabas (2007)]. The fluorescence observed it that of the polymer-stabilized quantum dot constituent particles. The bubbles and liquid slugs are symmetric with spherical bubble caps.

3.2.2 Solution

The 2D axisymmetric problem was solved in FLUENT 6.3. A steady state, segregated implicit solver was employed. Pressure was initially solved using a first order upwind scheme. Later, when the solution started converging the scheme was switched to second order upwind for more accurate results. The problem was solved employing a triangular mesh which allowed effective discretizing of the complex geometry without generating elements with high aspect ratio or skewness. Following the initial solution, the grid was adaptively refined at the regions with high gradients of flow parameters to reduce the high gradients within the solution domain and obtain a more accurate solution. Strain rate, or equivalently shear rate, (with units 1/s) is the primary variable used to characterize shear-induced particle breakup, and thus it was adopted as the refinement parameter in the computations. Three refinement steps were required before the solution showed independence of the grid size. Figure 3.3a shows the original grid near the bubble cap where the highest gradients are expected to occur. The refined grids are shown in

Figure 3.3b,c,d. The contrast in grids shown in Figure 3.3 points out the region requiring the maximum refinement, and corresponding to the highest strain rate gradients. The plot of shear rate versus grid size is shown in Figure 3.4. It is observed from the plot that the value of maximum strain rate in the domain remains constant after the second refinement of the grid to 110614 cells.

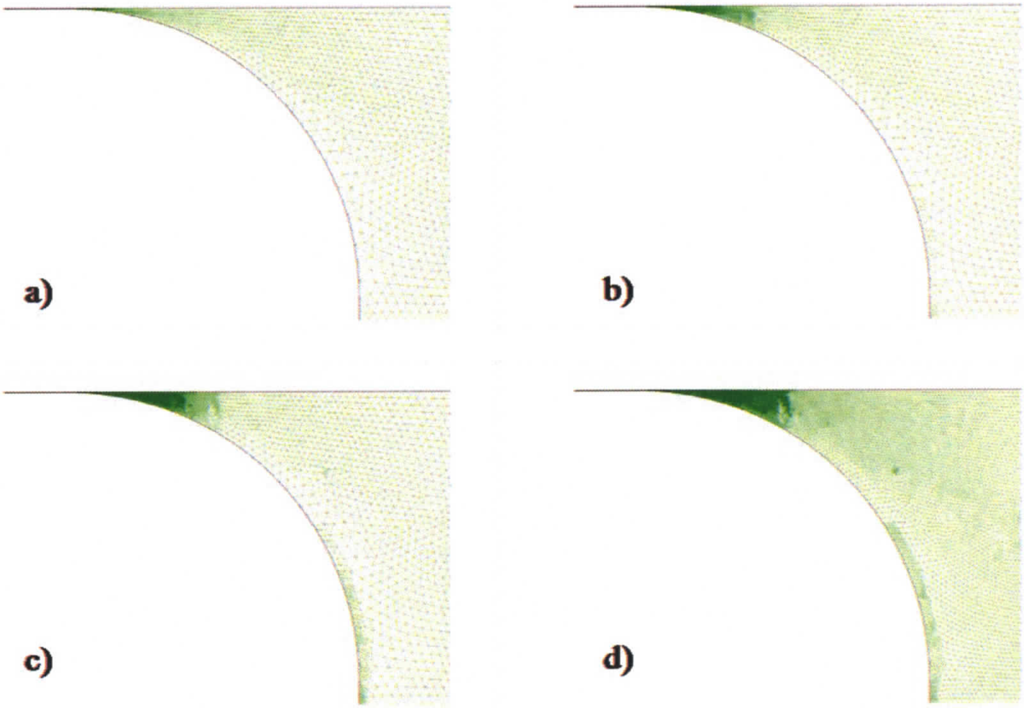

Figure 3.3 Plot of the triangular computational grid near the bubble cap for different generated meshes. a) The original grid with 40078 cells b) The grid adaptively refined to 44395 cells at regions with high shear rate gradients c) The grid adaptively refined to 110614 cells at regions with high shear rate gradients d) The grid adaptively refined to 374362 cells at regions with high shear rate gradients.

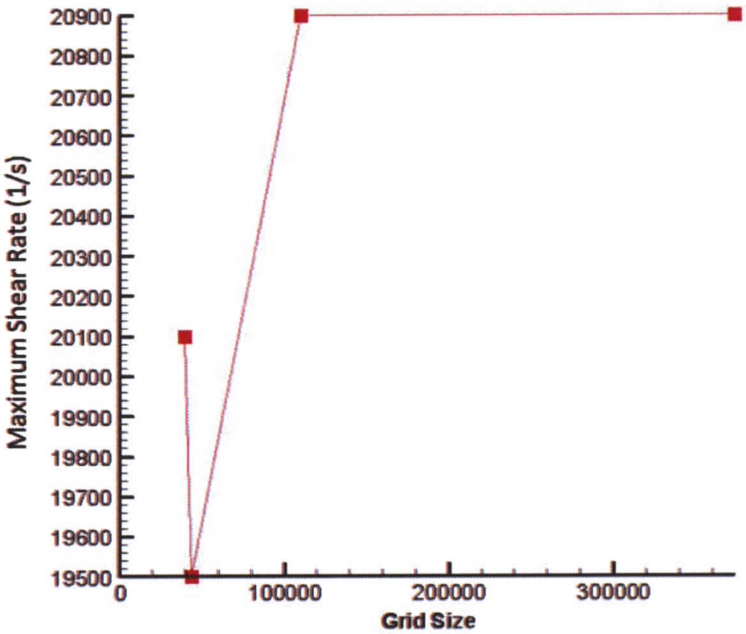

Figure 3.4 Maximum shear rate in the domain plotted versus the grid size for four different grid sizes. The equal value for the two largest grid sizes indicates that the solution, at these grid densities, is independent of the grid and thus may be applied for quantitative prediction of shear rate.

3.3 Results and discussions

3.3.1 Validation of the numerical results

Figures 3.5 shows the axial velocity distribution across the channel radius obtained from the computational model and compared to that obtained from the analytical solution for laminar flow in a circular cross-section channel. The numerical data are in a good agreement with the analytical solution. Here, the analytical solution is based on the assumption of fully developed flow within the liquid slug and is applicable in the flow at some middle point away from the bubble caps, provided the liquid plug is longer than a few diameters [Thulasidas et al. (1997)]. The parabolic analytical solution in a reference frame attached to the bubble is given in Eq. (3.1)

$$W(r) = \frac{2U_b}{\psi}\left(1 - \left(\frac{r}{R}\right)^2\right) - U_b \tag{3.1}$$

Where U_b is the bubble velocity, r is the radial distance from the axis, R is the channel radius, and ψ is defined as the ratio of the bubble velocity to the average velocity in the liquid slug [Thulasidas et al. (1997)]. Eq. (3.2) gives the relationship for ψ.

$$\psi = \frac{U_b}{V_{slug}} \tag{3.2}$$

Where V_{slug} is the average velocity inside the liquid slug. It has been shown that ψ is only a function of Capillary number for both round and square microchannels [Thulasidas et al. (1995); Thulasidas et al. (1997)]. For very low capillary numbers (<1e-04) ψ approaches unity and thus the bubble velocity and average liquid velocity become equal [Thulasidas et al. (1995); Thulasidas et al. (1997)]. Figure 3.6 compares the numerical data for shear rate distribution across the channel radius with the distribution obtained from the velocity profile in Eq. (3.1). The good agreement between the numerical and analytical solutions indicates the validity of the developed numerical model.

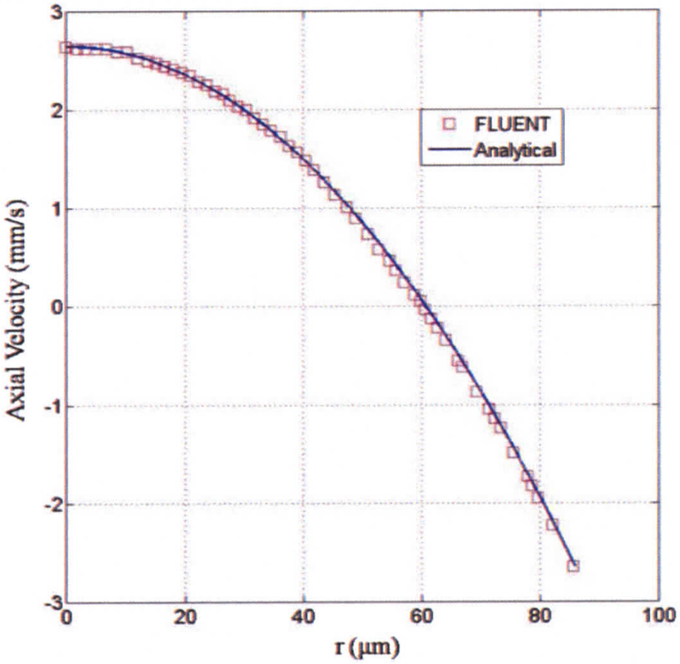

Figure 3.5 Axial velocity distributions across the channel radius at the middle of the liquid slug. The distribution obtained from FLUENT agrees well with the analytical distribution.

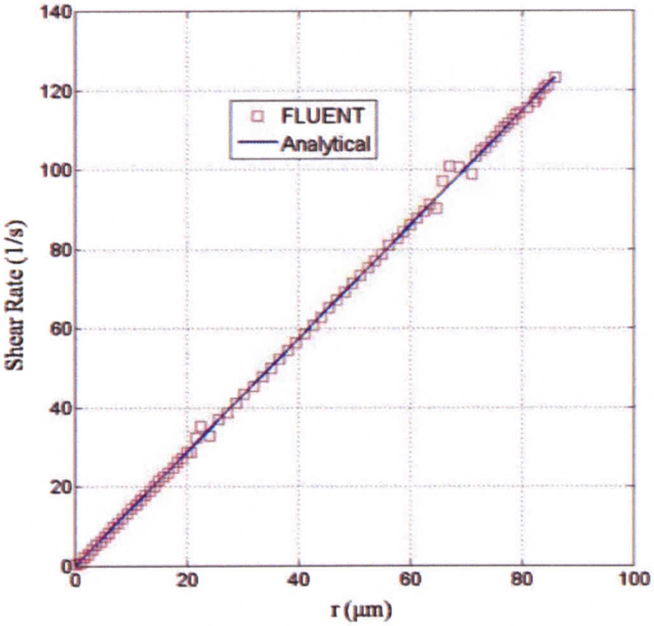

Figure 3.6 Axial shear rate distribution across the channel radius at the middle of the liquid slug. The data from the computational model agrees well with the analytical values.

3.3.2 Shear-Induced Particle Breakup

Figure 3.7a presents the computationally predicted shear rate contours within the liquid flow field. The contours show very low shear rates in the majority of flow field except for a transition region between the flat thin film and the circulating bulk flow. The shear rate distribution along the channel wall is shown in Figure 3.7b. The distribution shows two peak values representing the high-shear zone. Towards the bulk flow from the peaks, the distribution takes a downward slope to a significantly lower value within the bulk slug. While this finite shear is not obvious from the plot (due to the large scale required for the high shear rate points), it is in agreement with the analytical model for standard laminar flow in channels of circular cross-section. It is noteworthy that it is this, relatively negligible, degree of shear that would be experienced in a single phase reactor. The simulation results provided here demonstrate that the addition of a gas phase results in local regions with extremely high shear rates as compared to the case without a gas phase.

When considering if small particles within the liquid plug could be broken up via shear forces, it is useful to consider classical theory relating to 'droplet' breakup in shear flows. In order to avoid confusing interfacial phenomena at the scale of the particles of interest, with interfacial phenomena on the scale of the liquid plugs and gas bubbles, the term 'particle' will be used here instead of 'droplet' which is the more commonly used term in the literature. Thus it must be remembered here that the 'particles' of interest are not solid. Rather the particles are soft, and can be considered physically as fluid droplets with high internal viscosity. In the context of the classical particle breakup problem, shear-induced break up of particles within an external flow field depends on a number of parameters such as: the ratio of the particle viscosity to that of the external-flow (λ); the capillary number; the flow history; the initial shape of the particle; and finally the type of the external flow which may be classified by the ratio of the vorticity to the shear rate within the external flow [Rallison (1984)].

When considering shear-related particle breakup a slightly modified capillary number is employed (as compared to that presented in Chapter 1). Here the capillary number which is a measure of relative dominance of viscous and surface tension forces is defined as

$$Ca = \frac{\mu G a}{\Gamma} \tag{3.3}$$

where μ is the external flow viscosity, G represents the shear rate and a is the characteristic dimension of the droplet and Γ is the surface tension at the interface between the particle and the external liquid phase. In the context of particle breakup, critical capillary numbers (Ca_c) have been proposed to predict the breakup of particles, meaning that a particle will break apart if the capillary number grows larger than the critical value [Rallison (1984); Stone (1995); Schabas et al. (2008b)]. The critical capillary number curves which are available in the literature from experimentation and/or computation [Rallison (1984); Stone (1994)] are functions of viscosity ratio, λ, and the velocity gradient tensor parameter, α, which is given in Eq. (3.4)

$$\frac{Vorticity}{Shear\ rate} = \frac{1-\alpha}{1+\alpha} \tag{3.4}$$

Where the limits α=0 and α=1 correspond to a simple shear flow and an irrotational flow respectively [Rallison (1984); Stone (1994)].

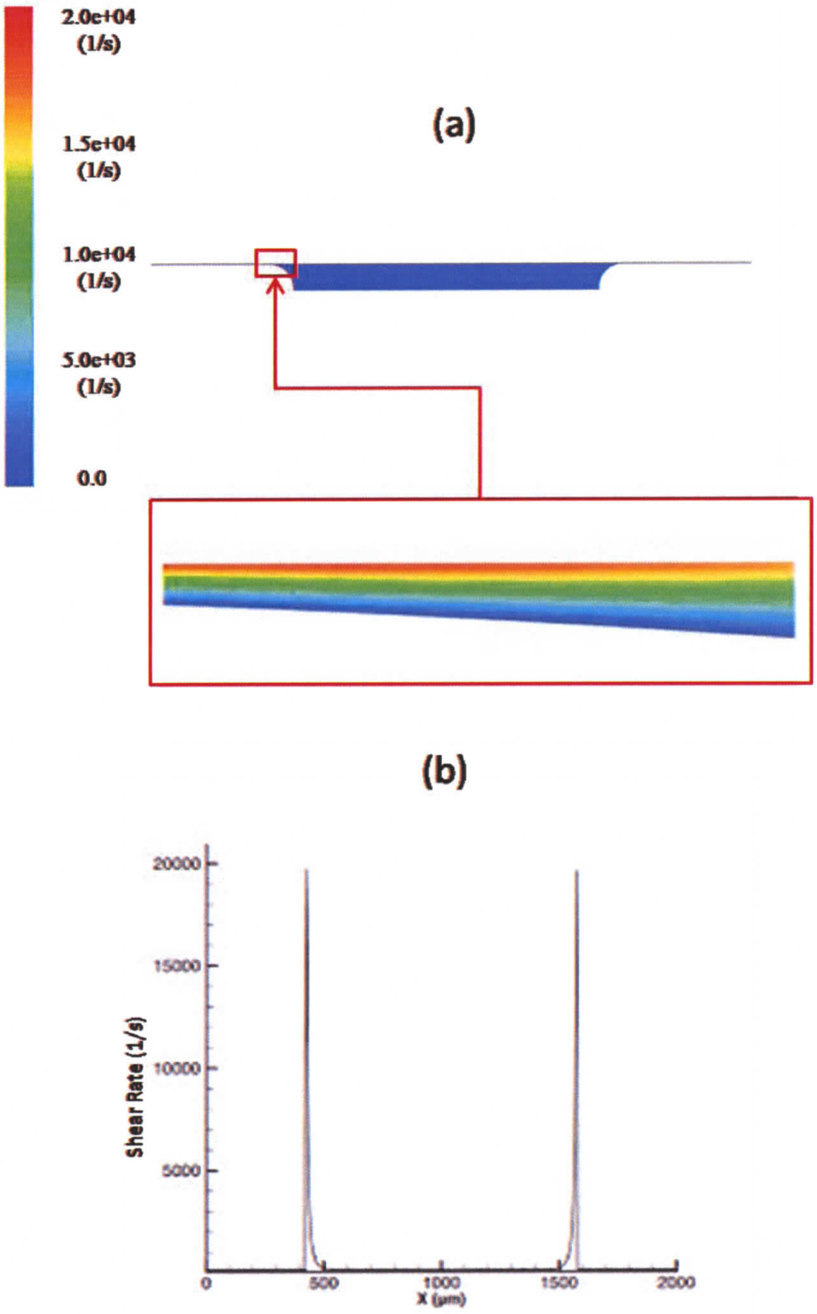

Figure 3.7 Computationally predicted shear rates in the gas-liquid segmented flows. a) Shear rate contours in the solution domain. The bulk flow within slug has much lower shear rate compared to the values at the magnified region, the transition zone between the bulk flow and the thin liquid film. b) Axial shear rate distribution along the channel wall. The high peaks mark the transition region between the bulk flow and the thin film.

To obtain the critical capillary number required for break-up, the flow parameter, α, is calculated from the vorticity and shear rate data given by the numerical model. The calculations indicate an approximate value of 0.1 for α in the regions of high shear stress. The streamline patterns for this value of α are shown in Figure 3.8. The velocity vector field at the high shear region given in Figure 3.9 confirms the flow pattern proposed by the parameter α. As is shown in Figure 3.9, a narrow trail of the bulk circulating flow slows down towards the bubble cap where it eventually arrives at a stagnation point on the bubble surface. A narrow portion of the flow near to the wall bypasses the stagnation point towards the thin film. The bypass and circulating flow as well as the stagnation point on the bubble surface are also indicated in the streamline pattern given in Figure 3.8. The streamline patterns and the location of the stagnation point are also in agreement with those proposed by Taylor [Taylor (1961)]. To find the value for critical capillary number the viscosity ratio of the droplet, λ, must also be known. For the quantum dot nanoparticles in the experimental conditions of Schabas et al. (2008b), the droplets viscosity ratio is extremely high, $\lambda >> 10$.

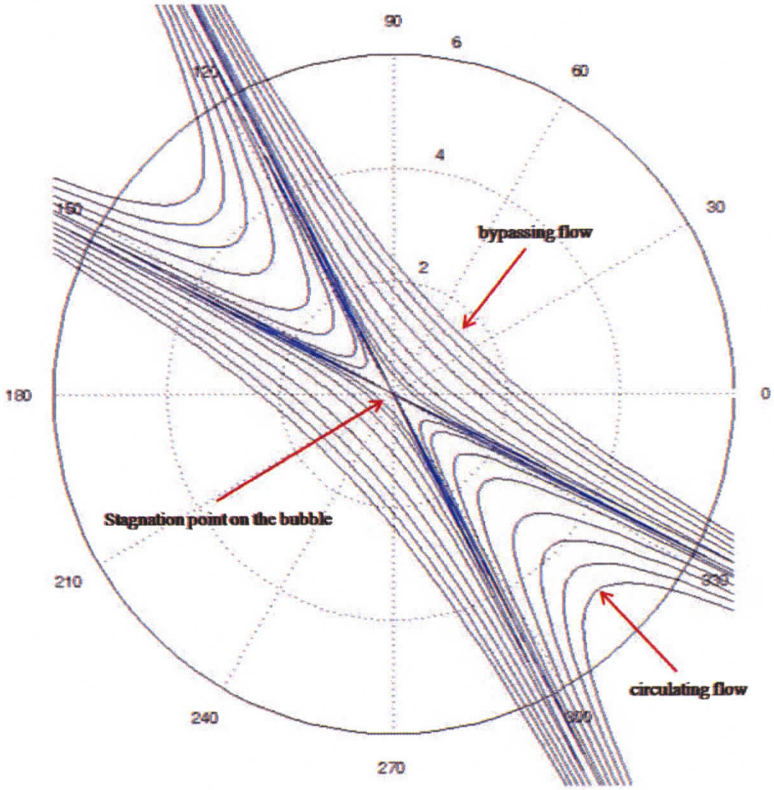

Figure 3.8 The streamline patterns plotted for the velocity gradient tensor parameter α = 0.1. The flow parameters of α = 0 and α = 1 correspond to simple shear and irrotational flow, respectively. Value of α for other types of flows fall between 0 and 1.

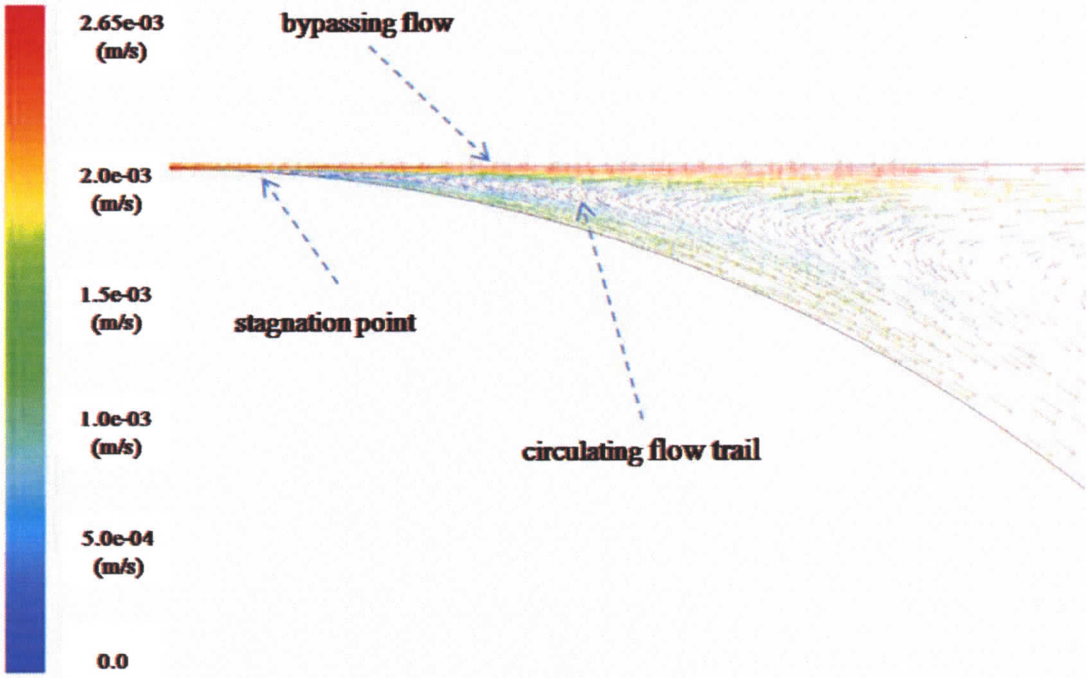

Figure 3.9 Velocity vectors at the transition region where circulating and bypass flows are present. The trail of the circulating flow shown in blue coincides with the bubble surface where it forms a stagnation point. The bypassing flow passes over the stagnation point and becomes the liquid film surrounding the bubble.

For the case of fully extensional flow fields (i.e. zero vorticity, $\alpha = 1$) and fields of relatively low vorticity, the critical capillary number in case of steady flow is found from the available data [Rallison (1984); Stone (1994)] to be approximately 0.1 for very large viscosity ratios ($\lambda >> 10$). The critical shear rate, G, is then found by substituting the Ca_c value obtained above, in Eq. (3.3) along with other parameters [Schabas et al. (2008b)]; the flow viscosity ($\mu = 0.92 \times 10^{-02}$), the droplet diameter ($a = 100nm$) and estimated particle/external flow surface tension ($\Gamma = 2$ dyn/cm). The critical shear rate required for the breakup, G_c, is calculated to be $4 \times 10^{06} s^{-1}$ [Schabas (2008)] In the high-viscosity particle case, this critical shear rate will increase sharply toward infinity as the flow vorticity increases to the limit of simple shear flow (i.e. $\alpha = 0$). A comparison of the estimated value of G_c with the maximum shear rate in the flow field, $\sim 2.0 \times 10^{04}$, given in Figure 3.7 indicates that the particle breakup in this flow regime and under steady state shear conditions is unlikely to occur.

Although the above approximate calculations provide a point of reference. It is important to note that several additional features of the experimental system, not included in either the model or the classical theory, may affect the particle break up significantly. These additional features may account for the QD breakup at a considerably lower shear rate within the microreactor [Schabas et al. (2008)]. For instance, the above analyses assume a steady shear exerted on the particles while in reality the unsteady circulating flow in the segmented flow reactor exposes the particles to abrupt shear rate gradients shown in the shear rate contours of Figure 3.7. It has been widely reported that the particle breakup is highly dependent on the instantaneous shear history and can occur due to abrupt shear gradients even at subcritical values of shear [Stone (1994); Schabas et al. (2008)]. It is also notable that for the measurement of the external flow/QD surface tension, Γ, the effects of the surfactants present at the particle surface were neglected. These surfactants can promote particle breakup by reducing the restraining surface tension forces compared to the shear forces and cause particle breakup at lower shear rates [Schabas et al. (2008)]. Dynamic surfactant gradients on the particle surface might also induce breakup at lower shear rates compared to a clean particle [Stone (1994); Schabas et al. (2008)].

3.4 Summary

A simplified numerical solution for gas liquid segmented flow within a round capillary was developed to obtain an approximate shear rate distribution in the flow field. The velocity profile and shear rate distribution across the channel diameter, given by the numerical model, were then validated against an analytical solution for velocity distribution in liquid slugs far away from the bubble caps. The numerical model and the analytical solution showed good agreement in the central portion of the liquid plug. The numerical data were then employed to find the value of maximum shear rate inside the liquid segments and compare those results to classical data regarding the critical capillary number for the breakup of particles. It was found that the addition of the gas phase results in local regions with extremely high shear rates as compared to the case without a gas phase. These results point to potential for exploiting shear-related phenomena in gas-liquid segmented reactors in addition to established benefits associated with rapid mixing and narrowed residence time distributions.

In the QDCM particle assembly application, the maximum shear rate predicted by the numerical model, while very high as compared to the single-phase case, was less than the value required for particle break-up as predicted by classical theory. Both the classical theory and the computational model, however, have many simplifying assumptions that should be considered. Specifically aspects of the interfacial phenomena and fluid flow in the segmented flow reactor that are not captured by the computational model or classical theory were discussed including unsteady flow effects, surfactant effects, and three-dimensional flow effects. It was argued that unsteady cyclic exposure of the particles to abrupt shear gradients and also presence of surfactants at the interface during the particle formation and processing could promote breakup at subcritical shear values.

While it is not possible, from the simulations alone, to conclude that the mechanism for particle break-up in these reactors was shear dominated, it is possible to conclude that shear forces in these reactors are much higher than single phase reactors and that they approach the regime where breakup of sub-micron particles or droplets is achievable.

4. Chapter 4: FABRICATION OF MICROCHIPS WITH LARGE SURFACE AREA

4.1 Introduction

Fabricating masters with features covering a large surface area is challenging due to the presence of imperfections on the surface of the spin-coated photoresist layer on the substrate. In other microfluidic applications, such as many analytical or diagnostic devices, much lower channel lengths are required (typically on the order of a few centimetres). Lower channel lengths result in more sparse and localized microchannel patterns to be fabricated. The photomasks of such patterns can be manipulated as to avoid any defects on the photoresist-coated wafer. Micro size gas bubbles, dust, and beading of unbaked photoresist on the substrate surface are the major sources of imperfections on the coated substrate. While such defects may be avoided when fabricating small/sparse channels, large-area structures require a higher degree of coating quality.

In this chapter the detailed step by step microfabrication process for fabricating microchips with large surface area is presented. At the end a number of fabricated masters and microchips with large surface area are depicted which were required for this work, and were the first of their surface area and complexity which have been fabricated in UVIC Microfluidics lab.

4.2 Methodology

4.2.1. Rapid Prototyping

An introduction to rapid prototyping and replica molding was given in Chapter 1. Here, the detailed process for rapid prototyping and molding of microchips with complex and large features is presented.

4.2.1.1 Substrate Pre-treatment

Surface pre-treatment was performed for two main objectives: 1) to increase the surface energy of the substrate and thus prevent beading of spin-coated photoresist layer on the surface and 2) to clean the surface and thus remove contaminants. The substrate was first exposed to piranha solution (three parts H_2SO_4 & one part H_2O_2) for 15-30 minutes. The etched substrate was then rinsed thoroughly in distilled water. To dehydrate the surface, the substrate was baked at 200°C for 15 minutes on a hotplate.

In some cases where the piranha etching failed to deliver strong enough adhesion of photoresist onto the substrate, oxygen plasma treatment of the substrate surface was employed to increase the surface energy. Oxygen plasma treatment of the substrate was found to enhance adhesion of the photoresist layer to the substrate. It is notable that plasma treatment was employed only to improve adhesion properties of already nominally clean surfaces.

4.2.1.2 Photoresist Coating

SU-8 photoresists (Microchem, Newton, MA) are designed to produce low defect coatings over a very broad range of film thickness (sub-micron to 300μm) depending on the type of photoresist. Throughout this thesis SU-8-50 and SU-8-100 were used which are suitable for thicknesses for features from 10μm to over 250μm [Microchem SU-8 50-100 datasheet]. Spin rate-thickness curves available from the photoresist producer were used to find the proper spin rate for achieving the photoresist thickness of interest on the substrate.

The coating process was performed in the following steps which are recommended by the photoresist producer [Microchem SU-8 50-100 datasheet]:

1. Static dispense: Approximately 1ml of SU-8 per inch of substrate diameter was dispensed on the substrate by pouring it from a small bottle. Care was taken to generate the minimum number of microsize bubbles which can stick to the substrate surface and produce defects on the surface. This was done by dispensing the photoresist slowly and very close to the substrate surface. In cases where high numbers of bubbles were present within the dispensed photoresist, the substrate was exposed to vacuum inside a vacuum and the bubbles were removed.

2. Spread Cycle: the programmable spin-coater (G3P-8 SPINCOAT, SCS, IN) was programmed to ramp up to 500 rpm at 100 rpm/second acceleration. The rpm was held at this speed for 5-10 seconds to allow the photoresist to cover the entire surface.

3. Spin Cycle: The spin-coater was programmed to increase the spin rate from 500 rpm to the final spin rate at an acceleration of 300 rpm/second and was held at the final speed for 30 seconds.

4. The spin rate was then ramped down to zero and the coated substrate was removed from the spin coater.

4.2.1.3 Soft Bake

After the photoresist had been applied to the substrate, it was soft baked to evaporate the solvent and solidify the film. The soft bake was performed in two steps. First, at 65C and then at 95C. The baking duration depends on the thickness of photoresist layer. Recommended baking times are provided by the photoresist producer [Microchem SU-8 50-100 datasheet]. However it was observed that a longer baking time than the recommended time is usually required for the solvent to evaporate completely. Longer baking durations are especially required when the photoresist layer is thicker than 100μm. A soft baking step can take up to several hours therefore the substrate was covered to protect it from dust and also from absorbing ambient UV light.

4.2.1.4 Exposure to UV Light

The optimal exposure dose depends on film thickness (thicker films require higher dosage). Care was taken to expose the photoresist layer to enough UV light such that the entire photoresist layer was activated right up to the wafer surface. Underexposing photoresist can cause poor adhesion, negative channel sidewalls and excessive cracking of photoresist. The substrate was set on the UV light source platform with a photomask laid on top of it. It was then exposed to UV light for 90-95 seconds which was enough UV exposure for the range of photoresist thicknesses employed in this work.

4.2.1.5 Post Exposure Bake

Following the exposure, a post exposure bake was performed to cross-link the exposed portions of the film. It is important to bake the photoresist for a long enough period of time to let the exposed photoresist polymerize completely. The post exposure baking time also depends on the thickness of photoresist layer. Similar to the soft bake step, the post exposure baking was done in two steps. First, at 65C for one minute and then at 95C for a longer period of time which depended on the thickness of the photoresist (typically 15 minutes for 100 μm thicknesses). The wafer was then cooled down slowly to avoid cracking of the polymerized photoresist due to abrupt temperature changes.

4.2.1.6 Developing the Photoresist

To remove the unexposed parts of the photoresist layer, the substrate was developed in SU-8 developer liquid (Microchem, Newton, MA) for several minutes (6 - 20 min) depending on the thickness. After washing off the unexposed photoresist the substrate was rinsed with ethanol to stop the action of the SU-8-Developer.

Figure 4.1 depicts a number of masters with high surface coverage. These masters were all developed through the steps presented above.

4.2.2 Replica Molding and Final Packaging:

PDMS and the curing agent were mixed with a 10:1 ratio. The mix was degassed in a vacuum chamber (Model 280A, Fisher Scientific, ON,) and applied over the master contained within a Petri dish. The container was put in the vacuum chamber for a final degassing. The molded PDMS was then baked on a hotplate at 85C for 30 minutes. The PDMS chip was then removed from the master and the inlet and outlet holes were punched. The PDMS chip was then sealed by a glass slide coated with PDMS. The PDMS chip and PDMS-coated glass slide surfaces were exposed to oxygen plasma and were put together to form permanent bonds. Figure 4.2 shows a number of high-area-coverage microchips fabricated in PDMS for different applications. In particular the chip in Figure 4.2c exhibited a serpentine reaction channel with hydraulic diameter of 68 μm that stretched 460 cm and the chip area covered 1800 mm^2.

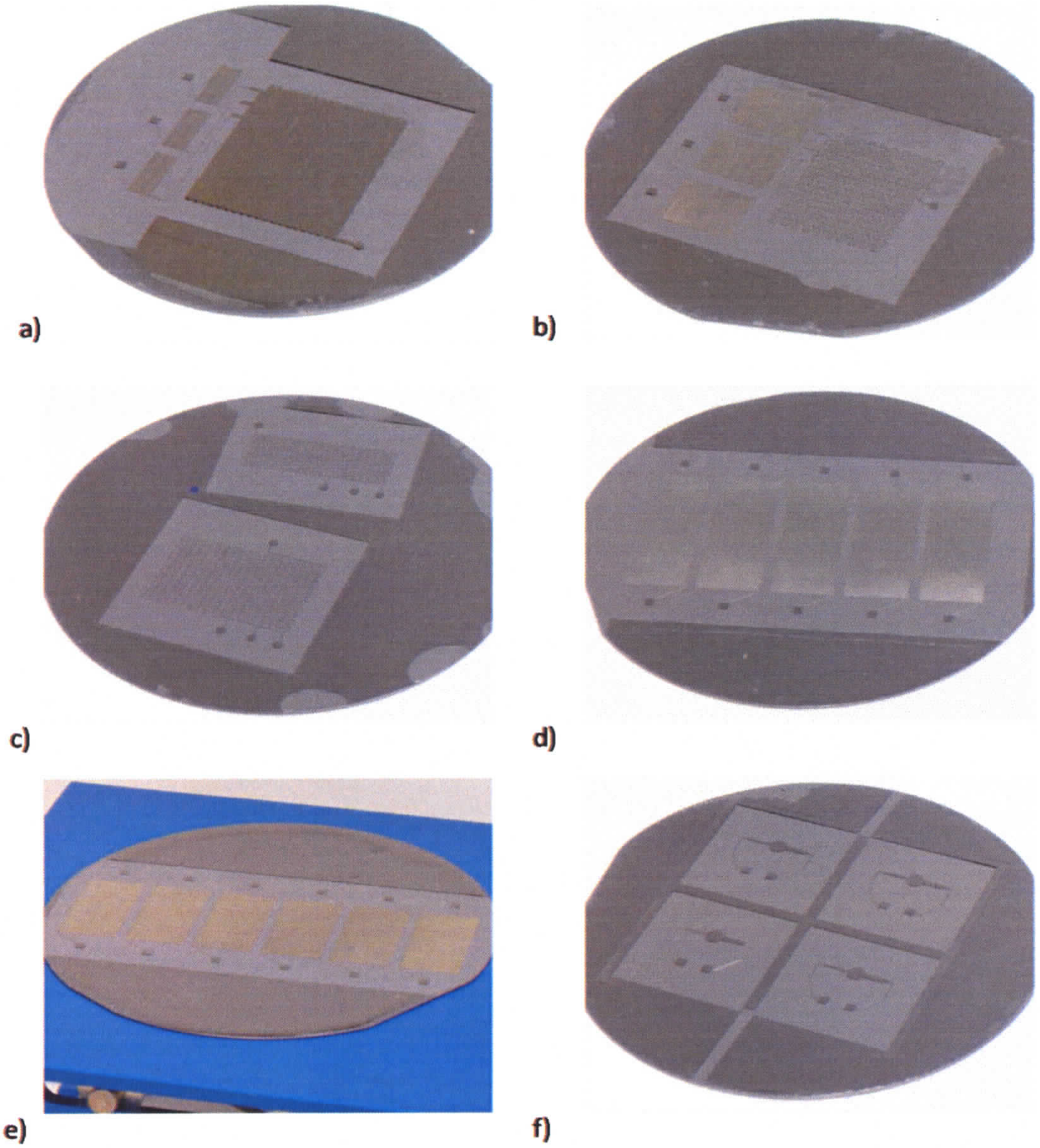

Figure 4.1 Images of microfluidic chip masters in photoresist-on-silicon. a) A microreactor with straight channels developed for RTD measurement experiments b) A microreactor with meandering channels amd onchip resistors developed for RTD measurement experiments. c) Microreactors with meandering channels developed for RTD measurement experiments d) An array of five long reaction channels designed and developed for Enzyme-Linked ImmunoSorbent Assay (ELISA) applications. e) An array of six long reaction channels developed for Enzyme-Linked Immuno-Sorbent Assay (ELISA) applications. f) Detection chips developed for Enzyme-Linked Immuno-Sorbent Assay (ELISA) applications.

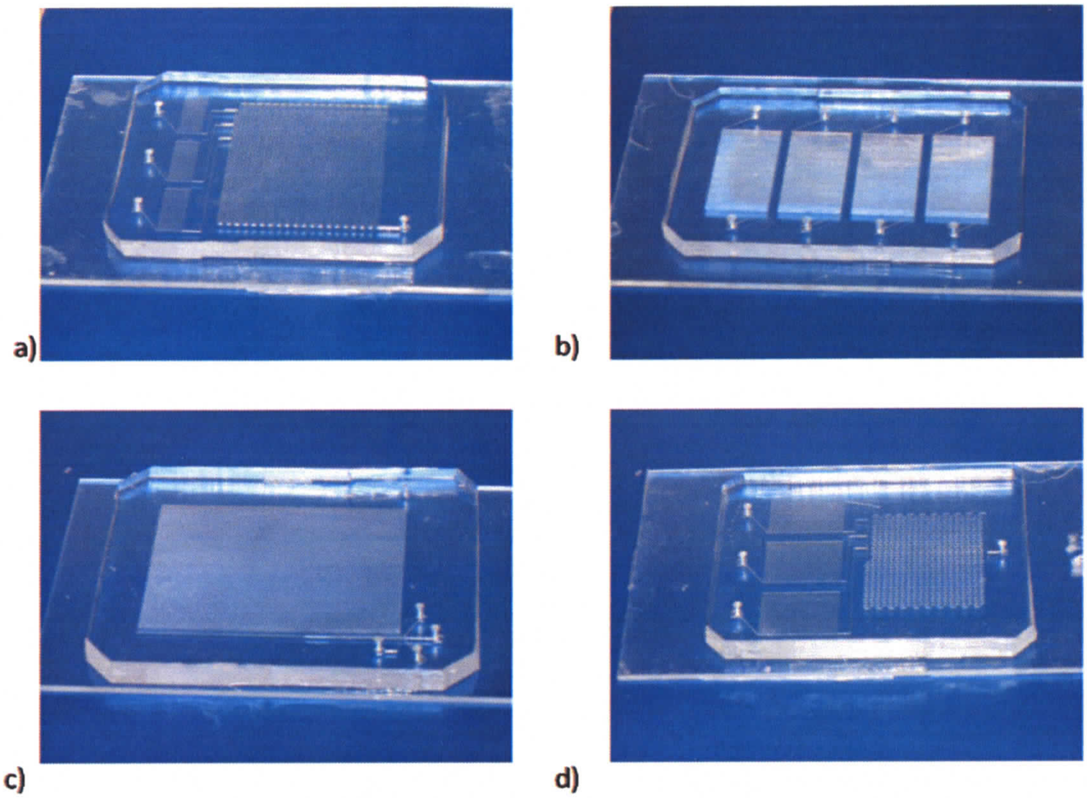

Figure 4.2 Images of large area coverage PDMS microfluidic chips on PDMS-coated glass microscope slides. a) A microreactor with straight channels and on-chip resistors fabricated in PDMS for RTD measurement experiments b) A chip containing an array of four long reaction channels developed for ELISA applications. It was also employed as a resistor block in two phase experiments. c) An ultra long microreactor fabricated in PDMS for size control of quantum dot compound nanoparticles. This chip had the highest coverage of those developed in this work. d) A microreactor with meandering reaction channel and on-chip resistors fabricated in PDMS for RTD measurement experiments.

4.3 Summary

Large area patterning of microchannels is require for microfluidic reactors where both rapid reactant mixing and long residence times are desired. Fabricating such large chips required the development of a detailed microfabrication process, and represents a contribution of this thesis. The step by step process developed for fabrication of masters with large surface area features was presented. A number of such high surface area masters fabricated onto silicon substrates as well as microchips casted in PDMS were presented.

5. Chapter 5: CONCLUSIONS AND FUTURE WORK

5.1 Contributions of This Thesis

This thesis was devoted to the study and application of gas-liquid segmented flow microfluidic reactors. Segmented flow microreactors were modelled, designed, fabricated, tested and applied in this work.

In the context of experimental work the contributions include the design and fabrication of microreactor and resistor chips which could operate steadily. A novel segmented flow reactor was developed which performed up to 63% better than the gas-liquid segmented flow microreactors which have been presented to date. In the context of numerical work, an effective computational model was developed for studying hydrodynamics of segmented flow in microreactors, and through that work it was found that regions of very high shear rate exist in these flows. The microchips fabricated and the experimental setups developed throughout this work are the most complicated microchips and setups which have been developed in UVic Microfluidics Lab to date. The major contributions of this thesis are summarized below.

5.1.1 Development of a Segmented Flow Microreactor with Hybrid Surface Properties

A gas-liquid segmented flow microreactor with wetting injector channel and partial-wetting reaction channel was developed. The wetting injection channel allowed stable segmentation of the liquid phase. The partial wetting reaction channels were modified so that the lubricating thin film surrounding the gas bubbles in the wetting injector channel was eliminated. The elimination of the thin film was due to the increase in surface tension between the liquid phase and the channel walls that was achieved with surface treatment. Residence time distribution (RTD) tests were performed to quantify the performance of the developed hybrid reactor and also the regular fully-wetting reactor. The hybrid microreactor showed up to 63% narrower RTD which is a significant gain in reactor performance. The RTD width is an indication of performance for microreactors in that a narrow RTD indicates minimal plug-to-plug contamination, and indicates that the reactants remain in the reactor for a similar period of time, under similar conditions. Similar reaction times and conditions promote homogeneity of product, in general.

5.1.2 Numerical Study of Shear-Induced Particle Breakup in a Segmented Flow Reactor

A simplified numerical model was developed to study the effect of shear stress on particle breakup in gas-liquid segmented flow microreactors. The complicated physics of two phase flow was simplified through justified assumptions. As a first assumption the rectangular reactor channel was approximated by a round axisymmetric channel with a diameter equal to the hydraulic diameter of the rectangular channel. Moreover, in the flow regime studied, the internal gas flow had negligible influence on the flow field within the liquid phase. Therefore, the gas phase was eliminated from the flow physics with the exception of the two-phase interface which was taken as a fixed boundary that could not support a shear force. The problem was modeled in a reference frame attached to the moving bubbles which was implemented by assuming zero velocity for the bubbles while assigning the bubble velocity to the channel wall. The moving reference frame enable the problem to be considered steady state. The numerical results were validated against an analytical solution at the liquid plug mid-plane. Where the bubble caps meet the thin liquid film a region of very high shear-rate was found. The shear rates in this region were 170 times those found in single phase flows as similar flow rates. The numerical results along with data available in literature on the droplet breakup were used to predict the feasibility of particle breakup within the microreactor, an effect observed experimentally by other group members. The model gave a maximum shear rate of $2.09 \times 10^{04}(1/s)$ in the flow field. This value is less than that predicted for these particles using classical theory, however, there is uncertainty in both Figures that were worthy of discussion, as in Chapter 3. While it is not possible, from the simulations alone, to conclude that the mechanism for particle break-up in these reactors was shear dominated, it is possible to conclude that shear forces in these reactors are much higher than single phase reactors and that they approach the regime where breakup of even nanoscale particles or droplets is achievable.

5.1.3 Fabrication of Microchips with High Surface Area

High surface area microchips with complicated features were developed throughout this thesis work and as collaboration with other researchers in UVic Microfluidics lab. Modifications were made to the typical microfabrication methods widely used in the area of microfluidics. These minor changes combined with the skills developed through mass production of microchips enabled the fabrication of effectively flawless high surface area masters. These masters had the largest and the most complicated features of all the masters developed in UVic Microfluidics Lab to the date.

5.2 Proposed Future Work

There are a number of possible extensions to this thesis work that can be considered for future work. Here the extensions and the significance of their possible deliverables are discussed.

5.2.1 Further Development of the Hybrid Reactor

Although the RTD tests for the hybrid reactor showed a considerable improvement in the performance over the established reactor with the same geometry, the reactor was operated for a limited range of reaction channel lengths and cross-sectional dimensions. If the segmentation of liquid plugs is as effective as the results of this work indicate, dispersion between plugs will not be a function of residence time or channel length. In that sense, a very long reactor channel would showcase the hybrid reactor more so than the results presented here. Also, using different cross-sectional geometries could clarify the range of applicability and the extent of performance improvement these reactors can offer.

The hybrid reactor developed in this work was suitable only for aqueous reactions due to the hydrophobic properties of the coating employed. On the other hand, gas-liquid segmented flow microreactors are widely employed for other applications which do not include aqueous solutions. Thus, it could result in promising findings to study the feasibility of methods which can render the microchannel surface partial-wetting or non-wetting in contact with other types of reactants such as organic solvents.

5.2.2 Further Investigation of the Shear-induced Particle Breakup in Segmented Flow Reactors

Microreactors with different geometry and operating conditions which can promote a wide range of shear stress could be employed for studying the effect of shear stress on particle breakup in a more comprehensive manner. Developing reliable methods for production of nanoparticles of arbitrary size and/or size distribution through shear processing within segmented flow reactors could be another venue for potential future work. Work along these lines is currently underway by Joe Wang, a Ph.D. student co-supervised by Dr. Sinton and Dr. Moffitt.

6. BIBLIOGRAPHY

Acheson,D.J., 1990, “Elementary Fluid Mechanics”, *Oxford University Press*, New York.

Adzima, B. J., and Velankar, S.S., 2006, ” Pressure drops for droplet flows in microfluidic channels”, *Journal of Micromechanics and Microengineering,* **16, pp.** 1504–1510.

Ahmed, B., Barrow, D., and Wirth, T., 2006, “Enhancement of Reaction Rates by Segmented Fluid Flow in Capillary Scale Reactors”, *Advanced Synthesis and Catalysis*, **348**, pp. 1043-1048

Ajaev, V.S., and Homsy, G.M., 2006, “Modeling Shapes and Dynamics of Confined Bubbles”, *Annual Review of Fluid Mechanics*, **38**, pp. 277-307.

Barajas, A.M., Panton, R.L., 1993, “The effect of contact angle on two-phase flow in capillary tubes. *International Journal of Multiphase Flow*, **19**, pp. 337-346.

Bazylak, A., Sinton, D., Djilali, N. (2005) "Improved Fuel Utilization in Microfluidic Fuel Cells: A Computational Study." *Journal of Power Sources*, **143**, pp. 57-66

Beebe, D.J., Mensing, G.A. and Walker, G.M., 2002, “Physics and Applications of Microfluidics in Biology”, *Annual Review of Biomedical Engineering*, **2**, pp. 261-286.

Berčič, G., Pintar, A., 1997, ” The role of gas bubbles and liquid slug lengths on mass transport in the Taylor flow through capillaries”, *Chemical Engineering Science,* **52 (21, 22)**, pp. 3709–3719.

Bird, R.B., Stewart, W.E. and Lightfoot, E.N., 1960, “Transport Phenomena”, John Wiley & Sons, New York.

Bretherton, F.P., 1961,”The motion of long bubbles in tubes”, *Journal of Fluid Mechanics,* **10**, pp. 166–188.

Bringer, M.R., Gerdts, C.J., Song, H., Tice, J.D. and Ismagilov, R.F., 2004, “Microfluidics Systerms for Chemical Kinetics That Rely on Chaotic Mixing in Droplets”, *Philosophical Transactions Royal Soiety London,* **362**, pp. 1087-1104.

Chen, D.L., Li, L., Reyes, S., Adamson, D.N., and Ismagilov, R.F., 2007, “Using Three-Phase Flow of Immiscible Liquids To Prevent Coalescence of Droplets in Microfluidic Channels: Criteria To Identify the Third Liquid and Validation with Protein Crystallization”, *Langmuir*, **23**, pp. 2255-2260.

Chin, C.D., Linderb, V., and Sia, S.K., 2007, “Lab-on-a-chip devices for global health: Past studies and future opportunities”, *Lab on a Chip*, **7**, pp. 41–57.

Choban, E.R., Markoski, L.J. Wieckowski, A., Kenis, P.J.A., 2004, “Microfluidic fuel cell based on laminar flow”, *Journal of Power Sources*, **128**, pp. 54–60.

Coleman, J.T., McKechnie, J. and Sinton D., 2006, “High-Efficiency Electrokinetic Micromixing Through Sequential Injection and Expansion”, *Lab on a Chip*, **6**, pp. 1033-1039.

Coleman, J.T. and Sinton, D., 2004, “Microfluidic Mixing Through Sequential Sample Injection With Rapid Expansion”, *International Mechanical Engineering Congress and RD&D Exposition*, Anaheim, CA, USA, Nov.13-19.

Cox, B.G., 1964, “An experimental investigation of the streamlines in viscous fluid expelled from a tube”, *Journal of Fluid Mechanics,* **20**, pp. 193–200.

Cubaud, T., Ho, C.-M., 2004, “Transport of bubbles in square microchannels”, *Physics of Fluids,* **16 (12)**, pp. 4575–4585.

Cubaud, T., Ulmanella, U. and Ho, C-M., 2006, “Two-Phase Flow in Microchannels with Surface Modifications”, *Fluid Dynamics Research*, **38**, pp. 772–786.

de Gennes, P. G., Brochard-Wyart, F., Quere, D., 2004, ”Capillarity and Wetting Phenomena: Drops, Bubbles, Pearls,WaVes”, Springer-Verlag, New York.

De Leebeeck, A., 2006, “Nanofluidic Species Transport and Nanostructure Based Detection On-Chip”, M.A.Sc. Thesis, *Department of Mechanical Engineering, University of Victoria.*

De Leebeeck, A., Sinton, D. 2006 "Ionic Dispersion in Nanofluidics." *Electrophoresis,* **27**, pp. 4999-5006.

deMello, A.J., 2006, “Control and Detection of Chemical Reactions in Microfluidic Systems”, *Nature*, **442**, pp. 394-402.

Diao, J., Young, L.,Kim, S., Fogarty, E.A., Heilman, S.M., Zhou, P., Shuler, M.L., Wu, M., and DeLisa, M.P., 2006, “A three-channel microfluidic device for generating static linear gradients and its application to the quantitative analysis of bacterial chemotaxis”, *Lab Chip*, **6**, pp. 381–388.

Doms, M., Feindt, H., Kuipers, W.J., Shewtanasoontorn, D., Matar, A. S., Brinkhues, S., Welton, R.H., Mueller, J., 2008, “Hydrophobic coatings for MEMS applications”, *Journal of Micromechanics and Microengineering*. **18,** (2008) 055030.

Dreyfus, R., Tabeling, P. and Willaime, H., 2003, "Ordered and Disordered Patterns in Two-Phase Flows in Microchannels", *Physical Review Letters*, **90 (14)**, pp. 144505-1-144505-4.

Dudukovic′, M.P., Larachi, F., Mills, P.L., 2002, "Multiphase Catalytic Reactors: A Perspective on Current Knowledge and Future Trends", *Catalysis Reveiws*, **44(1)**, pp. 123–246

Duffy, D.C., McDonald, J.C., Schueller, O.J. A., Whitesides, G. M., 1998, "Rapid Prototyping of Microfluidic Systems in Poly(dimethylsiloxane)", *Analytical Chemistry*, 70, pp 3781 – 3789.

Dyer, C.K., 2002, "Fuel Cells for Portable Applications", *Journal of Power Sources*, **106**, pp. 31-34.

Erbil, H.Y, Demirel, A.L., Avcı, Y., Mert, O., 2003, Transformation of a Simple Plastic into a Superhydrophobic Surface", *Science,* **299,** pp. 1377-1380.

Erickson, D. and Li, D., 2004, "Integrated Microfluidic Devices", *Analitica Chimica Acta,* **507,** pp. 11 – 26.

Fairbrother, F., Stubbs, A.E., 1935, "The bubble-tube method of measurement", *Journal of the Chemical Society,* **1**, 527–529.

Fogler, H.S, 2006, "Elements of Chemical Reaction Engineeting", Prentice Hall, New York.

Fuerstman, M.J., Garstecki, P., Whitesides, G.M., 2007,"Coding/Decoding and Reversibility of Droplet Trains in Microfluidic Networks", *Science*, Vol. 315, pp. 828-832

Gadd, J.C., Kuyper, C.L., Fujimoto, B.S., Allen, R.W., and Chiu, D.T., 2008, "Sizing Subcellular Organelles and Nanoparticles Confined within Aqueous Droplets", *Analytical Chemistry*, **80**, pp. 3450-3457.

Garstecki, P., Fuerstman, M.J., Stone, H.A., and Whitesides, G.M., 2006, "Formation of Droplets and Bubbles in a Microfluidic T-junction- Scaling and Mechanism of Break-up", *Lab on a Chip*, **6**, pp. 437-446.

Gobby, D., Angeli, P. and Gavriilidis, A., 2001, "Mixing Characteristics of T-type Microfluidic Mixers", *Journal of Micromechanics and Microengineering*, **11**, pp. 126-132.

Gruber, R., Melin, T., 2003, "Radial mass-transfer enhancement in bubble train flow", *International Journal of Heat and Mass Transfer,* **46**, pp. 2799–2808.

Günther, A. and Jensen, K.F., 2006, “Multiphase Microfluidics: From Flow Characteristics to Chemical and Materials Synthesis”, *Lab on Chip*, **6**, pp. 1487-1503.

Günther, A., Jhunjhunwala, M. , Thalmann, M., Schmidt, M. A. and Jensen, K. F., 2005,”Micromixing of Miscible Liquids in Segmented Gas-Liquid Flow”, *Langmuir*, **21**, pp. 1547–1555.

Günther, A., Khan, S.A., Thalmann, M., Trachsel, F. and Jensen, K.F., 2004, “ Transport and Reaction in Microscale Segmented Gas-Liquid Flow”, *Lab on a Chip*, **4**, pp. 278-286.

Günther, M., Schneider, S., Wagner, J., Gorges, R., Henkel, Th., Kielpinski, M., Albert, J., Bierbaum, R., Köhler, J.M., 2004, “Characterisation of residence time and residence time distribution in chip reactors with modular arrangements by integrated optical detection”, *Chemical Engineering Journal*, **101**, pp. 373–378.

Haeberle, S., and Zengerle, R., 2007, “Microfluidic platforms for lab-on-a-chip applications”, *Lab on a Chip*, **7**, pp. 1094–1110.

Hardt, S., Ehrfeld, W., Hessel, V., 2003, “Strategies for size reduction of microreactors by hear transfer enhancement effects”, *Chemical Engineering Communications*, **190**, pp. 540-559.

Hatch, A., Garcia, E. and Yager, P., 2004, “Diffusion-Based Analysis of Molecular Interactions in Microfluidic Devices”, *Proceeding of the IEEE*, **92(1)**, pp. 126-139.

Hatch, A., Kamholz, A.E., Hawkins, K.R., Munson, M.S., Schilling, E.A., Weigl, B.H. and Yager, P., 2001, “A Rapid Diffusion Immunoassay in a T-Sensor”, *Nature Publishing Group*, **19,** pp. 461-465.

Hertzog, D.E., Ivorra, B., Mohammadi, B., Bakajin, O. and Santiago, J.G., 2006, “Optimization of a Microfluidic Mixer for Studying Protein Folding Kinetics”, *Analytical Chemistry*, **78**, pp. 4299-4306.

Inoue, S. and Spring, K.R., 1997, “Video Microscopy the Fundamentals, 2nd Edition”, *Plenum Press*, New York.

Ismagilov, R.F., Stroock, A.D., Kenis, J.A., Stone, H.A. and Whitesides, G., 2000, “Experimental and Theoretical Scaling Laws For Transverse Diffusive Broadening in Two-Phase Laminar Flows in Microchannels”, *Applied Physics Letters*, **76 (17)**, pp. 2376-2378.

Jacobsen, S.C., Culbertson, C.T., Daler, J.E. and Ramsey, J.M, 1998, “Microchip Structures for Submillisecond Electrophoresis”, *Analytical Chemistry*, **70**, pp. 3476-3480.

Jensen, K.F., 2001, "Microreaction engineering-is small better?", *Chemical Engineering Science,* **56,** pp. 293-303.

Jensen, M.J., Stone, H.A., Bruus, H., 2006, "A numerical study of two-phase Stokes flow in an axisymmetric flow-focusing device", *Physics of Fluids* **18**, 077103 (2006)

Johnson, L.V., Walsh, M.L., Bockus, B.J. and Chen, L.B., 1981, "Monitoring of Relative Mitochondrial Membrane Potential in Living Cells by Fluorescence Microscopy", *The Journal of Cell Biology*, **88**, pp. 526-535.

Johnson, T.J., Ross, D., and Locascio, L.E., 2002, " Rapid Microfluidic Mixing", *Analytical Chemistry*, **74**, pp. 45-51.

Kakuta, M., Jayawickrama, D.A., Wolters, A.M., Manz, A. and Sweedler, J.V., 2003, "Micromixer-Based Time-Resolved NMR: Applications to Ubiquitin Protein Conformation" *Analytical Chemistry*, **75**, pp. 956–960.

Kamholz, A. E., 2004, "Proliferation of Microfluidics in Literature and Intellectual Property", *Lab on Chip*, 4, pp. 16N-20N.

Kamholz, A.E., Weigl, B.H., Finlayson, B.A. and Yager, P., 1999, "Quantitative Analysis of Molecular Interaction in a Microfluidic Channel: The T-sensor", *Analytical Chemistry*, **71 (23)**, pp. 5340-5347.

Kashid, M.N., Platte, F., Agar, D.W., Turek, S., 2007, "Computational modelling of slug flow in a capillary microreactor", *Journal of Computational and Applied Mathematics,* **203**, pp. 487 – 497.

Khan, S.A., Gunther, A., Schmidt, M.A., Jensen, K.F., 2004, "Microfluidic synthesis of colloidal silica", *Langmuir,* **20**, pp. 8604–8611.

Kirby, B. and Hasselbrink Jr., E.F., 2004, "Zeta Potential of Microfluidic Substrates: 1. Theory, Experimental Techniques and Effects on Separations", *Electrophoresis*, **25**, pp. 187-202.

Kjeang, E., McKechnie, J., Sinton, D., Djilali, N., 2007, "Planar and Three-Dimensional Microfluidic Fuel Cell Architectures Based on Graphite Rod Electrodes.", *Journal of Power Sources,* **168,** pp. 379-390.

Kjeang, E. K., Michel, R., Harrington, D. A., Djilali, N., Sinton, D. (2008) "A Microfluidic Fuel Cell with Flow-Through Porous Electrodes." *Journal of American Chemical Society,* **130,** pp. 4000-4006.

Kolb, W.B., Cerro, R.L., 1991, "Coating the inside of a capillary of square cross-section", *Chemical Engineering Science,* **46 (9)**, pp. 2181–2195.

Köhler, J.M., Henkel, Th., Grodrian, A., Kirner, Th., Roth, M., Martin, K., Metze, J., 2004, "Digital reaction technology by micro segmented flow—components, concepts and applications", *Chemical Engineering Journal*, **101**, pp. 201–216.

Krause, E., 2005. "Fluid Mechanics", Springer-Verlag Berlin Heidelberg.

Krishnadasan, S., Tovilla, J., Vilar, R., deMello, A. J. and deMello J. C., 2004, "On-line analysis of CdSe nanoparticle formation in a continuous flow chip-based microreactor", *Journal of Materials Chemistry*, **14,** pp. 2655-2660.

Kreutzer, M.T., 2003, "Hydrodynamics of Taylor flow in capillaries and monoliths channels". Doctoral dissertation. Delft University of Technology, Delft, The Netherlands.

Kreutzer, M.T., Du, P., Heiszwolf, J.J., Kapteijn, F., Moulijn, J.A., 2001, "Mass transfer characteristics of three-phase monolith reactors", *Chemical Engineering Science,* **56**, pp. 6015–6023.

Kreutzer, M.T., Günther, A., Jensen, K.F., 2008, "Sample Dispersion for Segmented Flow in Microchannels with Rectangular Cross Section", *Analytical Chemistry*, **80**, pp. 1558-1567.

Kreutzer, M.T., Heiszwolf, J.J., Kapteijn, F., Moulijn, J.A., 2003. Pressure drop of Taylor flow in capillaries: impact of slug length. In: Proceedings of the First International Conference on Microchannels and Minichannels. A.S.M.E, Rochester NY, U.S.A, pp. 153–159.

Kreutzer, M. T., Kapteijn, F., Moulijn, J. A., Heiszwolf, J. J., 2005, "Multiphase monolith reactors: Chemical reaction engineering of segmented flow in microchannels" *Chemical Engineering Science*, **60**, pp. 5895–5916.

Kawahara, A., Chung, P.M.-Y., Kawaji, M., 2002, "Investigation of two-phase flow pattern, void fraction and pressure drop in a microchannel", *International Journal of Multiphase Flow,* **28**, pp. 1411–1435.

Lebens, P.J.M., Heiszwolf, J.J., Kapteijn, F., Sie, S.T., Moulijn, J.A., 1999,"Gas-liquid mass transfer in an internally finned monolith operated countercurrently in the film flow regime", *Chemical Engineering Science,* **54**, pp. 5119-5125.

Lee, J.N., Park, C. and Whitesides, G.M., 2003, "Solvent Compatibility of Poly(dimethylsiloxane)-Based Microfluidic Devices", *Analytical Chemistry*, **75**, pp. 6544-6554.

Levenspiel, O., and Smith, W. K., 1957, "Notes on diffusion-type model for the longitudinal mixing of fluids in flow "Chemical *Engineering Science*, **6**, pp. 227–233.

Lohse, S., Kohnen B.T, Janasek, D., Dittrich, P.S., Franzke, J., and Agar, D.W, 2008, "A novel method for determining residence time distribution in intricately structured microreactors", *Lab on a Chip*, **8**, pp. 431–438.

Madou, M.J., 1997, "Fundamentals of Microfabrication", Boca Raton, FL: CRC Press.

Marsh, J.H., Bhattacharyya, D., Helmy, A.S., Avrutin, E.A. and Bryce, A.C., 2000, "Engineering Quantum-Dot Lasers", *Physica E*, **8**, pp. 154-163.

McDonald, J.C., Chabinyc, M.L., Metallo, S.J., Anderson, J.R., Stroock, A.D., and Whitesides, G.M., 2002, "Prototyping of Microfluidic Devices in Poly(dimethylsiloxane) Using Solid-Object Printing", *Analytical Chemistry*, **74**, pp. 1537-1545.

McDonald, J. C., Duffy, D.C., Anderson, J.R., Chiu, D.T., Wu, H., Schueller, O.J.A, Whitesides, G.M., 2000, "Fabrication of microfluidic systems in poly(dimethylsiloxane)", *Electrophoresis*, 21, pp. 27-40.

McKechnie, J., 2006, "Fabrication of Microfluidic Devices with Applications to Membraneless Fuel Cells", M.A.Sc. Thesis, *Department of Mechanical Engineering, University of Victoria.*

Meldrum, D.R., Holl, M.R., 2002, "Microscale Bioanalytical Systems", *Science*, **297**, pp. 1197-1198.

MicroChem, *Nano SU-8: Negative tone photoresist, formulation 2-25.* Newton, MA, 2002a.

MicroChem, *Nano SU-8: Negative tone photoresist, formulation 50-100.* Newton, MA, 2002a.

Munson, M.S., Hawkins, K.R., Hasenbrank, M.S. and Yager, P., 2005, "Diffusion Based Analysis in a Sheath-flow Microchannel: The Sheath-flow T-sensor", *Lab on Chip*, **5**, pp. 856-862.

Muradoglu, M., Günther, A., Stone, H.A., 2007, "A computational study of axial dispersion in segmented gas-liquid flow", *Physics of Fluids,* **19**, 072109.

Nakajima, A., Hashimoto, K., and Watanabe, T., 2001, "Recent Studies on Super-Hydrophobic Films", *Monatshefte für Chemie*, **132**, pp. 31-41.

Ng, J. Gitlin, I., Stroock, A.D. and Whitesides, G.M., 2002, "Components for Integrated Poly(dimethylsiloxane) Microfluidic Systems", *Electrophoresis*, 23, pp. 3461-3473.

Nguyen, N. T., Wereley, S. T., 2002, "Fundamentals and applications of microfluidics." Artech House, Norwood, MA.

Nguyen, N-T. and Wu, Z., 2004, "Micromixers – A Review", *Journal of Micromechanics and Microengineering*, **15**, pp. R1-R16.

Nozik, A.J., 2002, "Quantum Dot Solar Cells", *Physica E*, **14**, pp. 115-120.

Owen, M. J. and Smith, P.J., 1994, "Plasma Treatment of Polydimethylsiloxane", *Journal of Adhesion Science and Technology*, **8**, pp. 1061-1224.

Ozkan, F., Worner, M., Wenka, A., and Soyhan, H.S., 2007, "Critical evaluation of CFD codes for interfacial simulation of bubble-train flow in a narrow channel", *International Journal for Numerical Methods in Fluids*, (In Press).

Park, N-M., Kim, T-S. and Parka, S-J., 2001, "Band gap engineering of amorphous silicon quantum dots for light-emitting diodes", *Applied Physical Letters*, **78 (17)**, pp. 2575-2577.

Pedersen, H., Horvath, C., 1981, "Axial Dispersion in a Segmented Gas-Liquid Flow", *Industrial & Engineering Chemistry Fundamentals,* **20,** pp. 181-186.

Pinaud, F., Michalet, ., Bentolila, L.A., Tsay, J.M., Doose1, S., Li, J.J., Iyer, G., Weiss, S., 2005, "Advances in fluorescence imaging with quantum dot bio-probes", *Biomaterials*, **27**, pp. 1679-1697.

Polyanin, A.D., Kutrpov, A.M., Vyazmin, A.V., Kazenin, D.A., 2002 "Hydrodynamics, Mass and Heat Transfer in Chemical Engineering", *Taylor & Francis*, New York.

Probstein, R.F., 1994, "Physiochemical Hydrodynamics", 2nd edn., *Wiley*, New York.

Purcell, E.M., 1976, "Life at Low Reynolds Number", *Amercian Journal of Physics*, **45 (1)**, pp. 3-9.

Rallison, J. M., 1984, "The Deformation of Small Viscous Drops and Bubbles in Shear Flows", Annual. *Review of Fluid Mechanics.* , **16**, 45-66.

Reyes, D.R., Iossifidis, D., Aurox, P-A. and Manz, A., 2002, "Micro Total Analysis Systems. 1. Introduction, Theory and Technology", *Analytical Chemistry*, **74**, pp. 2623-2636.

Reynolds, O., 1883, "An Experimental Investigation of the Circumstances Which Determine Whether the Motion of Water Shall be Direct of Sinuous, and of the Law of Resistance in Parallel Channels", *Philosophical Transactions of the Royal Society of London*, **174**, pp. 935-982.

Roy, S., Bauer, T., Al-Dahhan, M., Lehner, P., and Turek, T., 2004, "Monoliths as Multiphase Reactors: A Review", *AIChE Journal*, Vol 50, No. 11.

Salman, W., Angeli, P., Gavriilidis, A., 2005, "Sample Pulse Broadening in Taylor Flow Microchannels for Screening Applications", *Chemical Engineering Technology*, **28**, No. 4.

Salman, W., Gavriilidis, A., Angeli, P., 2004, "A model for predicting axial mixing during gas–liquid Taylor flow in microchannels at low Bodenstein numbers", *Chemical Engineering Journal,* **101,** pp. 391–396.

Schabas, G., 2007, "Microfluidic Self-Assembly of Quantum Dot Compound Micelles ", M.A.Sc. Thesis, *Department of Mechanical Engineering, University of Victoria.*

Schabas, G., Wang, C.-W., Oskooei, A., Yusuf, H., Moffitt, M.G., Sinton, D., 2008b, "Formation and Shear-Induced Processing of Quantum Dot Colloidal Assemblies in a Multiphase Microfluidic Chip." *Langmuir*, **24**, pp. 10596-10603.

Schabas, G., Yusuf, H., Moffitt, M. G., Sinton, D., 2008a, "Controlled Self-Assembly of Quantum Dots and Block Copolymers in a Microfluidic Device." *Langmuir*, **24**, pp. 637-643.

Schumacher, J. T., Grodrian, A., Kremin, C., Hoffmann, M., and Metze, J., 2008, "Hydrophobic coating of microfluidic chips structured by SU-8 polymer for segmented flow operation", *Journal of Micromechanics and Microengineering*, **18,** (2008) 055019.

Seo, M., Nie, Z., Xu, S., Mok, M., Lewis, P.C., Graham, R. and Kumacheva, E., 2005, "Continuous Microfluidic Reactors for Polymer Particles", *Langmuir*, **21**, pp. 11614-11622.

Serizawa, A., Feng, Z., Kawara, Z., 2002, "Two-phase flow in microchannels", *Experimental Thermal and Fluid Science,* **26**, pp. 703–714.

Shestopalov, I., Tice, J.D. and Ismagilov, R.F., 2004, "Multi-step synthesis of nanoparticles performed on millisecond time scale in a microfluidic droplet-based system", *Lab on Chip*, **4**, pp. 316-321.

Sharp, K.V., Adrian, R.J., Santiago, J. G. and Molho, J.I., 2002, "Liquid Flows in Microchannels", Chapter 6 in *The Mems Handbook*, *CRC Press*, New York, NY.

Sia, S.K., Whitesides G.M., 2003, "Microfluidic devices fabricated in poly(dimethylsiloxane) for biological studies", *Electrophoresis*, **24**, pp. 3563–3576.

Sinton, D., 2004, "Macroscale Flow Visualization", *Microfluid Nanofluid*, **1**, pp. 2-21.

Sinton, D., Erickson, D., Li, D., 2003, "Microbubble lensing-induced photobleaching (μ-BLIP) with application to microflow visualization", *Experiments in Fluids,* **35**, pp. 178–187

Sinton, D., Ren, L. and Li, D., 2003, “A Dynamic Loading Step for Microfluidic Chip Sample Injection”, *Journal of Colloid and Interface Science*, **266**, pp. 448–456.

Song, H., Chen, D.L., and Ismagilov, R.F., 2006, “Reactions in Droplets in Microfluidic Channels”, *Angewandte Chemie*, **45**, pp. 7336 -7356.

Song, H., Tice, J.D. and Ismagilov, R.F., 2003, “A Microfluidic System for Controlling Reaction Networks in Time”, *Angewandte Chemie International Edition*, **42 No. 7**, pp. 767-772.

Squires, T.M. and Quake S.R., 2005, “Microfluidics: Fluid physics at the Nanoliter Scale”, *Review of Modern Physics*, **77**, pp. 977-1026

Stone, H.A., 1990, “A simple derivation of the time-dependent convective-diffusion equation for surfactant transport along a deforming interface”, *Physics of Fluids A,* **2** (1).

Stone, H.A., 1994, “Dynamics of Drop Deformation and Breakup in Viscous Fluids”, *Annual.* Review *of Fluid Mechanics.* , **26**, 65-102.

Stone, H.A., Strook, A.D. and Ajdari, A., 2004, “Engineering Flows in Small Devices: Microfluidics Towards a Lab-on-a-Chip”, *Annual Review of Fluid Mechanics*, **36**, pp. 381-411.

Stroock, A. D., Dertinger, S. K. W., Ajdari, A., Mezic, I. Stone, H. A., and Whitesides, G. M., 2002, ”Chaotic Mixer for Microchannels”, *Science*, **295**, pp. 647–651.

Suo, M., Griffith, P., 1964, “Two phase flow in capillary tubes”, *Journal of Basic Engineering*, **86**, pp. 576–582.

Taitel, Y., Bornea, D., Dukler, A.E., 1980, “Modeling flow pattern transitions for steady upward gas-liquid flow in vertical tubes. *AIChE Journal*, **26**, pp. 345-354.

Taylor G.I., 1953, “Dispersion of soluble matter in solvent flowing slowly through a tube.” *Proceeding of the Royal Society of London*, A, **219**, pp 186–203.

Taylor G.I., 1954, “Conditions under which dispersion of a solute in a stream of solvent can be used to measure molecular diffusion.”, *Proceeding of the Royal Society of London*, A, pp 473–477.

G.I. Taylor, 1961, “Deposition of a viscous fluid on the wall of a tube”, *Journal of Fluid Mechanics.* **10**, pp. 161–165

Thiers, R.E., Reed, A.H., Delander, K., 1971,” Origin of the lag phase of continuous-flow analysis curves”, *Clinical Chemistry,* **17** (1), pp. 42–48.

Thulasidas, T.C., Abraham, M.A., Cerro, R.L., 1995a, “Bubble-train flow in capillaries of circular and square cross section”, *Chemical Engineering Science,* **50 (2)**, pp. 183–199

Thulasidas, T.C., Abraham, M.A., Cerro, R.L., 1997, “Flow patterns in liquid slugs during bubble-train flow inside capillaries” *Chemical Engineering Science*, **52(17)**, pp. 2947–2962.

Thulasidas, T.C., Abrahams, M.A., Cerro, R.L., 1999, “Dispersion during bubble-train flow in capillaries”, *Chemical Engineering Science,* **54**, pp. 61-76.

Tice, J.D., Song, H., Lyon, A.D. and Ismagilov, R.F., 2003, “Formation of Droplets and Mixing in Multiphase Microfluidics at Low Values of the Reynolds and the Capillary Numbers”, *Langmuir*, **19**, pp. 9127-9133.

Trachsel, F., Gunther, A., Khan, S. and Jensen, K. F., 2005, “Measurement of residence time distribution in microfluidic systems”, *Chemical Engineering Science*, **60**, pp. 5729–5737.

Triplett, K.A., Ghiaasiaan, S.M., Abdel-Khalik, S.I., Sadowski, D.L., 1999, “Gas–liquid two-phase flow in microchannels, Part I: two-phase flow patterns. *International Journal of Multiphase Flow,* **25**, pp. 377–394.

Tsougeni, K., Tserepi, A., Boulousis, G., Constantoudis, V., Gogolides, E., 2007, ” Control of Nanotexture and Wetting Properties of Polydimethylsiloxane from Very Hydrophobic to Super-Hydrophobic by Plasma Processing”, *Plasma Processes and Polymers*, **4**, pp. 398–405.

Tüdos, A.J., Besselink, G.A.J., and Schasfoort, R.B.M., 2001, “Trends in miniaturized total analysis systems for point-of-care testing in clinical chemistry”, *Lab on a Chip*, **1**, pp. 83–95.

Vilkner, T., Janasek, D. and Manz, A. 2004, “Micro Total Analysis Systems. Recent Developments”, *Analytical. Chemistry*, **76**, pp. 3373-3386.

Wainright, J.S., Savinell, R.F., Liu, C.C., Litt, M., 2003, “Microfabricated fuel cells”, *Electrochimica Acta*, **48**, pp. 2869-2877.

Wang, H., Iovenitti, P., Harvey, E., and Masood, S., 2002, “Optimizing layout of obstacles for enhanced mixing in microchannels”, *Smart Materials and Structures*, **11, pp.** 662–667.

Wang, C.-W. and Moffitt, M. G., 2004, “Surface-Tunable Photoluminescence from Block Copolymer-Stabilized Cadmium Sulfide Quantum Dots”, *Langmuir*, **20**, pp. 11784-11796.

Wang, J., 2000, “From DNA Biosensors to Gene Chips. Nucleic Acids”, *Nucleic Acids Research,* **28**, pp. 3011-3016.

Weigl, B.H. and Yager, P., 1999, "Microfluidics Diffusion-Based Separation and Detection", *Science*, **283 (5400)**, pp. 346-347.
West, J., Becker, M., Tombrink, S., and Manz, A., 2008, "Micro Total Analysis Systems: Latest Achievements", *Analytical Chemistry,* **80**, pp. 4403–4419.

White, F.M., 2003, "Fluid Mechanics: Fifth Edition", *McGraw Hill*, New York.

Whitesides, G.M., 2006, "The origins and the future of microfluidics", *Nature*, **442**, pp. 368-373.

Whitesides, G. M., Stroock, A. D., 2001 "Flexible methods for microfluidics." *Physics Today*, **54(6)**, pp. 42–48.

Yen, B.K.H., Günther, A., Schmidt, M.A., Jensen, K.F. and Bawendi, M.G., 2005, "A Microfabricated Gas–Liquid Segmented Flow Reactor for High-Temperature Synthesis: The Case of CdSe Quantum Dots", *Angewandte Chemie International Edition*, **44**, pp. 5447-5451.

Yusuf, H., Kim, W-G., Lee, D. H., Guo, Y. and Moffitt, M. G., 2007a, "Size Control of Mesoscale Aqueous Assemblies of Quantum Dots and Block Copolymers", *Langmuir*, **23**, pp. 868-878.

Yusuf, H., Kim, W-G., Lee, D. H., Aloshyna, M., Brolo, A.G. and Moffitt, M. G., 2007b, "A Hierarchical Self-Assembly Route to Three-Dimensional Polymer-Quantum Dot Photonic Arrays", *Langmuir*, **23**, pp. 5251-5254.

Zhao, T.S., Bi, Q.C., 2001, "Co-current Air-water Two-phase Flow Patterns in Vertical Triangular Microchannels", *International. Journal of Multiphase Flow*, **27**, pp. 765-782.

Zhao, L., Rezkallah, K.S., 1993, "Gas–liquid flow patterns at microgravity Conditions". *International Journal of Multiphase Flow*, **19 (5)**, pp. 751–763.

Zhen-hua, L., Yi-pu, G., 2007, " Effect of Surfactant on Two-phase Flow Patterns of Water-gas in Capillary Tubes" , *Journal of Hydrodynamics*, Ser.B, 2007,**19(5)**, pp. 630-634.

Zheng, B., Tice, J. D., and Ismagilov, R. F., 2004, "Formation of Droplets of Alternating Composition in Microfluidic Channels and Applications to Indexing of Concentrations in Droplet-Based Assays", *Analytical Chemistry*, **76**, pp. 4977-4982.